BRNO UNIVERSITY OF TECHNOLOGY

VYSOKÉ UČENÍ TECHNICKÉ V BRNĚ

CENTRAL EUROPEAN INSTITUTE OF TECHNOLOGY BUT

STŘEDOEVROPSKÝ TECHNOLOGICKÝ INSTITUT VUT

PREPARATION OF HYBRID CERAMIC MATERIALS BY ICE-TEMPLATING

PŘÍPRAVA HYBRIDNÍCH KERAMICKÝCH MATERIÁLŮ METODOU ICE-TEMPLATING

DOCTORAL THESIS
DIZERTAČNÍ PRÁCE

AUTHOR — **Ing. Jakub Roleček**
AUTOR PRÁCE

SUPERVISOR — **doc. Ing. David Salamon, Ph.D.**
ŠKOLITEL

BRNO 2019

Declaration

I declare that this doctoral thesis has been worked out by myself under supervision of doc. Ing. David Salamon, Ph.D., and that all the quotations from the used literary sources are accurate and complete.

Brno . . . .

(author's signature)

Abstract

Ice-templating, also known as freeze-casting, is a relatively simple, inexpensive, and very versatile technique to fabricate porous ceramic scaffolds with the controlled microstructure. The prepared scaffolds are used for preparation of hybrid ceramic composites or as bioceramic scaffolds. Hybrid ceramic composites are based on mimicking the architecture of natural/biological materials and structures. The motivation is to emulate nature's toughening mechanisms by infiltration of polymers into ceramic structures. However, the main problem for an application is size of the prepared scaffolds. Preparation of large scaffolds by ice-templating method requires achieving controlled ice crystals growth throughout the whole sample volume. Thus it is necessary to precisely control the ice-templating process to obtain the well-defined lamellar architecture. Biological activity of bioceramic materials depends on a combination of physical and chemical characteristics that are strongly related to their microstructure. The scaffold porosity has to be interconnected with a sufficiently large pore size for successful bone tissue growth within the whole volume of an implant.

Presented Ph.D. dissertation work was focused on scale up of the ceramic scaffolds prepared by ice-templating, creation of multiscale porosity inside the scaffolds, and preparation of hybrid ceramic composites for a ballistic protection.

Ceramic suspensions for ice-templating were successfully prepared from different powders (mainly hydroxyapatite and alumina) with different solid loadings of ceramic powder from 7.5 vol.% up to 45 vol.%. The influence of suspension additives on formation of lamellar roughness and interlamellar bridging, and impact of these microstructural elements was studied. Hybrid alumina/polymer composites were successfully designed and prepared from ice-templated alumina plates with lamella length up to 70 mm and various polymeric resins. Mechanical performance of hybrid alumina/epoxy resin composites was tested and the results showed that ice-templating reveals to be the robust method for production of hybrid ceramic-polymer composites with good strength/density ratio. However ballistic tests of ice-templated alumina/polymer hybrid composites revealed that majority of composites presented in this work were not able to efficiently stop armor piercing projectiles. Combination of ice-templating and indirect rapid prototyping has been shown to enable manufacturing of bioceramic scaffolds for bone replacement from hydroxyapatite with multiscale porosity which could prove to be beneficial for the development of highly porous bioactive scaffolds with enhanced biological performance. Ice-templating also significantly modified the phase composition change during the sintering of hydroxyapatite scaffolds.

Key words

Ice-templating, hybrid ceramic composites, bioceramic scaffolds, Al_2O_3, HAP, aqueous suspensions, mechanical properties, ballistic testing

Abstrakt

Ice-templating, známý také jako freeze-casting, je relativně jednoduchou, levnou a velmi univerzální technikou pro výrobu porézních keramických struktur s řízenou mikrostrukturou. Takto připravené keramické struktury jsou použity pro výrobu hybridních keramických kompozitů, nebo jako biokeramické scaffoldy. Hybridní keramické kompozitní materiály jsou založeny na napodobování přírodních/ biologických materiálů. Hlavním cílem je napodobit v přírodě se vyskytující zhouževnaťující mechanismy tím, že porézní keramické struktury jsou po slinutí napuštěny polymerními materiály. Hlavním problémem při výrobě porézních keramických vzorků s velkými rozměry, pomocí metody ice-templating, je dosažení řízeného růstu ledových krystalů v celém objemu vzorku. Aby tedy bylo možné získat velké keramické vzorky s dobře definovanou lamelární strukturou je třeba proces ice-templatingu velmi přesně kontrolovat. Biologická aktivita biokeramických materiálů závisí na kombinaci fyzikálních a chemických charakteristik, které silně souvisejí s jejich mikrostrukturou. Porozita scaffoldů musí být vzájemně propojená a velikostí pórů dostatečně velká pro úspěšný růst kostní tkáně v celém objemu implantátu.

Prezentovaná disertační práce je zaměřena na problematiku zvětšování rozměrů keramických vzorků připravených pomocí metody ice-templating, vytvoření víceúrovňové porozity uvnitř vzorků a výrobu hybridních keramických kompozitů pro balistickou ochranu.

Keramické suspenze pro ice-templating byly úspěšně připraveny z různých prášků (zejména hydroxyapatitu a oxidu hlinitého s různým plněním keramického prášku od 7,5 obj.% do 45 obj.%. Byl také studován vliv aditiv na utváření lamelární drsnosti a mezilamelárních přemostění. V současnosti je zkoumán dopad těchto strukturních prvků na výsledné mechanické vlastnosti. Hybridní kompozity oxid hlinitý/polymer byly úspěšně navrženy a připraveny z destiček z oxidu hlinitého připravených metodou ice-templating s délkou lamel až 70 mm a různých polymerních pryskyřic. Byla testovány mechanické vlastnosti hybridních kompozitů oxid hlinitý/polymer a výsledky ukázaly, že ice-templating je robustní metodou pro výrobu hybridních kompozitů keramika-polymer s dobrým poměrem pevnost/hustota. Avšak balistické testy hybridních kompozitů oxid hlinitý/polymer odhalily, že většina kompozitů vytvořených v rámci této práce nebyla schopna účinně zastavit střely s průbojným jádrem. Ukázalo se, že kombinace procesu ice-templating a nepřímého 3D tisku umožňuje výrobu biokeramických scaffoldů pro kostní náhrady z hydroxyapatitu s víceúrovňovou porozitou, což by se mohlo ukázat jako prospěšné pro vývoj bioaktivních vysoce porézních scaffoldů se zvýšenou biologickou aktivitou. Ice-templating také významně ovlivnil změnu fázového složení během slinování hydroxyapatitových vzorků.

Klíčová slova

Ice-templating, hybridní kramické kompozity, biokeramické scaffoldy, Al_2O_3, HAP, vodné suspenze, mechanické vlastnosti, balistické testy

ROLEČEK, Jakub. *Preparation of hybrid ceramic materials by ice-templating.* Doctoral thesis. Brno: Brno University of Technology, Central European Institute of Technology, 2019. 86 p. Supervised by doc. Ing. David Salamon, Ph.D.

Table of contents

1 Introduction

Ceramics are defined as inorganic, non-metallic materials which are typically crystalline in nature and contain metallic and non-metallic elements. Typical examples are Al_2O_3, CaO, ZrO_2, SiC, and Si_3N_4. There are several broad categories of ceramics classifying the industrial products as follows: clay products, white ware, refractories, glasses, cements, abrasives, and advanced ceramics [1].

During the last decades there has been a strong movement to use advanced ceramics in new technological applications and to understand the mechanical behavior of these materials. Unfortunately, ceramics are in general brittle, so consequently, there has been a strong emphasis on understanding the mechanical properties of ceramics and on improving their strength, toughness and contact-damage resistance [2].

One approach to enhance properties of advanced ceramics is to create ceramic composites. Ceramic composites provide the exemplary way to reduce the negative effects of brittleness, whilst retaining the further advantageous properties of ceramic structures. Ceramic composites have generally low densities compared to their metallic counterparts, leading to beneficial lightweight structures. The major scientific interests, besides resistance to oxidation, are mechanical properties of ceramic composites, mainly fracture toughness and damage tolerance. Thus, those mechanisms which are responsible for such fracture resistance must be adjusted to achieve crack deflection and high energy dissipation in general [1].

One group of ceramic composites is ceramic matrix composites (CMCs). The behavior CMCs is heavily dependent upon the components. Clever combination of reinforcements, interfaces and matrix materials leads to sophisticated composites achieving outstanding performances, especially under severe environmental conditions. This enables the designing engineer to adjust the composite properties directly to various requirements of applications and load conditions. In all CMCs variations – whether particles, short- or long-fiber-reinforced – either the interface or the matrix must meet this challenge. In consequence, different CMC strategies have been followed, including weak interface composites (WIC) or weak matrix composites (WMC) [1].

Hybrid ceramic composites are another subgroup of CMC. They are often based on mimicking the architecture of natural/biological materials and structures. Effort in designing and manufacturing hybrid ceramic composites is to emulate nature's toughening mechanisms by infiltration of polymers into ceramic structures. Such biomimetic materials have significantly better mechanical properties (tensile strength, fracture toughness) than the individual compounds that they are made of [3].

This work is focusing on adopting ice-templating as a new technique for preparation of relatively large ceramic scaffolds, compare with current state of art, and infiltrating them by various polymers to create hybrid ceramic composites with high toughness. Development of the technique from laboratory size to applicable dimensions is challenging, however necessary step for an application. Ballistic protection is our targeted application which can use benefits of hybrid composites: high toughness and low weight. Scientifically it is necessary to control ice-templating process and interlamellar bridging in wide range of temperatures.

2 Literature review

2.1 Ice-templating

Ice templating, also known as freeze-casting, is a complex process, where many parameters can affect the results: formulation of the suspension (nature of the solvent, particle distribution of the starting powder, solid loading, binder, surfactant, nature of the material, pH, viscosity), freezing conditions (setup, temperature, cooling rate) [3].

Despite its complexity is ice-templating relatively technically simple, inexpensive, and very versatile technique to fabricate bulk porous scaffolds. The basic idea of ice-templating is to obtain porosity replicating of ice crystals, by freezing suspension and subsequently removing the ice crystals by sublimation of the solvent (most commonly water is used as a solvent). The solid phase in the suspension can be of practically any nature, from ceramic to metal particles or polymer, but ceramic particles are the most used. Porous ceramic scaffolds can be obtained by controlled freezing of ceramic suspensions, which is followed by sublimation of water and densification (sintering). In ice-templating, the particles in ceramic suspension are ejected from the moving solidification front and pile up between growing ice crystals creating multilayer porous ceramic structures with well-defined architecture. The process is based on the very low solubility of the second phase in the solvent, which ensures its segregation during solidification. Typical process of ice-templating is shown in the Figure 1 [3].

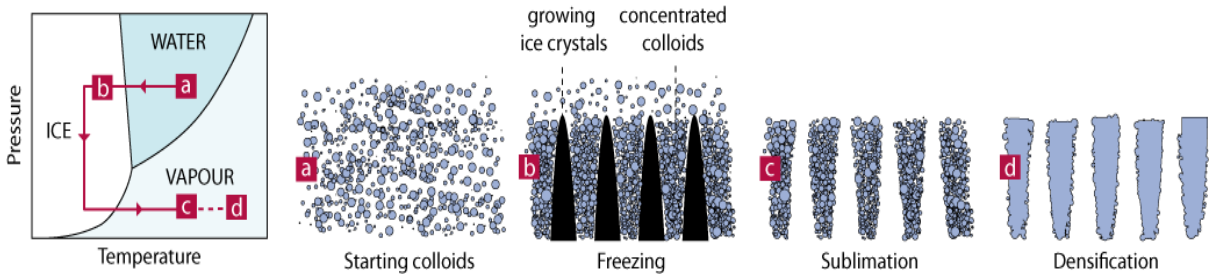

Figure 1. *Schematic diagram of the ice-templating method [3].*

Although there is increased interest in ice-templating method over the last decade, the first observation of the formation of cellular structures upon freezing goes back to over a century ago. The idea of using segregation to obtain specific architectures was firstly pursued by Mahler et al. [4], when they froze silica gels to obtain fibers. Processing of macro porous ceramic structures was firstly reported in 2001 by Fukasawa et al. [5].

Over the past 15 years, ice-templating has been widely applied to various classes of materials, in particular ceramics to produce macroporous samples. In recent years a lot of effort has been put into this production technique, which shows the ability to use a wide variety of nano- to macro-scaled powders and various dispersion liquids (solvents). Many formulation and process parameters, often inter-reliant, affect the final scaffold, because it is hard to understand relationships of various parameters. Only a few of these complex relationships have been investigated and published until now [3; 6].

2.1.1 Materials for ice-templating

In so far published studies that deal with ice-templating, as a method for porous scaffolds preparation (leaving aside polymers and metals), a wide variety of ceramic materials were used.

Al_2O_3, ZrO_2, SiC, Si_3N_4, TiO_2, ZrB_2, Cr_3C_2, AlN, mullite, hydroxyapatite, tri-calcium phosphate, lead zirconate titanate (PZT), barium titanate , silica/kaolinite, sialon, lithium iron phosphate, yttrium orthosilicate, cermets, cordierite, iron oxides, baghdadite, glass and bioglass [6]. Range of materials is only limited by ability to be dispersed in suspension without rapid sedimentation or chemical reaction.

2.1.2 Role of the solvent

Ice-templating implies that water is used, but generally a variety of solvents can be used for ice-templating experiments. Most commonly used solvents are: water, camphene, tert-butyl alcohol (TBA), naphthalene/camphor, dioxane, terpene,or carbon dioxide [6]. Some physical properties of selected solvents important for ice-templating are shown in the Table 1.

Table 1. *Physical properties of selected solvents used for ice-templating [7].*

Solvent type	Density ($g \cdot cm^{-3}$)	Boiling temperature (°C)	Freezing temperature (°C)	Saturated vapor pressure at 20 °C (kPa)	Surface tension ($mN \cdot m^{-1}$)
Water	1.00	100.0	0.0	2.3	73.1
Caphene	0.84	155.0	44.9	0.3	sublimes
Tert-butyl alcohol	0.79	82.5	25.3	4.1	20.7

As can be seen from Table 1, the working temperature of the ceramic suspension should correspond to the range where the solvent is liquid. Room temperature is usually used in the case of water, but different temperatures are necessary for camphene based and tert-butyl alcohol based suspensions (60°C and 38°C respectively) [7]. Due to its unique properties, water is used as the most common solvent in ice-templating. The expansion of water during the crystallization creates high mechanical pressure and promotes compaction of ceramic particles. This phenomenon is usually called as freeze-pressing. The effect of physical and chemical parameters under freezing on agglomeration degree and texture of final compacts has been discussed in details in case of aqueous alumina suspensions by Salamon et al [8].

Different porous ceramic structures achieved by using water, camphene and TBA as a solvents for ice-templating are shown in the Figure 2, respectively.

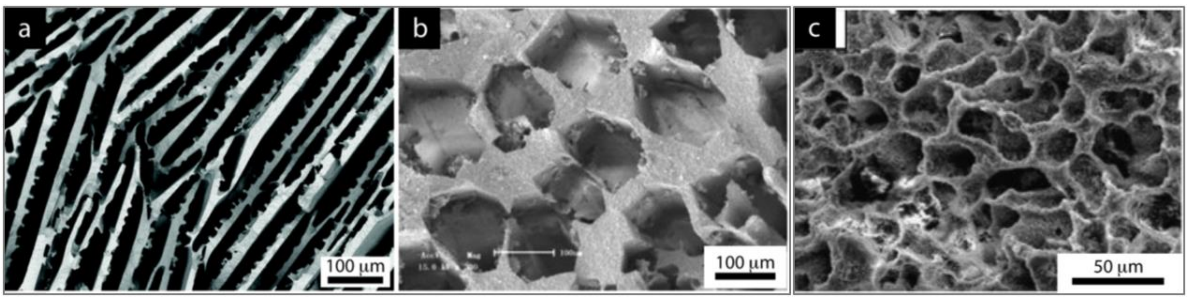

Figure 2. *Porous alumina structures obtained by ice-templating, using different solvents; (a) water, (b) TBA, (c) camphene [6].*

Water is most commonly used as a solvent for ice-templating because of economic and environmental viewpoint. Water has also some disadvantages including: high surface tension (poor wetting), low vapor pressure (slow drying), and sensitivity to pH (less stable, higher viscosity suspensions) [7].

Contrary, strong advantage of water in ice-templating is a possibility to influence its solidification behavior. In order to modify the structure of ice various co-solvents (cryoprotectants) may be added to the aqueous system. These additives are used extensively for freezing of biological tissues and can be used to reduce the effects of solute rejection and crystallite size during the solidification of water in suspensions of ceramic powders. The desired properties of cryoprotectants for ice-templating are: low toxicity, solubility in water, low freezing point depression, and cost effectiveness. Many cryoprotectants create significant shift of freezing points to very low temperatures, which is not convenient for subsequent freeze-drying of ice-templated ceramic samples. For example, mixing of glycerol with water (in proper proportions) yields shift of freezing temperature from -1.6 °C to -9.6 °C. Furthermore the addition of 20 wt.% of glycerol reduces the volumetric expansion of water from 10 % to 5 % [7; 9; 10].

The addition of glycerol obviously also affect the structure of ice-templated ceramic samples. Such microstructures are shown in Figure 3.

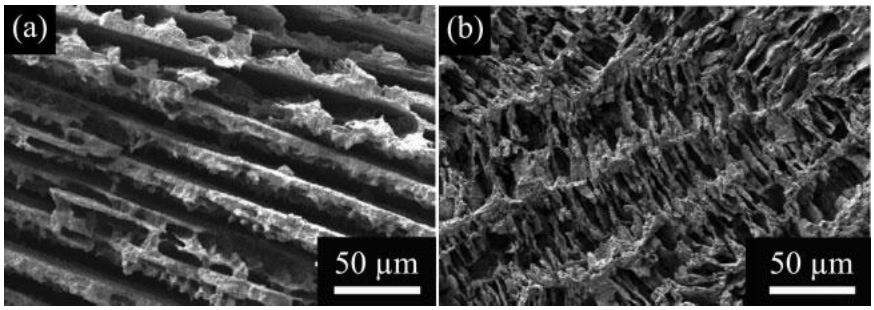

Figure 3. *Glycerol effect on microstructure of ice-templated hydroxyapatite scaffold; (a) water, (b) water + 20 wt.% glycerol [11].*

As it was mentioned above, several organic solvents with high melting points may be used instead of water. The requirements for the alternative disperse medium are following [7]:

- appropriate solidification temperature, which should be higher than the room temperature, but should not be too high
- liquid viscosity similar to water so that concentrated suspensions can be made
- limited volume change during solidification to avoid problems associated with solidification shrinkage or expansion
- higher vapor pressure in solid state necessary for freeze-drying
- moreover, the solvent should be safe and inexpensive.

Recently, such compounds as TBA and camphene have been tried as solvent in ice-templating process. These solvents not only suit mentioned requirements, but make freeze-drying possible at room temperatures and offer the ability to cast ceramics that are not compatible with water.

Camphene ($C_{10}H_{16}$) is a bicyclicmonoterpene. It is safe and inexpensive natural material which is commonly used in fragrance preparation. Camphene has a melting point about 45 °C [7], and at room temperature it is crystalline solid material. Furthermore, high vapor pressure at solid state is convenient for freeze-drying (see Table 1). Large gradient of camphene vapor pressure between the surface of camphene and surrounding atmosphere exists at room temperature and ambient pressure. Hence, camphene can be removed via sublimation without assistance of vacuum pump [7; 12].

During ice-templating, dendrites of camphene grow in certain crystallographic directions. Such freezing behavior results in formation of a bicontinuous structure, in which each separated phase is interconnected in 3D space, see Figure 2c. Moreover, it was found that the camphene-based ice-templating could be used to freeze very dilute ceramic suspensions with low solid loadings, which, accordingly, allow ultra-high-porosity ceramics with completely interconnected pore channels [7; 13].

Using a Tert-butyl alcohol (TBA) as solvent for ice-templating allows a flexible freezing process and results in relatively long pore channels after sublimation, which is a consequence of relatively high freezing temperature (see Table 1) [7; 14].

TBA normally creates long straight ice prisms without any branches unlike the dendrite structure of frozen water or camphene. Chen [10] observed that pore channels obtained after sublimation had straight polygonal cross sections. In case of water or camphene-based suspensions, pores have circular or elliptical cross sections, see Figure 2b. Thus TBA can be used for specific applications such as fabrication of ceramics with unidirectional pore structure (for example for water filters) [7].

Sofie [15] shown that TBA can be removed from ice-templated sample by rapid volatilization at 80 °C and this method is much faster than standard freeze-drying [7; 15].

Ice-templating is a versatile and flexible process for all kinds of solvent, its able to yield a very wide range of porosity values, from 99.9 vol.% for ice-templated graphene (for which no sintering is necessary), to several percent. A transition in the morphology of the pores is observed when the solid loading is high and redistribution of particles by the growing crystals cannot take place anymore. The typical solid loading for this transition is around 50–55 vol.% [16]. Above this critical solid loading, the low tortuosity of the individual pore channels is lost, and the pore size becomes smaller. The range of achievable pore sizes (of sintered ceramic scaffolds), when water, camphene, or TBA is used as a solvent, is plotted in Figure 4 [6].

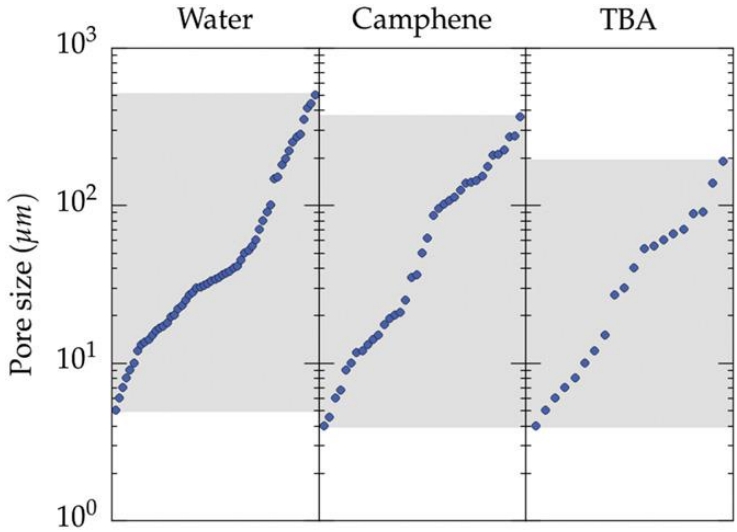

Figure 4. *Range of pore size achieved for the three most commonly used solvents: water, camphene, and TBA. The values are simply plotted in increasing order [6].*

Pore size range is essentially in range from 3-4 to 200-500 µm for all the solvents. Pores larger than 200 µm were not found with TBA, although this limit just might be a consequence of the lower number of records used for creation of the plot [6].

2.1.3 Suspension properties

Ceramic suspensions for ice-templating are typically composed of submicrometer-sized particles suspended in solvent (commonly water) and normally dispersants and binders are added.

Role of dispersants is to reduce particle aggregation and flocculation; dispersants can be anionic, cationic or neutral. Aggregation and flocculation are undesirable because they lead to heterogeneities in the final product and change the suspension's physical properties such as sedimentation and viscosity. If the particle size is constant viscosity depends on the type of interaction between particles and solvent, whether by van der Waals forces, hydrogen bonds or polar interactions. If the type of interaction is constant viscosity depends on the particle size [17].

Role of binders in suspensions is to increase the strength of the green ceramic bodies before sintering, or to form composite materials for which further processing is not necessary [17].

Other properties of suspension, such as pH, viscosity, eutectic temperature, osmotic pressure, and surface tension, influence the behavior of the freezing suspension. Required change of these properties is usually accomplished by adding various liquid modifiers. Rheological properties, such viscosity, show strong correlations to the resulting microstructure and mechanical properties of ice-templated scaffolds [18].

Sedimentation

Through the control of particles sedimentation (which depends on the particles density, size distribution and the solvent's density and viscosity) it is possible either to avoid or to generate structural gradients before and during freezing. When a spherical particle of radius r and mass m is immersed in a fluid of density ρ_L, it will experience two forces. First one due to the gravitational acceleration g = 9.807m·s^{-2} and the second force opposing it. This force accords to Archimedes

principle and is equal to the weight of the volume *V* of the fluid that particle displaces. The resulting force on the spherical particle is

$$F = (m - \rho_L V)g = (\rho_P - \rho_L)g\frac{4}{3}\pi r^3 \,. \tag{2.1}$$

If the particle's density is different than fluid´s in which it is immersed, it will, according to Stokes's law, experience a frictional force resisting its motion. This resisting force depends on the dynamic viscosity η of the solvent and both radius and velocity v_P of the particle,

$$F_f = 6\pi r\eta v_P \,. \tag{2.2}$$

Equating expressions (2.1) and (2.2) and solving for the velocity v_P, the particle's terminal velocity can be calculated,

$$v_P = \frac{2(\rho_P - \rho_L)g}{9}\,\frac{r^2}{\eta}\,. \tag{2.3}$$

To reduce sedimentation, the density difference between the spherical particle and solvent needs to be minimized. This means that for a given material pairing and terminal velocity, the viscosity needs to increase quadratically with an increase in the particle diameter to increase terminal velocity [17].

2.1.4 Freezing process

Particle trapping

Speed of crystal growth during solidification defines the freezing front velocity, which determines whether a particle in the suspension will be rejected and pushed ahead, or engulfed and trapped by the approaching liquid-solid interface. The important factor is the balance between two opposing forces that act on each particle: a repulsive force, which keeps the particle in the liquid phase owing to the system's resistance against a change in the surface energy, and an attractive force that, due to viscous drag, pushes the particle towards the solid-liquid interface, see Figure 5.

Thermodynamically, a particle can only be trapped if the free energy of the system $\Delta\sigma_0$ is negative

$$\Delta\sigma_0 = \sigma_{ps} - (\sigma_{pl} + \sigma_{sl}) < 0 \,, \tag{2.4}$$

where σps, σpl and σsl are the surface energies between the particle and frozen solid, the particle and the liquid and the solid and the liquid, respectively. The particle in the suspension will be engulfed and trapped, if energy of newly formed particle-solid surface is smaller than sum of energies of the particle-liquid and solid-liquid surfaces disappearing from the system; otherwise, the particle remains in the liquid [17].

Freezing front velocity can be calculated from equilibrium of repulsive and attractive forces, a critical velocity v_{cr} is that at which particle trapping occurs

$$v_{cr} = \frac{\Delta\sigma_0 a_0}{3\eta r}\,, \tag{2.5}$$

at freezing-front velocities below the critical value, particles are pushed ahead by the solid-liquid interface [17; 19][17, 19].

The Figure 5 schematically illustrates the interaction between a particle of radius *r* separated from the solid-liquid interface by a liquid film of thickness *d* on which an attractive force F_η and a repulsive force F_R are acting. Balancing the forces, a critical freezing front velocity *v* can be calculated. Above this velocity of the freezing front the particle will be engulfed and trapped. Below this velocity the particle will be rejected and pushed ahead by the solid-liquid interface [17].

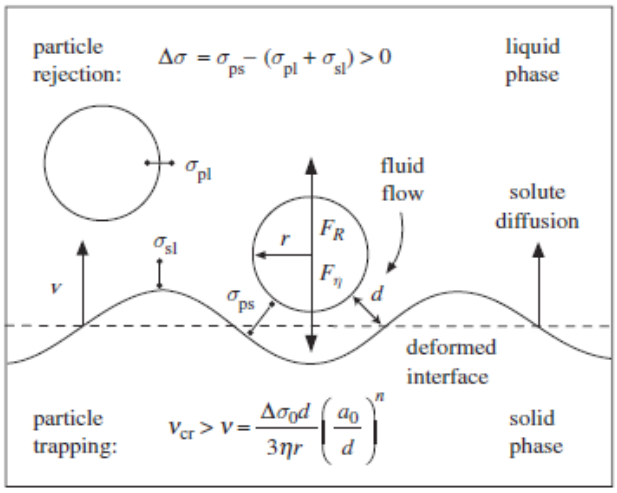

Figure 5. *Schematic illustration of interactions between particle and the freezing front [17].*

Freezing front velocity

Manipulating the freezing front velocity and temperature gradient inside the ceramic suspension significantly changes the spacing and thickness of the lamellae of ice-templated scaffold. Empirically it was shown that lamellar spacing λ decreases as the velocity *v* of the freezing front increases (for aqueous suspensions), following a relationship

$$\lambda \propto \frac{1}{v^n}, \tag{2.6}$$

where *n* depends on the particle size and vary from 1-4. Furthermore, the size and concentration of particles in a suspension can influence homogeneity, porosity, and surface roughness of the final scaffolds. Increasing the solid loading of the suspension (concentration of particles) decreases the resulting scaffold porosity. Decreasing the particle size generally increases uniformity of microstructural features that directly replicate the dendritic ice structure. The freezing front velocity is very important processing parameter, and it is necessary to control its value to obtain designed scaffold [17; 18; 20].

Effect of the freezing (solidification) front velocity on the thickness of the lamellae for alumina samples fabricated by ice-templating is shown in the Figure 6. The scanning electron micrographs shown in the graph correspond to cross sections parallel to the direction of the ice front movement. The sample was obtained with ultrafast freezing to gauge the thickness limit achievable by this technique [20].

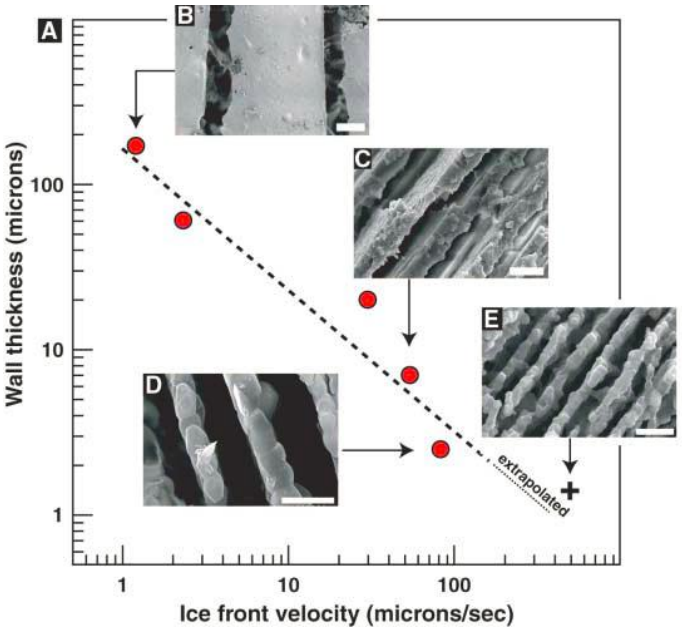

***Figure 6**. Dependence of the lamellae thickness of ice templated alumina scaffolds on the freezing front velocity. Scale bars indicate: (B) 50 µm (C) 10 µm (D) 5 µm (E) 5 µm [20].*

Stages of directional freezing

Initial zone - nucleation and growth

Directional solidification behavior of aqueous systems during ice-templating was studied and it was stated that immediately after the nucleation of ice crystals, ceramic particles are ejected from the growing planar ice front, leading to the formation of a constitutionally super-cooled zone directly ahead of the growing ice. This unstable region eventually results in perturbations, breaking the planar front into a columnar ice front, the phenomenon is known as Mullins-Serkerka instability [21].

However in-situ testing by Deville et al. [21; 22] revealed a different mechanism. Just before nucleation, the suspension is in an unstable super-cooled state. Homogeneous nucleation of ice crystals occurs followed by explosive crystal growth in every spatial and crystallographic direction. The initial nucleation and growth is so rapid (approaching 800 $mm \cdot s^{-1}$) that all particles in suspension are completely engulfed by the ice front because not enough time is given for their redistribution. This rapid ice crystal growth results in a structure with anisotropic particle distribution (initial zone structure), which is shown in the Figure 7 (from the *copper bottom* to the *zone e*) [21; 22].

Transition zone - change in microstructure

As solidification slows and growth kinetics of ice crystal becomes rate-limiting, the ice crystals begin to exclude the ceramic particles and a competitive growth process develops between two crystal groups, lamellar crystals oriented along the freezing direction (z-crystals) and pseudolamellar columnar dendritic crystals s along the radial direction(r-crystals). This part of ice-templated samples is called transition zone (Figure 7, *zones e -d*) [11; 23].

Within the transition zone, the r-crystals stop their growth or turn into z-crystals that eventually become the predominant orientation and lead to steady-state growth. There are several reasons for such turn. During freezing the growing crystals tend to align with the temperature gradient, as this is thermodynamically preferential and the lowest energy configuration. Aligned growth, however, can mean two different things. Assuming the temperature gradient is vertical, the growing crystals will be parallel (z-crystal) or perpendicular (r-crystal) to this gradient. A crystal that is placed horizontally can

still grow in line with the temperature gradient, but it will mean growth rather on its face than on its edges [23; 24].

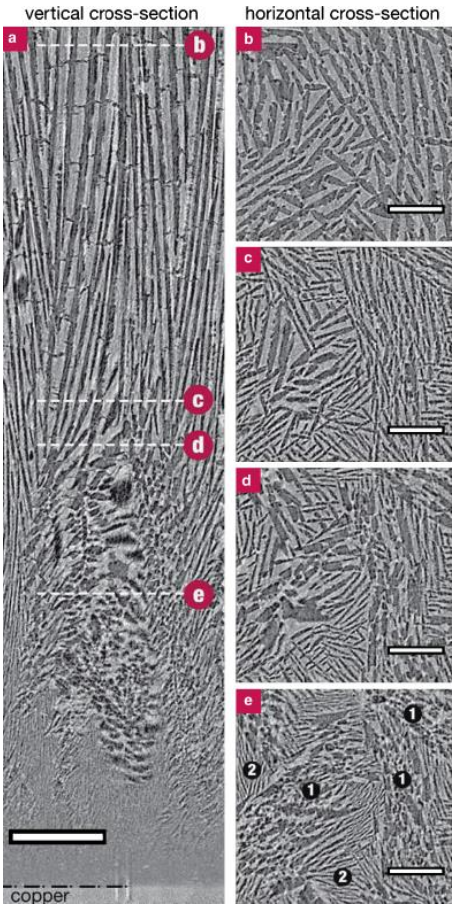

Figure 7. *Tomography reconstructed slices showing different zones within the ice-templated sample. Scale bars indicate: (a) 250 µm (b-e) 150 µm [21].*

Growth zone - steady-state lamellar growth

The structure in this region contains long, aligned lamellae of ice and ceramics. The fast freezing of a sample leads to fine ice crystals and small lamellae thickness of final ice-templated sample. Typical freezing velocities (freezing front velocities) which are used for ice-templating are in this steady state growth zone between $10 – 100\ mm \cdot s^{-1}$, which results in ice crystals typically between 2 mm and 200 mm long [23; 24].

Additives for controlling the structure

Controlling the structure at micron and submicron levels requires a manipulation of thickness and roughness of growing ice crystals. These features play a crucial role in the mechanical properties of final ceramic scaffold. The strategy, used for example by Munch et al. [25], was to use chemical additives that will affect the growth kinetics and microstructure of ice as well as topology of ice-water interface. They used various additives, such as dioxane, glycerol, sucrose, sodium chloride, citric water, or ethanol, to modify the microstructures (e.g. lamellar or cellular), surface roughness (e.g. faceted or dendritic), and interlamellar bridging of ice-templated scaffolds. Other authors such as Porter et al [18] investigated in their research effects of isopropanol addition to aqueous ceramic suspension, which resulted in elongated lamellar pores with periodic surface roughness and thick bridging. Pekor et al. [26] demonstrated that soluble polymers commonly used as plasticizers, such as

polyethylene glycol and polyvinyl alcohol, have a significant effect on the pore size and secondary dendrite arm spacing. Deville et al. [27] used zirconium acetate to limit the incorporation of water molecules into growing ice crystals, resulting in faceted polyhedral structures of ice-templated scaffold. Several research groups have demonstrated that pore-formers, such as polymer beads, sponges or salts, added to the suspension before freezing and removed after lyophilization by heating or dissolving create complex pore architectures with varied morphologies [25; 18].

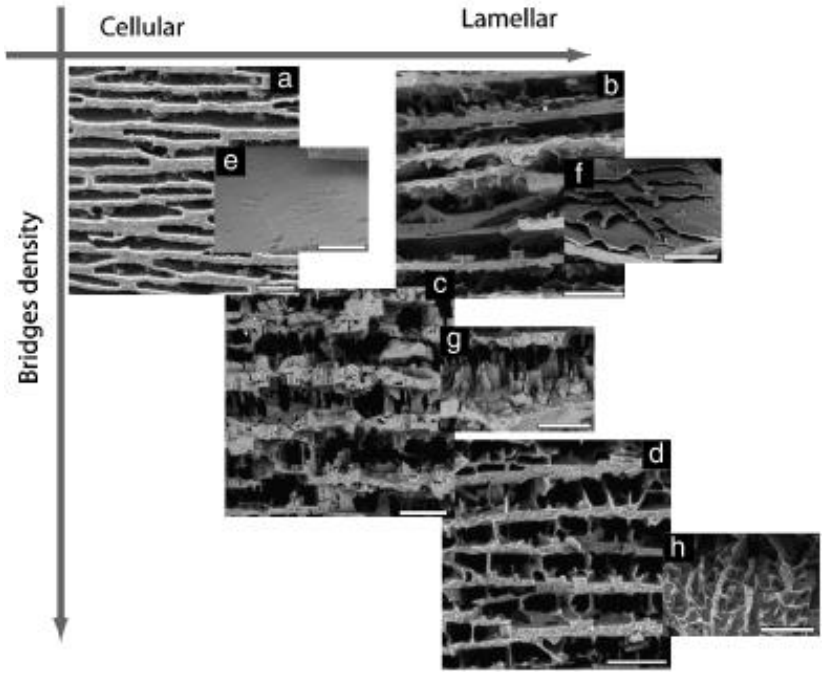

Figure 8. *SEM micrographs of ice-templated scaffolds showing the effect of additives on the architecture; (a) 10 wt.% sucrose in citric water, (b) 4 wt.% ethanol, (c) 4 wt.% sodium chloride, (d) 4 wt.% sucrose. Scale bars indicate: (a) 50 µm, (b) 100 µm, (c) 100 µm, (d) 50 µm, (e) 50 µm, (f) 100 µm, (g) 100 µm, (h) 100 µm [25].*

Different additives (to aqueous ceramic suspension) can change the structure of ice-templated scaffolds from lamellar to cellular, and roughness and density of interlamellar bridges can be manipulated, example is shown in Figure 8. Addition of 10 wt.% of sucrose in citric water with pH=2.5 (Figure 8a) resulted in a cellular structure with very smooth ceramic walls; 4 wt.% of ethanol addition resulted in a lamellar structure with smooth roughness (Figure 8b); 4 wt.% of sodium chloride addition resulted in a sharp-faceted lamellae surface (Figure 8c); and (d) 4 wt.% sucrose addition promoted a lamellar structure with microscopic roughness (Figure 8d) [25].

Structural defects

The presence or absence of structural defects is critical for mechanical response of the porous materials. Defects in ice-templated materials are obtained under certain conditions, which have not been fully clarified yet [28]. These defects are related to the development of so-called ice lenses: ice crystals growing perpendicular to the solidification direction, which adopt a crack-like morphology, see Figure 9. The appearance of ice lenses is mostly studied in geophysics, for their occurrence during freeze-thaw cycles of frozen soils [6].

The most appealing hypothesis [29] invoked to explain the formation of ice lenses is related to the development of residual stresses during the freezing (a result of the volume increase that accompanies the water to ice phase transformation), and mechanical resistance of the pack of

concentrated particles between ice crystals. The morphology of these defects is very similar to mechanically induced cracks, however that ice-lens type defects have only been observed after water is used. This may be explained by the negligible volume change upon liquid to solid phase transformation of all non-water base solvents [6; 29].

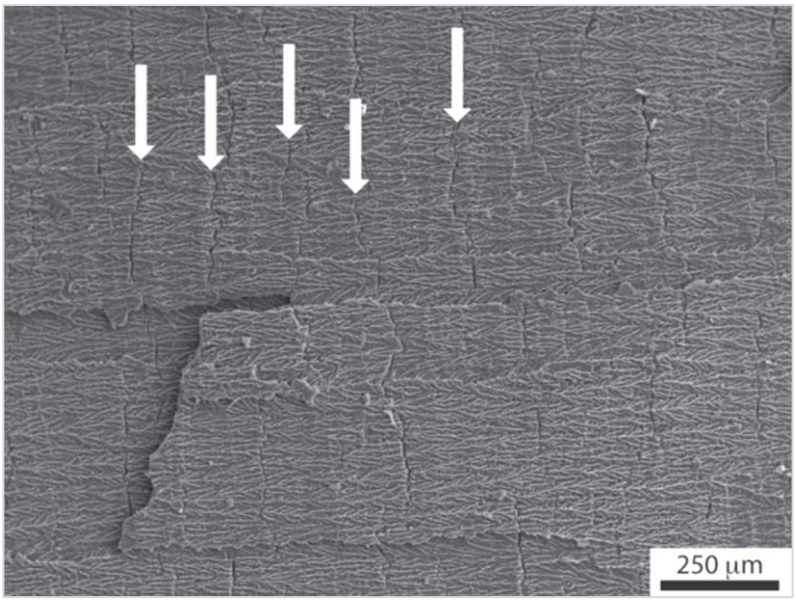

Figure 9. *Ice-lens type defects (arrows) in ice-templated alumina. Solidification direction was from the left to the right [6].*

Presence of such defects is very detrimental for mechanical strength of ice-templated scaffolds. The material is essentially pre-cracked and final mechanical strength, at a given porosity, is always low compare to defect-free ice-templated materials [6].

2.1.5 Ice-templating apparatus

Once a suspension with appropriate sedimentation properties and additives has been prepared, it is degassed and filled into a mold of ice-templating apparatus. Most experiments described in the literature use a single side freezing system [17].

Relatively simple apparatuses are commonly used for single side ice-templating experiments, whose representative is shown in the Figure 10. One side ice-templating apparatus is typically composed of polymer mold for suspension (PTFE, acrylic, PMMA or PVC are used most frequently) [30; 31; 32; 33], which is sealed by copper bottom plate and placed on copper rod, sometimes called cold finger [17; 31; 32; 33; 34]. This copper rod is immersed in a liquid nitrogen bath for sufficient cooling and equipped with thermocouple and heating elements for precise temperature control. The top of the polymer mold is commonly open, so that the upper surface of the suspension is exposed to the ambient atmosphere at room temperature [17].

The main disadvantage of this arrangement is that the ice-templated samples must have a simple shape and relatively small dimensions, because the cross section of ice-templated sample (perpendicular to the ice growth) should copy the shape and dimensions of the cold finger. This condition should be met due to the sufficient heat transfer from the suspension/ice templated sample.

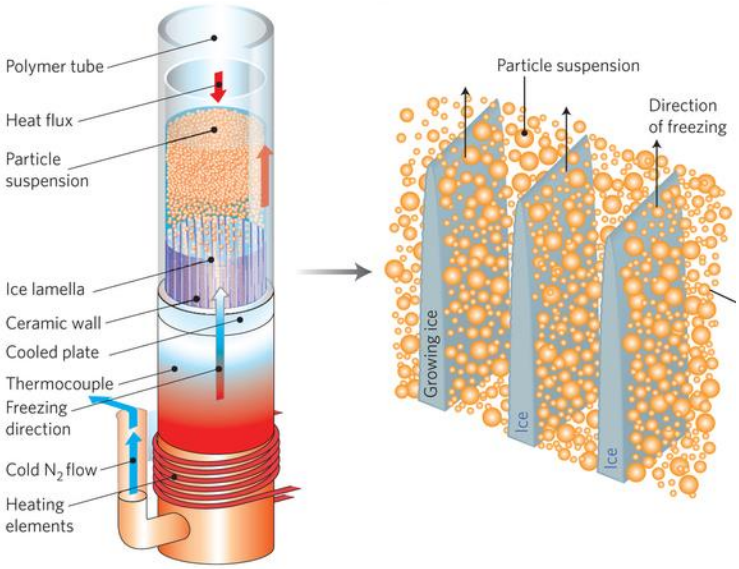

Figure 10. *Ice-templating apparatus for a single side ice-templating [30].*

If precise temperature gradient control during freezing is needed, another type of ice-templating - double side ice-templating can be used, see Figure 11. In double side ice-templating the freezing kinetics is controlled by heaters placed on the copper cold fingers and thermocouples placed on each side of the polymer mold with suspension. Freezing can occur from top, bottom or from both sides of the mold. By adjusting both temperature gradient and cooling rate, a wide range of freezing conditions can be achieved. For low freezing rates, only one cold finger can be used. To reach higher freezing rates, a constant macroscopic temperature gradient can be established using the two cold fingers cooled at the same rate [31].

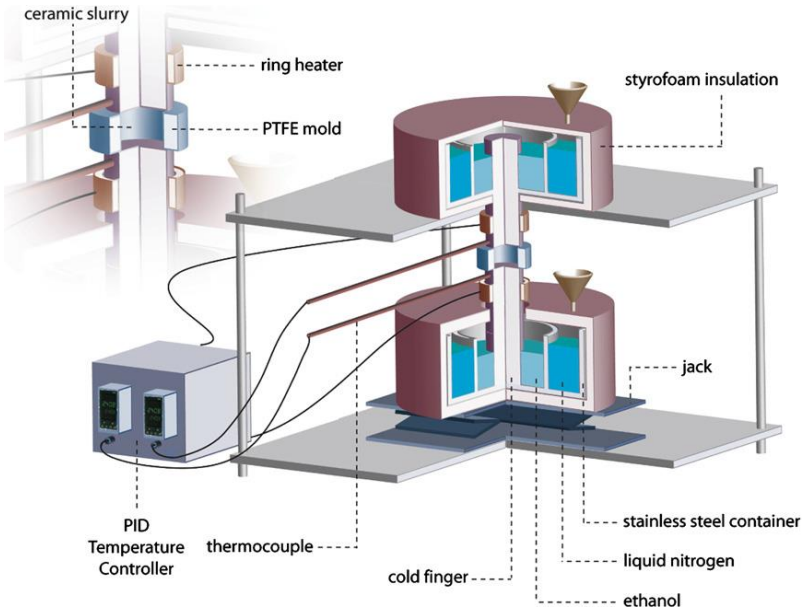

Figure 11. *Ice-templating apparatus for double side ice-templating [31].*

Magnetic ice-templating is another variation of ice-templating, as it was demonstrated by Porter et al. [32]. They prepared samples by using a custom built ice-templating unit with rotating permanent magnet. Figure 12 shows the magnetic ice-templating setup. The ice-templating

apparatus consists of a copper cold finger immersed in a liquid nitrogen bath, and a band heater and thermocouple linked to a PID controller are attached to the copper cold finger in order to control the cooling rate of the copper surface at the bottom of a mold. The rotating permanent magnet is constructed from a 1.32 T neodymium magnet (2.5x10x10 cm^3). Two cast iron channel arms, threaded stainless steel rods, and cast iron flux path distributors are attached to the neodymium magnet to direct and concentrate the magnetic flux path through the mold perpendicular to the ice growth direction (Z-axis). The magnetic field strength can be varied from 0 to 0.15 T by adjusting the distance of the flux path distributors with the threaded rods. The permanent magnet device is rotated by a vertical aluminum shaft connected to a stepper motor [32].

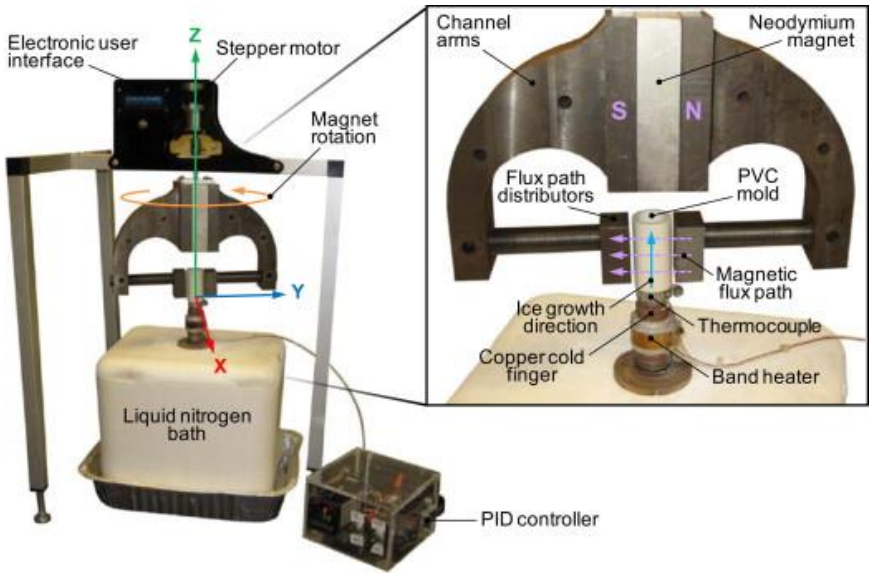

Figure 12. *Ice-templating apparatus for magnetic ice-templating [32].*

2.1.6 Freeze-drying

Freeze-drying also known as lyofilization is the last step of ice-templating process in which the frozen solvent is removed from the scaffold by sublimation.

Freeze-drying is widely used process for drying and improving the stability of various pharmaceutical products including: viruses, vaccines, proteins, peptides, or colloidal carriers: liposomes, nanoparticles, nano-emulsions. This process is relatively slow and expensive, so it is applied only for products having a high added value. Freeze-drying cycle in terms of ice-templating can be divided into two stages: primary drying (ice sublimation) and secondary drying (desorption of unfrozen water) [35].

Some suspensions for ice-templating can contain sucrose or other sugars as structure modifiers and the transition glass is present during freeze-drying. Therefore it is important to consider effects of temperature and moisture content on glass transition temperature T_g. Solid/liquid state representation of the binary system water-sucrose is shown in the Figure 13, displaying how the phase composition of an initially dilute solution (A) changes with temperature during freezing and subsequent drying [36].

The important point to note is that, despite the predictions of classical phase equilibrium, sucrose does not precipitate as a crystal phase, when its solution is cooled to the eutectic point T_e,

but becomes subject to progressive supersaturation. As the freezing process continues, more and more water in the suspension freezes. This results in increasing saturation of the remaining liquid, and liquid solution becomes more concentrated, its viscosity increases inducing inhibition of further crystallization. This highly concentrated and viscous liquid solidifies, yielding an amorphous, crystalline, or combined amorphous-crystalline phase. The small percentage of water that remains in the liquid state and does not freeze is called bound water [35; 36].

Once ice and supersaturated solution (glassy phase) reaches its limiting composition, ice sublimation can be started, but it must be performed at, or below T_g'. If the temperature is higher than T_g ice will melt back into solution, causing a dramatic drop in its viscosity, with damaging and irreversible consequences on the freeze-dried scaffold [35].

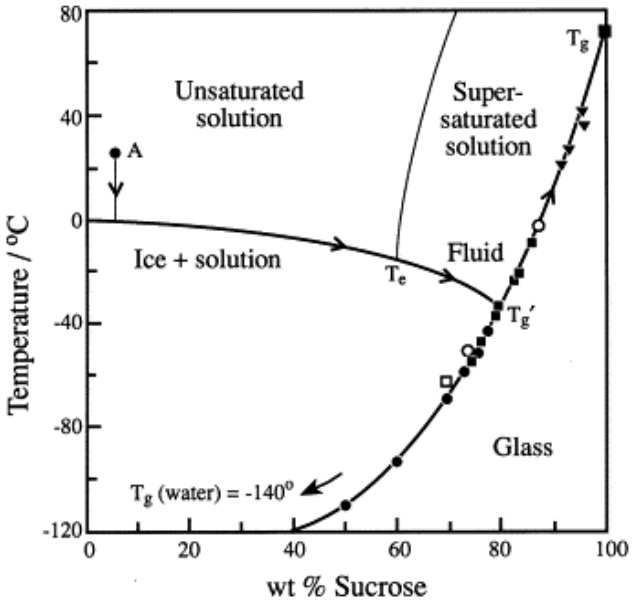

Figure 13. *Phase diagram for a binary system of sucrose-water showing glass transition temperature Tg' [36].*

The point of intersection of the freezing and glass curves, T_g', depends on solution composition, but not on its initial concentration. The vapor pressure of ice which provides the driving force for water removal increases logarithmically with increasing temperature. However, from economic reasons the ice sublimation stage should be performed at as high temperature as possible. Therefore, the correct sublimation temperature depends on the composition and in practice, T_g' values above −40 °C should be aimed [35].

Primary drying

The primary drying stage involves sublimation of ice from the frozen sample. In this process heat is transferred from a supporting shelf to the frozen sample and conducted to the sublimation front. Consequently ice sublimes and formed water vapors pass through the dried portion of the sample to its surface, where it is transferred through the vacuum chamber to a condenser (cold trap). In the cold trap water vapor is condensed and forms ice again. Green porous ceramic scaffold is formed at the end of sublimation step and its pores correspond to spaces previously occupied by ice crystals [35].

Secondary drying

Secondary drying involves the removal of absorbed water from the green product. Part of the water is not separated out as ice during the freezing, and did not sublimate off during first stage [37]. A typical production scale freeze-dryer (Figure 14) consists of a drying chamber containing temperature- controlled shelves, which is connected to a cold trap via a large valve. The cold trap is containing plates or coils capable of being maintained at very low temperature (less than −50 °C). One or more vacuum pumps in series are connected to the cold trap to achieve pressures in the range from 4 to 40 Pa in the entire system during the operation [35; 38].

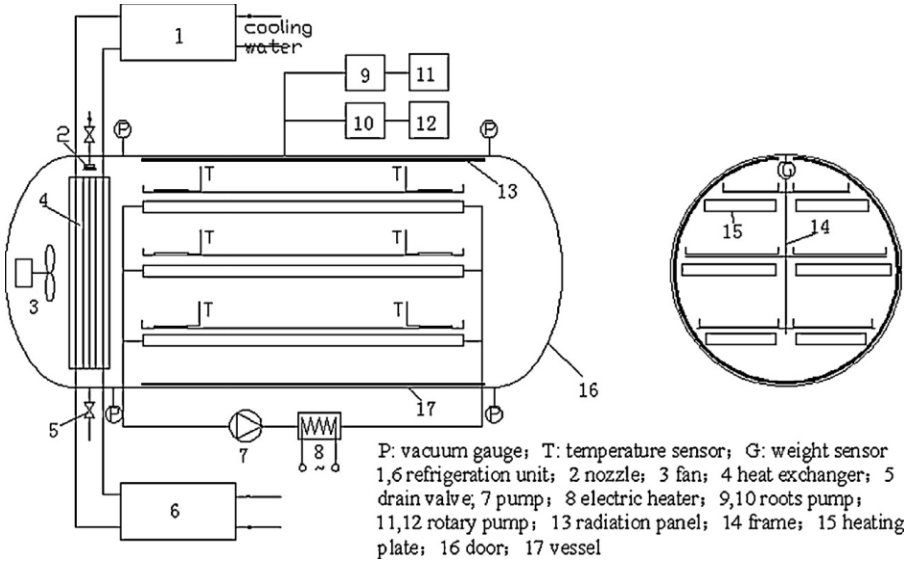

Figure 14. *Schematic illustration of production scale Freeze-dryer [38].*

2.2 Sintering

The dominant method of final fabrication of ceramic green bodies after the shaping is pressure less sintering. Shaping processes involve powder mixture, suspension, or plastic material which is formed into a shape. It is generally desirable to reach green bodies with high density and homogeneous microstructure (pore size distribution), because the low green density causes high sintering shrinkage and moreover large (supercritical) pores have to be eliminated during sintering at high temperatures (to reach high final density), causing unwanted grain growth. Generally there are several shaping methods for advanced ceramics, one group is classified as dry and traditional, namely die pressing or cold isostatic pressing (CIP). Slip casting and extrusion, tape casting and injection-molding processes are classified as wet and high-tech forming processes [1].

Dry powder compaction methods used to create a green body by an application of external mechanical pressure. This application of pressure significantly affects the homogeneity of the green body and thus also densification and grain growth during sintering stage, because of inhomogeneous pressure distribution inside the green body. Application of external pressure also brings shape limitations due to the necessity of pressing die. On the other hand, so called wet shaping methods benefit from the homogeneous arrangement of particles in the suspension, and therefore tailoring of final microstructure is easier. [8].

Sintering process converts the green body microstructure to microstructure of the dense or porous ceramic components. Sintering step is the last processing step, where the final microstructure

of the ceramic sample can be influenced. The sintering process consists of solid particle bonding or neck formation, followed by continuous closing of pores from a large open porosity to essentially pore-free bodies [1].

The driving force of sintering is reduction of the total Gibbs free energy of the system. It takes place, in the most general description, as the transformation of energetically inconvenient interface solid/gas to energy-favorable solid/solid interface. The total interfacial energy of a powder compact is expressed as γA, where γ is the specific surface (interface) energy and A the total surface (interface) area of the compact. The reduction of the total energy can be expressed as

$$\Delta(\gamma A) = \Delta\gamma A + \gamma \Delta A \tag{2.7}$$

Here, the change in interfacial energy ($\Delta\gamma$) is due to densification and the change in interfacial area is due to grain coarsening. For solid state sintering $\Delta\gamma$ is related to the replacement of solid/gas interfaces (surface) by solid/solid interfaces. As it is schematically shown in Figure 15, the reduction of total interfacial energy happens via densification and grain growth, the basic phenomena of sintering [2].

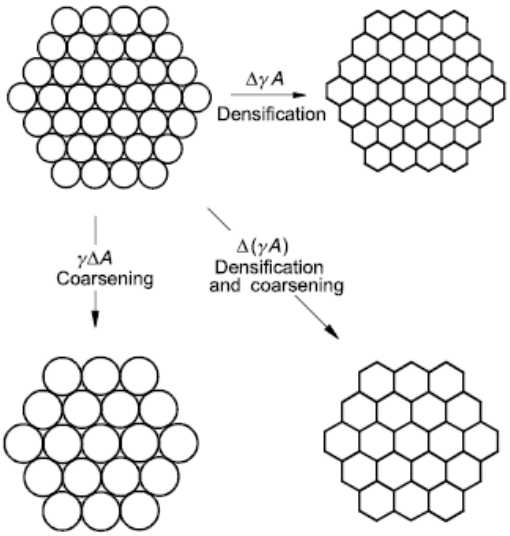

Figure 15. *Schematic illustration of the sintering process [2].*

Sintering behavior of ceramics after freeze-pressing

Sintering behavior of ice-templated ceramics is influenced by the expansion of water during the freezing. This phenomenon is usually called as freeze-pressing and should be taken in account, when designing appropriate sintering cycle. Freeze-pressing should be a new alternative method of applying mechanical pressure inside a suspension. Ceramic suspension itself is not externally compressible, but ceramic particles should be compressed by growing ice crystals in freezing water-based ceramic suspension. The ice expansion creates mechanical pressure for powder compaction due to the physical properties of water and ice. The idea of using the pressure of growing ice crystals to break rocks was already known to our ancient ancestors, but the idea to use this enormous pressure for compaction of ceramic powder was brought by Salamon et al. in 2011 [8]. In their work controlled ice formation was used for compaction of Al_2O_3 particles inside the suspension. This study showed possibility of controlled aggregation of powder by freezing and thawing with no shape

limitations for a final product. This method also showed high homogeneity of pressed powder as opposed to conventional pressing methods. Schematic illustration of ceramic particles packing by freeze-pressing is showed in Figure 16.

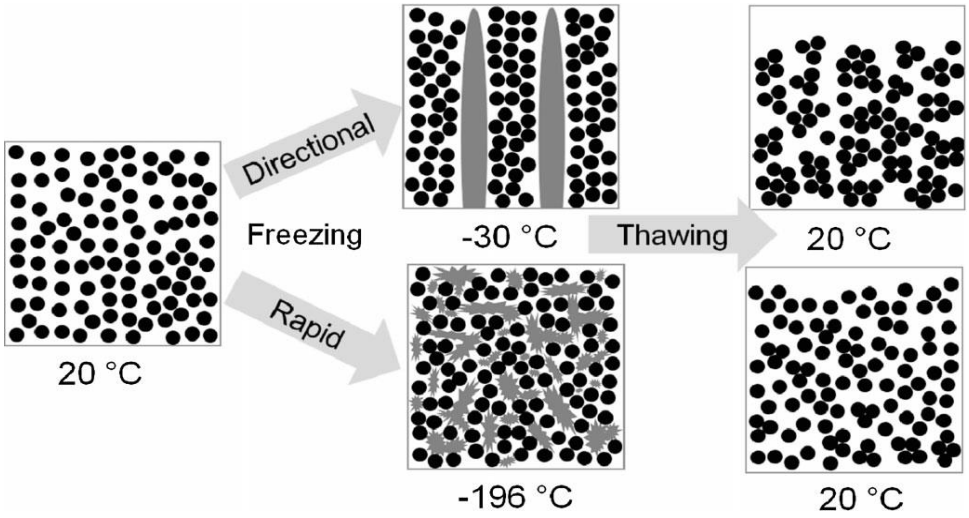

Figure 16. *Schematic illustration of initial particle packing in ceramic suspension, after directional freezing and rapid freezing [8].*

Salamon et al. [8] also reported different sintering behavior of freeze-pressed samples in comparison with conventionally prepared samples (tape casting, cold isostatic pressing). A possibility to manipulate sintering behavior of ceramics by freeze-pressing brings new routes to create composite materials. Freeze-pressing should open a new way to combine materials with different volume changes during sintering due to shifts of sintering kinetics of freeze-pressed materials. These shifts of sintering kinetics of α-Al_2O_3 samples prepared by different methods reported by Salamon et al. are shown in Figure 17.

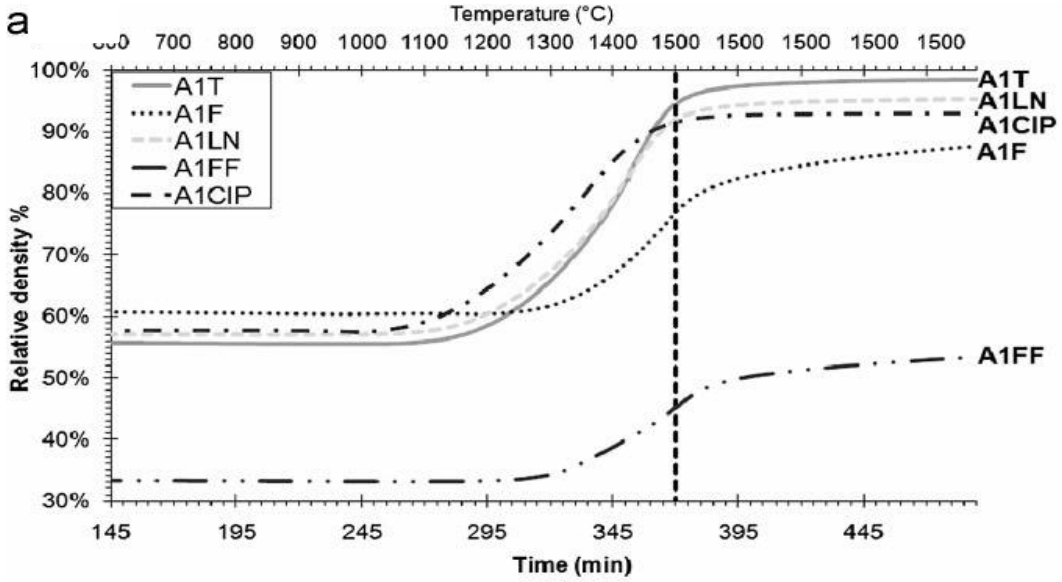

Figure 17. *Densification of raw α-alumina powder (samples were dried at open air conditions); T – tape cast; LN – freeze-pressed sample in liquid nitrogen; CIP – cold isostatically pressed dry powder; F –directionally freeze-pressed sample at -30 °C; FF – freeze-dried sample after freeze-pressing [8].*

2.3 Ice-templating + indirect 3D printing for bioceramic scaffolds fabrication

During the last decades there has been a growing interest on using hydroxyapatite (HAP) or beta-tricalciumphosphate (β-TCP) as a bone graft replacements because of their excellent biocompatibility and bioactivity. Biological activity of these bioceramic materials depends on a combination of physical and chemical characteristics that are strongly related to their microstructure [39]. For example, in order to promote the vascularization and diffusion of nutrients necessary for tissue regeneration, bone graft replacements have to be manufactured as highly porous structures (i.e. scaffolds) [39; 40; 41; 42]. Scaffold porosity has to be interconnected with a minimum pore size of at least 300 mm for successful bone tissue growth within the whole volume of an implant [43]. However, while porosity plays a crucial role in scaffold functionality, it also lowers its mechanical performance [39; 40; 44].

Additive manufacturing is promising approach to produce porous scaffolds that meet all the requirements in terms of pore size, shape and interconnectivity for bone cell growth, while maintaining the mechanical properties as high as possible. Additive manufacturing, also known as solid freeform fabrication, rapid prototyping or 3D printing, is a general term involving all techniques that enable production of structures via the sequential delivery of energy and/or materials according to a computer-aided design (CAD) [45; 46]. In contrast with conventional porous scaffolds production technologies, Additive manufacturing allows precise control over both macrostructure and microstructure with a high degree of reproducibility and homogeneity [47; 48]. Hence, the mechanical properties of the scaffolds can be tailored by design. Moreover, the straight forward translation from CAD to CAM allows tailoring the scaffolds to meet specific needs of each patient [45; 49].

However, Additive manufacturing techniques also exhibit certain limitations, for example printing resolution and architectural control are often highly dependent on the selected material and technique. For example, in the case of nozzle-based systems the resolution, and thus the pre designed porosity features, is highly dependent on the nozzle diameter [45; 46].

A suitable strategy to overcome these limitations and produce multi scale porosities is to combine and additive manufacturing technique with a conventional method for fabricating porous structures [45; 50; 51]. This approach, called indirect rapid prototyping, combines structures manufactured by additive manufacturing techniques, as a mold or sacrificial template for the final scaffold, with conventional techniques. The use of additive manufacturing allows production of scaffolds with a well-defined 3D shape and an interconnected pore network while the conventional method allows the creation of additional hierarchical porosity in the scaffold [45; 49; 52; 53; 54]. In this sense, the combination of widespread, low-cost 3D printing by fused deposition modeling (FDM) with ice-templating can be a good alternative.

2.4 Ceramic/ceramic composites

The most widely used ceramic/ceramic composites are based on ceramic fibers embedded in ceramic matrix. These types of materials are commonly categorized as “ceramic matrix composites” (CMC), “continuous fiber ceramic composites” (CFCC), and “ceramic fiber-matrix composites” (CFMC). The main advantage of ceramic/ceramic composites is their toughness and damage tolerance, compared to monolithic ceramics. Currently the most advanced ceramic/ceramic composites are based on silicon carbide fibers, but their lifetime is limited by susceptibility of SiC to

oxidation and degradation in oxidizing atmospheres at elevated temperatures. To overcome these limitations, oxide based ceramic constituents can be used for preparation of ceramic/ceramic composites, in addition manufacturing costs of such composites can be significantly lower. The main drawback of oxide/oxide composites is reduced mechanical performance compared to non-oxide ones [55].

The main requirement for a tough ceramic composite is crack deflection at or near the fiber/matrix interface. The two basic mechanisms used for crack deflection in ceramic/ceramic composites are the use of sufficiently weak (porous) matrix or use of a weak engineered interphase, which typically involves fiber coating [56; 55] Typical appearance of CMCs with porous matrix and weak engineered interphase is shown in Figure 18.

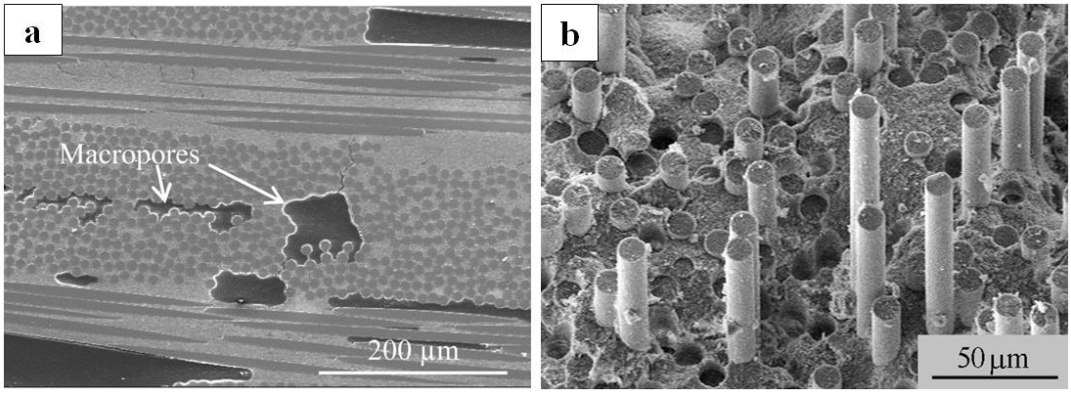

Figure 18. *Typical microstructures of CMCs with: a) porous matrix (Nextel™610/alumina composite) [57]; b) weak engineered interphase (Nextel™610/Monazite ($LaPO_4$)/alumina composite [58].*

Ice-templating hasn´t been used very widely for preparation of ceramic/ceramic composites until now. There were several attempts to use this process in fabrication of oxide fiber reinforced composites with porous matrix. For example Mah et al. [59] used freeze drying of camphene based alumina/YAG slurries impregnated in Nextel™610 fabrics to reduce cracking of ceramic matrix during manufacturing of composites.

Whole ice templating process with controlled freezing rate of water based zirconia/YAG suspension, for fabrication of Nextel™610/zirconia/YAG composite, was used by Wamser et al. [60]. In this work, ice-templating was implemented as way to produce porous ceramic matrix with no shrinkage during sintering. A glycerol and gelatin were used as ice-templating suspension additives to change size and morphology of growing ice crystals. The appearance of final sintered ceramic/ceramic composite is shown in Figure 19.

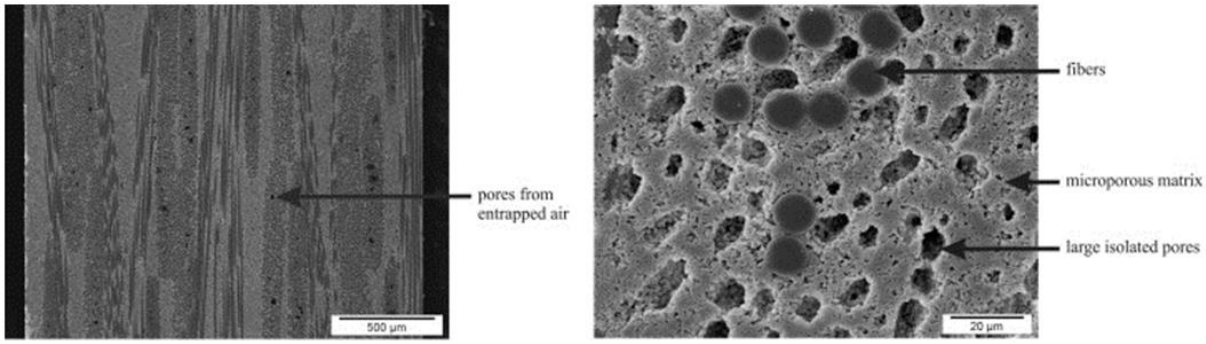

Figure 19. *Microstructure of Nextel™610/zirconia/YAG composite prepared by ice-templating process [60].*

2.5 Ceramic/polymer (hybrid ceramic) composites

Hybrid ceramic composites are based on mimicking natural materials, especially nacre. Nacre is very lightweight structural composite composed of inorganic minerals embedded in an organic matrix with very sophisticated structure and complex design. Its mechanical properties far exceed what could be expected from a simple mixture of their components. Many of the complex architectural features observed in nacre provide its simultaneous strength and toughness, properties that are generally considered mutually exclusive [18; 61].

One of the most important properties of materials used for ballistic protection is their fracture toughness (resistance to the initiation and growth of a crack) and nacre exhibits very high fracture toughness, although it is made of very brittle material. Nacre consists of 95 vol. % of layered aragonite ($CaCO_3$) bonded by a thin layer of organic material, that acts as a glue. Such arrangement of aragonite exhibits a toughness three orders of magnitude higher than $CaCO_3$ itself [61].

Ice-templating is a great way to fabricate synthetic architectural features that emulate the strengthening and toughening mechanisms found in natural materials as nacre. To date Munch et al. [61], Launey et al. [62] and Liu et al. [63] have developed the most promising ceramic composites that mimicking nacre by ice-templating method. Munch et al. [61] created a porous ceramic scaffolds made of Al_2O_3 and subsequently infiltrated them with polymethylmetacrylate (PMMA). This Al_2O_3/PMMA composite had lamellar or "brick and mortar" (after subsequent pressing of lamellar materials) structures similar to natural nacre, see Figure 20. They also made some experiments with addition of sucrose to ceramic suspension. Addition of sucrose created a microscopic roughness on the ceramic lamellae, which had positive impact on fracture toughness of the composite.

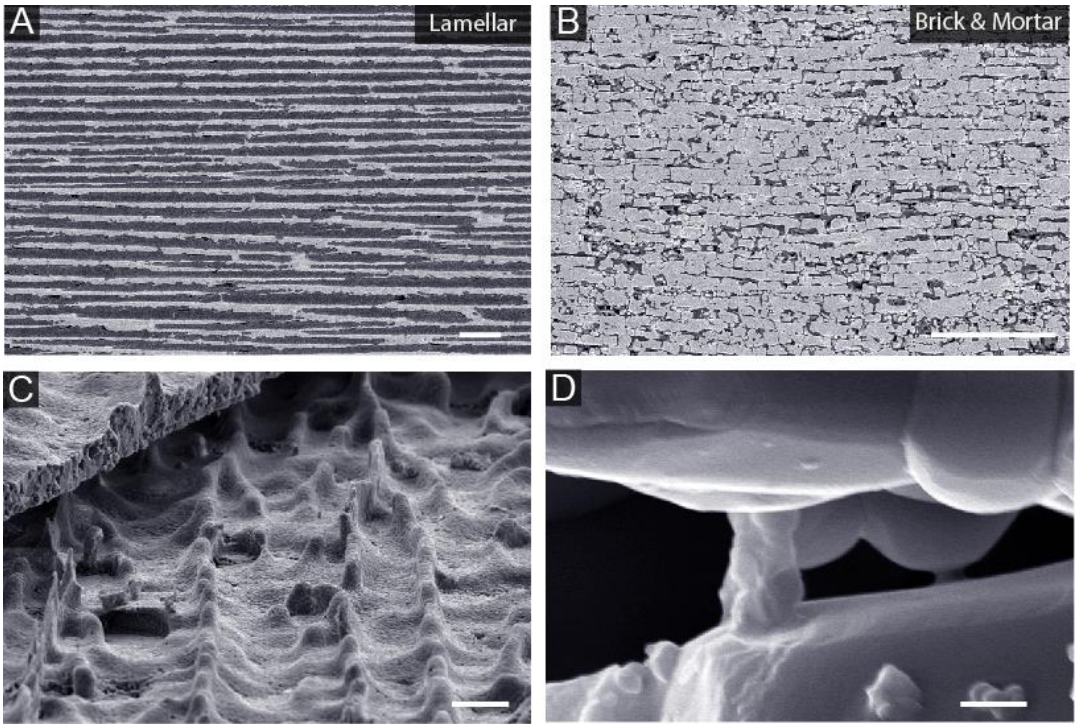

Figure 20. *Structure of ice-templated alumina; (A) Al_2O_3/PMMA lamellar composite (the lighter phase is the ceramic; the dark phase is the polymer). (B) Brick-and-mortar architecture. (C) Microscopic roughness in the ceramic walls caused by addition of sucrose. (D) Ceramic bridges between lamellae formed due to the trapping of ceramic particles by the growing ice [61].*

In case of hybrid ceramic composites, the objective is to allow stress relaxation by combining a strong and hard (ceramic) phase with soft (polymer or metal) layer in between. The nacre-like PMMA/alumina materials in particular showed remarkable R-curve behavior, thus indicating that they are tolerant to the stable growth of cracks, with a fracture toughness of 30 MPa·m½ or more and flexural strength of 160 MPa (several times higher in energy terms than those of either the constituent ceramic or polymer, see Figure 21). Furthermore, they were 1.5-2 times more ductile than nacre, and twice as strong. In fact, such hybrid alumina ceramics approach the specific strength and toughness of aluminium metal alloys while exhibiting lower density and higher stiffness [30].

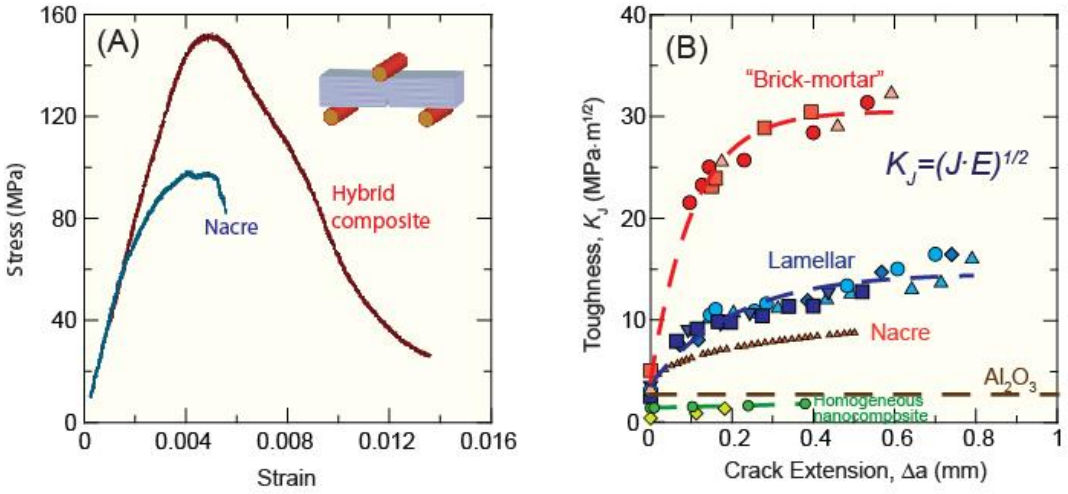

Figure 21. *Mechanical properties and crack growth of the synthetic hybrid composites [61].*

2.5.1 Ceramics/polymer adhesion

Most of industrially used polymer resins for composites manufacturing have low surface energy and a lack of polar functional groups on their surface, resulting in poor adhesion properties. Therefore, because adhesive bonding is a surface phenomenon, preparation prior to bonding is important for the development of strong, durable adhesive joints [64; 65].

The contact between ceramic scaffold and infiltrated polymer plays a significant role on mechanical properties of final composite. Improving the adhesion between scaffold and polymer includes surface treatment of ceramics. The main purpose of the surface treatment is to remove weak boundary layers (oils and greases, or glassy phases) from the surface to maximize the degree of molecular contact between the ceramic surface and the polymer, and to ensure that the intrinsic adhesion forces across the interface are sufficient to achieve adequate bond strength [66].

There are several methods to prepare ceramic surfaces, apart from degreasing and cleaning, for adhesive bonding e.g. roughening, acid etching, plasma activation, laser ablation, sol-gel and silane treatment, and chemical grafting [66; 67].

Roughening

Roughening of the surface is important in achieving higher adhesion strength as it helps to create stronger and more durable bonds, and also provides larger surface area for the adhesive to grip. For ceramic materials, sand (or grit) blasting (sometimes also called airborne-particle abrasion) is superior to sand paper, or emery cloth [64; 67].

The effects of various roughening treatments on the bond strength of porcelain materials were studied by Thurmond et al. [68]. Results of this work discovered that grit blasting creates better adhesion strength as it removes loose substances on the bonding interface as well as increases the surface contact area.

Acid etching

The main reason for acid-etching treatment is to apply acid on a ceramic surface in order to create pores for a better bond strength of an adhesive to the surface of ceramics. Because ceramic materials are generally very difficult to etch, very concentrated acids at elevated temperatures have to be used. Mostly used acids include hydrofluoric, phosphoric, sulfuric and hydrochloric acids. However, as it was pointed out for example by Kato et al [69] the acid-etching process is not always beneficial to the enhancement of surface bond strength. Acid residues from etching process tend to remain in the surface pores of ceramics and can subsequently damage the adhesive layer and weaken or cause failure of the bond. There is also a health concern due to use of concentrated acids at elevated temperature especially in case of hydrofluoric acid (HF) [64].

Plasma activation

Lately, there were several studies dealing with plasma ceramic surface treatment to improve adhesion and bonding strength between ceramics and polymer. Several studies [70; 71; 72] revealed that the main effect of plasma treatment is that the ceramic surface after plasma activation showed decreased content of C–C bonds, suggesting that organic matter was removed. By contrast, the content of oxygen-containing polar groups increased (C–O–C and O=C–O), suggesting that plasma treatment enhanced the surface hydrophilicity. However the plasma activation is less effective than acid etching or silane treatment.

Laser ablation

Recent studies have shown that laser treatment of the ceramics surface can result in improvement of bonding strength due to the ultraviolet radiation absorption at the top surface layer which could cleans up surface contaminants such as fluorocarbons and silicones completely Laser treatment also provides effective mean for structuring ceramic surfaces via the action of ablation, although the effectiveness of laser ablation is very dependent on the laser type (wavelength of the radiation) and on type of ceramics [64; 67].

Silane treatment

Silanes are very effective in adhesion promotion between resin composites and silica-based or silica-coated ceramics. It is generally accepted that for non-silica-based ceramics, surface treatment is necessary preliminary step to increase silica content and then, with help of silane, improve resin bonding [73].

Silane groups usually have two different reactive groups. One group is reactive to the substrate and the other to the adhesive. In terms of how silane coupling agents work, silicon-hydroxyl (silanol) groups are formed in the bonding process with silanes, this would then form bonds with inorganic surface hydroxyl groups from substrates by covalent or hydrogen bonding, and thus promote the adhesion strength. The organic group on the silane is typically a reactive group with which the polymer resin will react or interact [64; 67].

The adhesion mechanism of polymer resin to ceramic surface after silane treatment is shown in Figure 22.

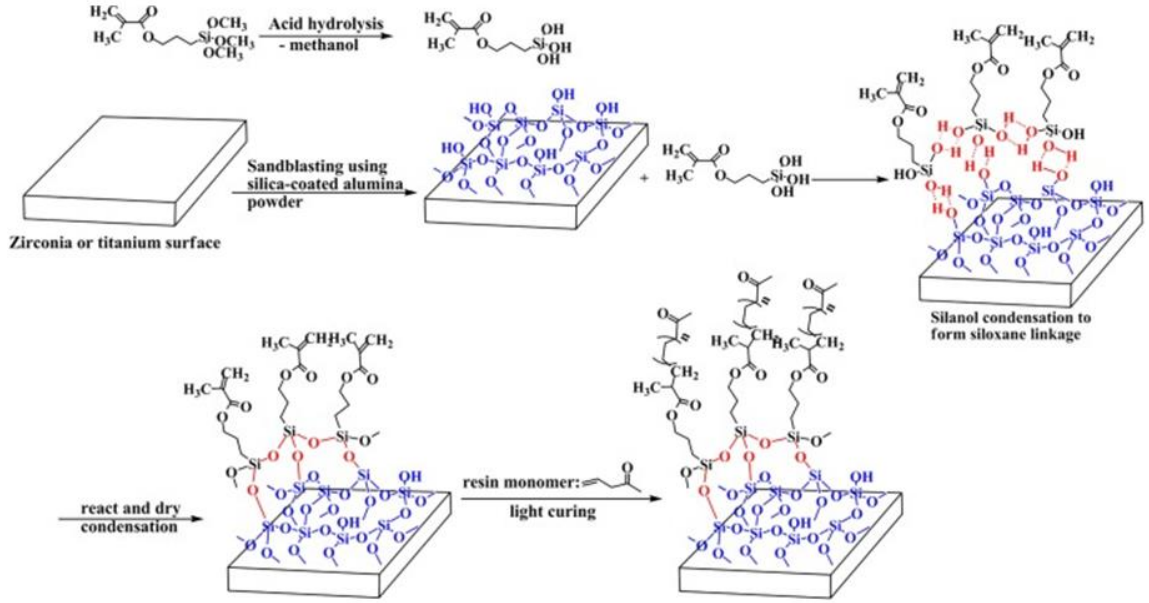

Figure 22. *Adhesion mechanism of polymer resin bonding to silica coated ceramic surface by an application of silane coupling agent [73].*

The application of silane coupling agents on ceramics is mainly found in dental area and this treatment is almost in all cases accompanied by grit blasting. For example silica-coated alumina particles were used by Lung et al. [74] to produced greater surface roughness and enrich ceramic surface with silica to enhance bonding to resin via silane coupling agents. Generally, good bonding of polymer resin to ceramic surface after silane treatment can be achieved when there is adequate amount of SiOH sites on initial ceramic surface [64].

The silane treatment of ice-templated scaffolds was performed by Munch et al. [61]. Chemical grafting was used in this work to improve cohesion between ice-templated Al_2O_3 scaffold and infiltrated PMMA resin.

3 Aims of Thesis

As existing structural materials reach their performance limits, one of the major scientific challenges for the 21st century is the development of new stronger and tougher lightweight structural materials. One approach in this quest for the design of new and superior structural materials is by mimicking the architecture of natural/biological materials and structures.

The main goal of this Ph.D. dissertation work is to master ice-templating technique for relatively large samples compare with current state of art. New technique should be adopted for preparation of hybrid ceramic composites. The expected results will stimulate development of new porous materials directly designed for specific applications.

The main objective of the dissertation work will be fulfilled via the following partial goals:

1. Development of ice-templating apparatus suitable for large samples compare with current state of art.

2. Preparation of suitable ceramic suspensions and description of their behavior during ice-templating.

3. Evaluation of mechanical properties of ice-templated samples based on microstructure.

4. Preparation of hybrid ceramic/polymer composites and evaluation of their mechanical performance.

4 Materials and methods

4.1 Ice-templating suspensions

Several ceramic powders, see Table 2, were used for preparation of ice-templating suspensions and for ceramic/ceramic composites manufacturing. The majority of ice-templated scaffolds were prepared from alumina and hydroxyapatite powders. Several suspension additives (sugar, dextrin, maltodextrin and starch) were tested to improve mechanical properties of the ice-templated scaffolds and to control the micro roughness of lamellae surfaces. A sugar (sucrose) in concentration of 3 wt.% appeared to be the best additive in terms of resulting microstructure of the ice-templated scaffolds and green body mechanical stability, sufficient for manipulation with samples.

Table 2. *Selected properties of applied ceramic powders.*

Compound	Density [g·cm^{-3}]	Average particle size D_{50} [nm]	Purity [%]	Designation	Producer
α-aluminium oxide (α-Al_2O_3)	3.99	390	99.5	AES-11C	Sumitomo
Yttria stabilized zirconia (ZrO_2)	6.05	300	94.3	CY3Z-RS	Saint Gobain
Yttria stabilized zirconia (ZrO_2)	6.08	80	94.7	TZ3YSE	Tosoh
Hydroxyapatite (HAP)	3.16	-	≥ 90.0	$Ca_5(OH)(PO_4)_3$ p.a.	Sigma – Aldrich

Alumina suspensions

Water-based ice-templating suspensions were prepared from alumina powder Sumitomo AES-11C. Suspension´s solid loading was varied from 25-50 vol.% of Al_2O_3. Final composition of ice-templating suspension with 45 vol.% of alumina powder, used for preparation of hybrid ceramic/polymer composites, is shown in Table 3.

Table 3. *Composition of suspension with 45 vol.% of Al_2O_3 used for ice-templating.*

Compound	Weight [g]	Volume [cm^3]	Density [g·cm^{-3}]	Weight fraction [wt.%]	Volume fraction [vol.%]
Al_2O_3 powder	180.00	46.15	3.99	73.50	44.70
Polyvinylacohol	1.05	0.81	1.30	0.40	0.80
Water	51.55	51.55	1.00	21.10	50.00
Darvan C-N	4.00	3.64	1.10	1.60	3.50
Octanol	0.83	1.00	0.83	0.30	1.00
Sugar	7.32	-	1.59	3.00	-

The dynamic viscosity was measured to characterize ice-templating alumina suspensions with various solid loadings. Results of these measurements are shown in Figure 23.

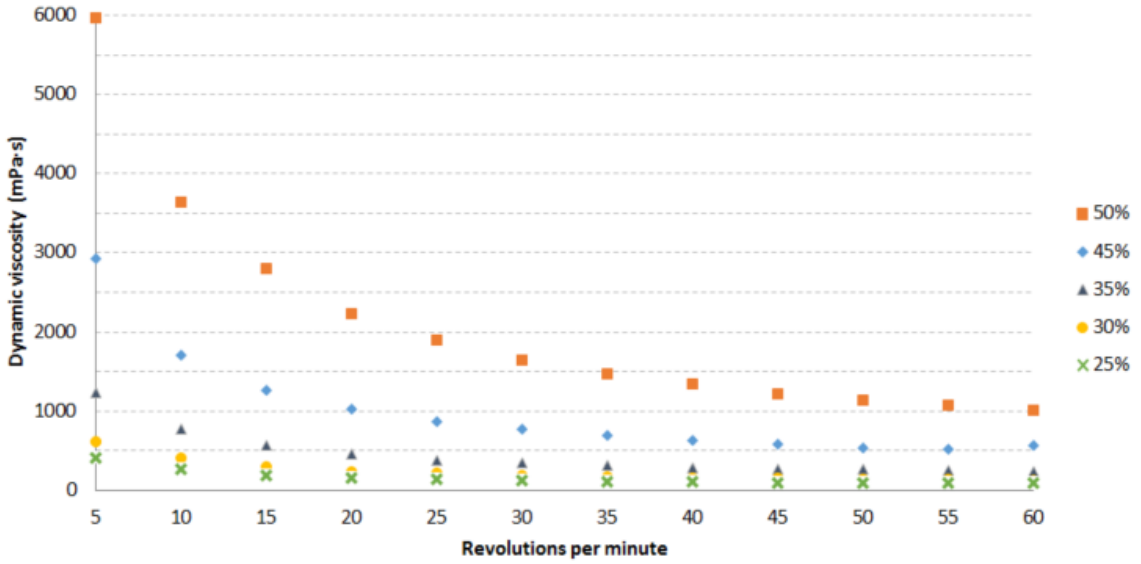

Figure 23. *Dynamic viscosity of ice-templating alumina suspensions with the various solid loading.*

HAP suspensions

Water-based suspensions for ice-templating were prepared from calcined HAP powder with solid loadings from 7.5 vol.% to 20 vol.% of calcined HAP powder. The composition of selected ice-templating suspension with solid loading of 15 vol.% of calcined HAP, used for preparation of ceramic/ceramic composites is shown in Table 4.

Table 4. *Composition of ice-templating suspension with 15 vol.% of calcined HAP powder.*

Compound	Weight [g]	Volume [cm^3]	Density [$g \cdot cm^{-3}$]	Weight fraction [wt.%]	Volume fraction [vol.%]
HAP powder	30.00	9.74	3.16	34.08	15.10
Polyvinylalcohol	1.10	0.85	1.30	1.25	1.10
Water	51.50	51.50	1.00	58.50	80.70
Dolapix CE64	2.00	1.82	1.10	2.22	2.80
Octanol	0.83	1.00	0.83	0.94	1.00
Sugar	2.60	-	1.59	3.00	-

4.2 Ice-templating process

4.2.1 Ice-templating apparatus

Conventionally used ice-templating and freeze-drying apparatuses (with copper cold finger submerged in liquid nitrogen bath) were not suitable for our production of ice-templated scaffolds, especially in terms of samples dimensions and shape variability, thus it was necessary to design, develop and manufacture our own customized ice-templating apparatus. Our effort on this topic was

successful and we put in practice our customized version of the ice-templating apparatus, which is productively used and allows us to scale up easily the size of ice-templated samples and to change their shape without any modifications of the ice-templating apparatus itself. The final version of ice-templating/freeze-drying apparatus is shown in Figure 24.

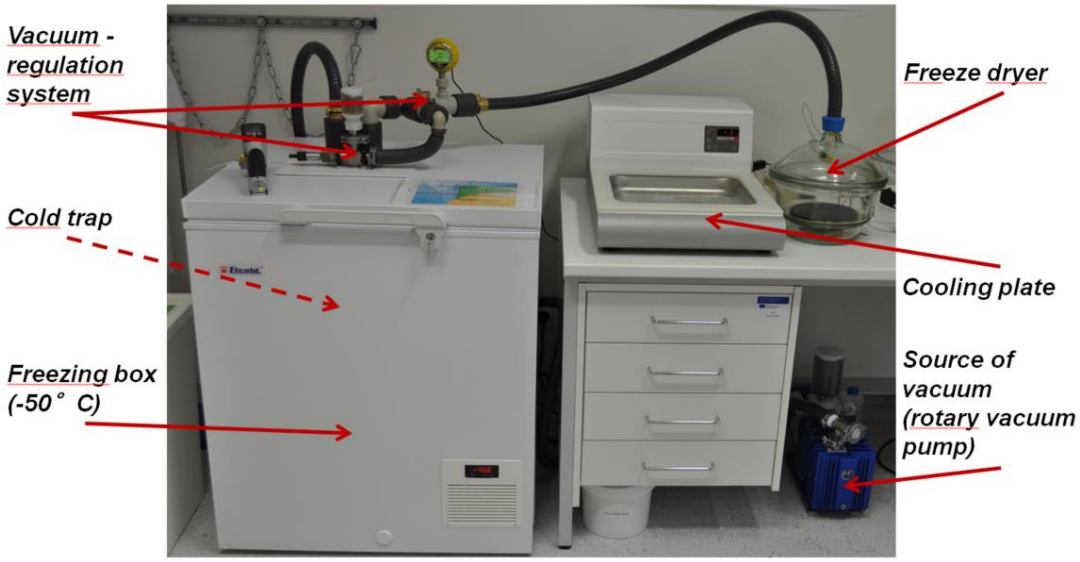

Figure 24. *Design of our customized ice-templating apparatus.*

4.2.2 Ice-templating vessels

All types of ice-templating vessels were designed to maintain controlled heat transfer during the freezing step and thus obtain the desired microstructure if ice-templated bodies. Ice-templating vessels with complex porous structure of walls were designed in 3D CAD software and subsequently printed on a FDM 3D printer (Felix 3.1, FELIX printers, Netherlands). Polylactic acid (PLA, Plasty Mladeč), in pure form and/or with various additives, was used as the printing material.

A main criterion for successful design was directional lamellae formation in whole volume of ice-templated samples, thus it was necessary to ensure good heat transfer between the cooling plate and the ceramic suspension. To fulfill this need, all types of ice-templating vessels contain a copper block in the bottom part. The final design of ice-templating vessels was optimized by experiments and two main types of ice-templating vessels were created:

Vessels for manufacturing of Al_2O_3 wafers

The shape and the size of final hybrid alumina/polymer composites were chosen. Due to the ballistic testing requirements for the sample size a rectangular shape was chosen to create a wafer with dimensions of 60.0 × 55.0 mm and thickness of 10.0 mm after sintering. According to these dimensions the ice-templating vessels were designed and manufactured, see Figure 25. The final vessel is composed of 5 parts to allow easy and fast dismember after the freezing step to prevent accidental melt-down of frozen samples. The inner dimensions of the vessel are 80.0 × 70.0 × 13 mm.

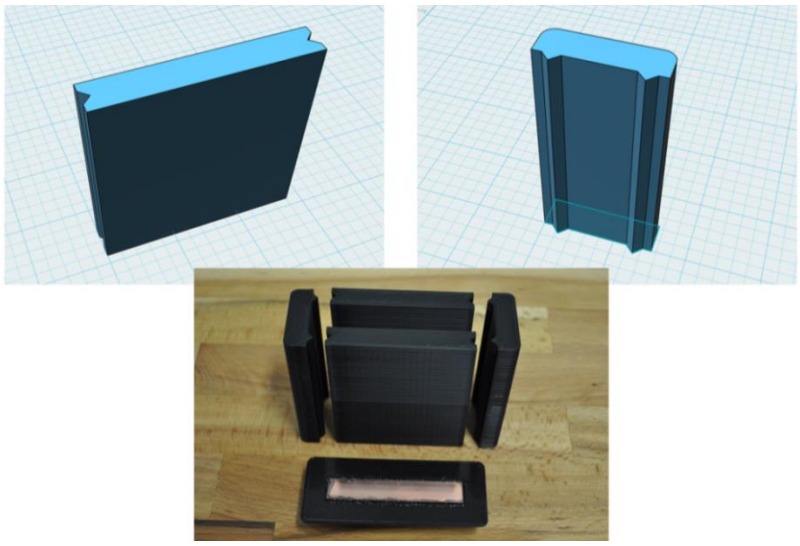

Figure 25. *Ice-templating vessels for flat scaffolds.*

Vessels for manufacturing of HAP scaffolds

The shape and the size of final hybrid HAP scaffolds were chosen to simulate the shape of bone grafts used for bone replacements. Cylindrical shape was chosen and inner diameter of the vessel was set to *d* = 25.4 mm and the height to *h* = 45.5 mm. According to these dimensions the ice-templating vessels were designed and manufactured, see Figure 26. The final vessel is composed of 4 parts to allow easy and fast dismember after the freezing step to prevent accidental melt-down of frozen samples.

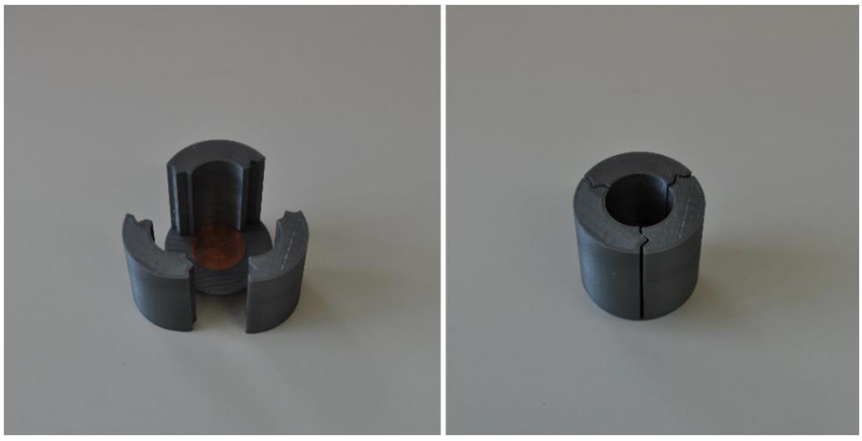

Figure 26. *Ice-templating vessels for cylindrical scaffolds.*

4.2.3 Indirect 3D printing + ice-templating

The proposed fabrication process of green HAP scaffolds samples with controlled multiscale porosity, which consists of a mesh 3D printing, ice-templating and freeze-drying stages, is schematically illustrated in Figure 27. Firstly, a 3D mesh consisting of orthogonal layers of parallel cylindrical bars (diameter, *d* = 0.9 mm), with 3 mm offset between the bars in *xy* plane, distance between adjacent layers in z direction of *h* = 0.66 mm, and total dimensions of 20.0 × 20.0 × 40.0 mm was designed in 3D CAD software and subsequently printed on a FDM 3D printer (Felix 3.1, FELIX printers, Netherlands). Polylactic acid (PLA) (Silver PLA, Plasty Mladeč) was used as a printing

material. Total volume of the 3D mesh was evaluated to be around 4 ml. Printed 3D mesh was trimmed off, placed on the bottom of an ice-templating vessel/die, and cast by the ice-templating HAP suspension. After the final step (freeze-drying process), green body of cylindrical HAP scaffolds, with controlled lamellar structure and embedded PLA mesh were obtained.

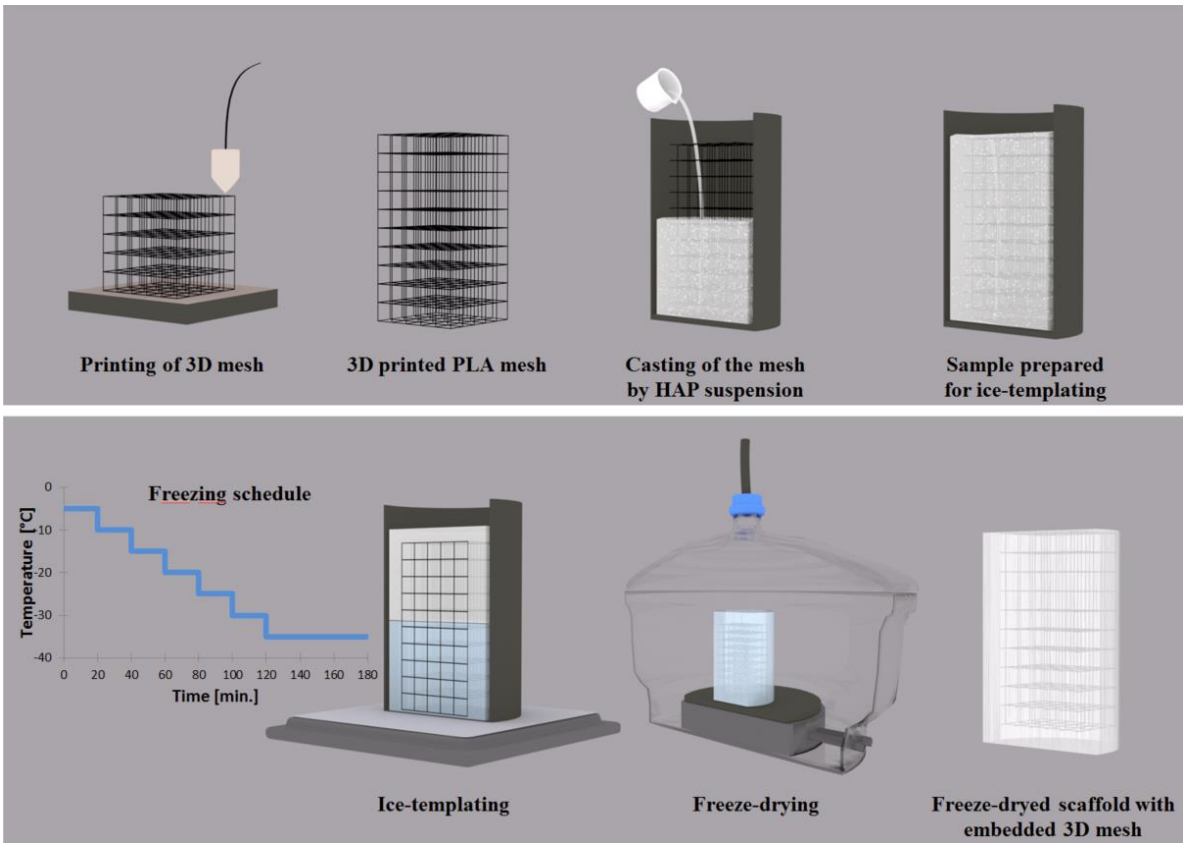

Figure 27. *Schematic illustration of the indirect 3D printing + ice-templating process.*

4.2.4 Ice-templating and freeze-drying process

The optimal initial temperature of the cooling plate, for all ice-templating vessels design, was set up at -5 °C. This starting temperature was used during all ice-templating experiments. The cooling rate (for this stage of experiments) was chosen so that the temperature of the cooling plate was decreased by 5 °C every 20 minutes down to -35 °C, see Figure 27. This cooling rate enables lamellae formation in the whole volume of all samples for all suspensions with various solid loadings. Samples were kept at -35 °C for 1 hour to ensure complete freezing and to balance the temperature throughout the samples.

The freezing step was followed by sublimation of ice crystals in a vacuum chamber at a pressure of approximately 10 Pa for 24 hours with a gradual temperature increase up to 30 °C, this procedure avoids damage of the lamellar structure of ceramic bodies by ice melting or reaching the sugar glass transition temperature. Therefore, it was necessary to moderate the heat transfer during the freeze-drying period. The implementation of freeze-drying in the whole process is shown in Figure 27.

4.2.5 Robocasting

Robocast scaffolds with similar macropore size were manufactured to compare porosity distribution, phase composition and mechanical stability with scaffolds prepared by indirect 3D printing combined with ice-templating. Among other additive manufacturing techniques, robocasting was selected for its similarities with the ice-templating, since it also uses water-based suspensions (with minimal additives content) as feedstock material, although in robocasting the slurries are highly concentrated in order to be capable of maintaining their shape during scaffold layerwise assembly.

Water-based suspension (ink) for robocasting was prepared from calcined HAP with a solid loading of 45 vol.%. The calcined powder was gradually added to an aqueous solution of a dispersant (DarvanC). Then, a 5 wt.% hydroxypropyl methylcellulose (MC) (Methocel F4M; Dow Chemical, USA) water solution was added to the mixture to increase its viscosity. In the last step the ink was flocculated through the addition of polyethylenimine (PEI) water solution (10 wt.%). After each addition of powder or component, the dispersion was homogenized in planetary centrifugal mixing device (ARE-250, Thinky, Japan) for 7 min at 700 revolutions per minute. The final composition of robocasting ink with 45 vol.% of HAP is shown in Table 5.

Table 5. *Composition of an ink with 45 vol.% of HAP used for robocasting.*

	HAP powder	**Water**	**Dispersant**	**MC (5 wt.%)**	**PEI (10 wt.%)**
Weight [g]	53.30	16.10	6.36	2.90	4.70

The homogenized robocasting ink was filled in a syringe barrel, and after removing any trapped air bubbles, mounted on the robocasting device (A3200, Aerotech/3D inks, USA). The part 3D model was designed in a suitable 3D CAD software (RoboCAD 4.1, 3D inks, USA), and consisted of a mesh of orthogonal layers containing parallel cylindrical adjacent bars (d = 0.84 mm). In order to mimic as closely as possible the interconnected pore channel network that would be obtained in the previous procedure upon elimination of the PLA mesh, one bar out of every three was eliminated from the model, leaving a gap roughly equal to d, and the separation between adjacent layers was set to h = 0.66 mm. The computer-controlled robotic system was used to fabricate the green body of three-dimensional porous scaffolds at room temperature by ink extrusion through a conical polymeric deposition nozzle (EFD, USA) with a tip diameter d = 0.84 mm. The nozzle was moved at a printing speed of 20 mm/s following the designed CAD model. Deposition was made in a paraffin oil tank to avoid rapid water evaporation from the ink during printing. The external dimensions of the resulting robocast scaffolds before sintering were 11.4 × 11.4 × 12.0 mm.

4.3 Sintering

Heat treatment (burning out of organic compounds) of ice-templated alumina wafers was carried out at 700 °C for 1 hour in air atmosphere with heating and cooling rates of 5 °C·min^{-1} to achieve complete burn out of organic compounds and separators used during ice-templating. Sintering of was performed at 1550 °C for 2 hours in an air atmosphere. The heating rate was set to 5 °C·min^{-1} and cooling rate from the sintering temperature was set to 10 °C·min^{-1} to avoid thermal shock and cracking.

Sintering of ice-templated HAP samples was performed at 1200 °C for 2h in air atmosphere. The heating rate was set to 2 °C·min^{-1} up to 600 °C (30 minutes dwell time), to allow all the additives and separators used during ice-templating and the 3D-printed PLA mesh to be burnt out completely, and 5 °C·min^{-1} from 600 °C up to sintering temperature. The cooling rate from the sintering temperature was set to 5 °C·min^{-1} to avoid thermal shock and cracking.

Sintering of robocast samples was performed under the same conditions as in the case of ice-templated samples, but some samples were sintered at 950 °C, rather than at 1200 °C, for 2h in an attempt to achieve a similar total porosity in samples fabricated by both methods.

4.4 Hybrid ceramic composites manufacturing

4.4.1 Ceramics/ceramics composites

Alumina/alumina composites

Ice-templated green Al_2O_3 scaffolds made from suspension with 30 vol.% solid loading were used as a starting substrate for dense alumina/porous alumina composites preparation. A slip casting technique was involved for dense ceramic layer formation. The Sumitomo AES-11C α-Al_2O_3 powder was used for preparation of water based slip casting suspensions with 50 vol.% solid loading was used.

Two types of dense alumina/porous alumina composites were prepared with monolithic or segmented dense layer, respectively. A 70.0 × 80.0 mm frame made of PLA on a FDM 3D printer was placed on ice-templated green Al_2O_3 scaffold and alumina suspension in desired thickness was cast in this frame. A 3D printed PLA insert was placed in the frame before slip casting, in the case of segmented dense layer manufacturing, see Figure 28. The surface of slip cast suspension was covered by a thin layer of sunflower oil, to slow down water evaporation. All samples in this setup were left to dry slowly at ambient conditions. After complete drying of the slip cast layer, the PLA frame was removed and formed composites were trimmed off, heat treated and sintered according to process specified above.

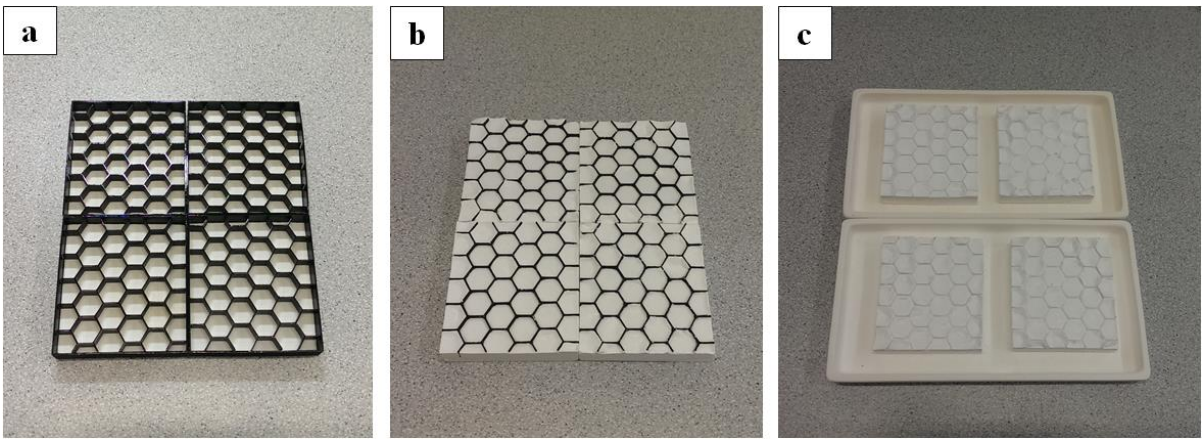

Figure 28. *The dense Al_2O_3/porous Al_2O_3 composites manufacturing; a) 3D printed PLA frame and insert, composites after slip casting of dense layer, c) composites after burn up of 3D printed parts.*

HAP/HAP composites

Ice-templated green HAP scaffolds made from calcined HAP suspension, with 15 vol.% solid loading, were used as a starting substrate for porous ceramic/dense ceramic composites preparation. A slip casting technique was involved for the dense ceramic layer preparation. HAP powder was used for preparation of water based slip casting suspension, which composition is specified in Table 6.

Table 6. *Composition of suspension with 20 vol.% of HAP used for slip casting.*

	HAP powder	Water	PVA	Dispersant	Octanol	Sugar
Weight [g]	42.00	51.50	1.10	2.00	0.80	4.00

Ice-templated green HAP scaffolds were placed in a silicon mold, cast by different ceramic suspensions and the surface of slip cast suspension was covered by a thin layer of sunflower oil, to slow down water evaporation. All samples in this setup were left to dry slowly at ambient conditions. After complete drying of the slip cast layer, the created composites were taken out of the silicon mold, trimmed off and sintered according to process specified above.

4.4.2 Ceramics/polymer composites

A basic criterion for successful preparation of hybrid ceramic composites is complete filling of empty space in the ceramic scaffolds. Therefore, viscosity of polymer is a crucial factor for preparation of bubble free ceramics/polymer composite. Four types of resins were used for hybrid Al_2O_3/resin composites fabrication, see Table 7. One resin was based on two component epoxide system (Axson technologies, USA), the other three resins were based two component polyurethane systems (Ebalta, Germany).

Table 7. *Selected properties of resins used for vacuum infiltration of ice-templated Al_2O_3 wafers.*

Resin type	Designation	Testing standard	Viscosity (25 °C) [mPa·s]	Tensile strength [MPa]	Elongation at break [%]
epoxy	EPOLAM 2017	EN ISO 527	210	73.0	6
polyurethane	GM 708/PUR 4	EN ISO 527	500 ± 100	50.0 ± 5.0	10 ± 3
polyurethane	GM 959/959-1	EN ISO 527	1350 ± 200	8.4 ± 0.8	900 ± 100
polyurethane	GM 984-1/A+B	EN ISO 527	2700 ± 200	39.0 ± 2.0	311 ± 8

Sintered alumina wafers with lamellar structure were placed in a silicone mold and embedded in polymer resin. The whole assembly was placed into a vacuum chamber, evacuated to pressure bellow 100 Pa and kept at this pressure for 20 min to ensure penetration of the resin into all free spaces of ceramic wafers. After the evacuation step, infiltrated ceramic wafers were left at room temperature for 24h to let the resin harden completely. The resulting hybrid Al_2O_3/resin composites were then removed from the mold and trimmed off. The final appearance of alumina/epoxy composites and a schematic illustration of processing steps during the preparation of the hybrid Al_2O_3/resin composites are shown in Figure 29.

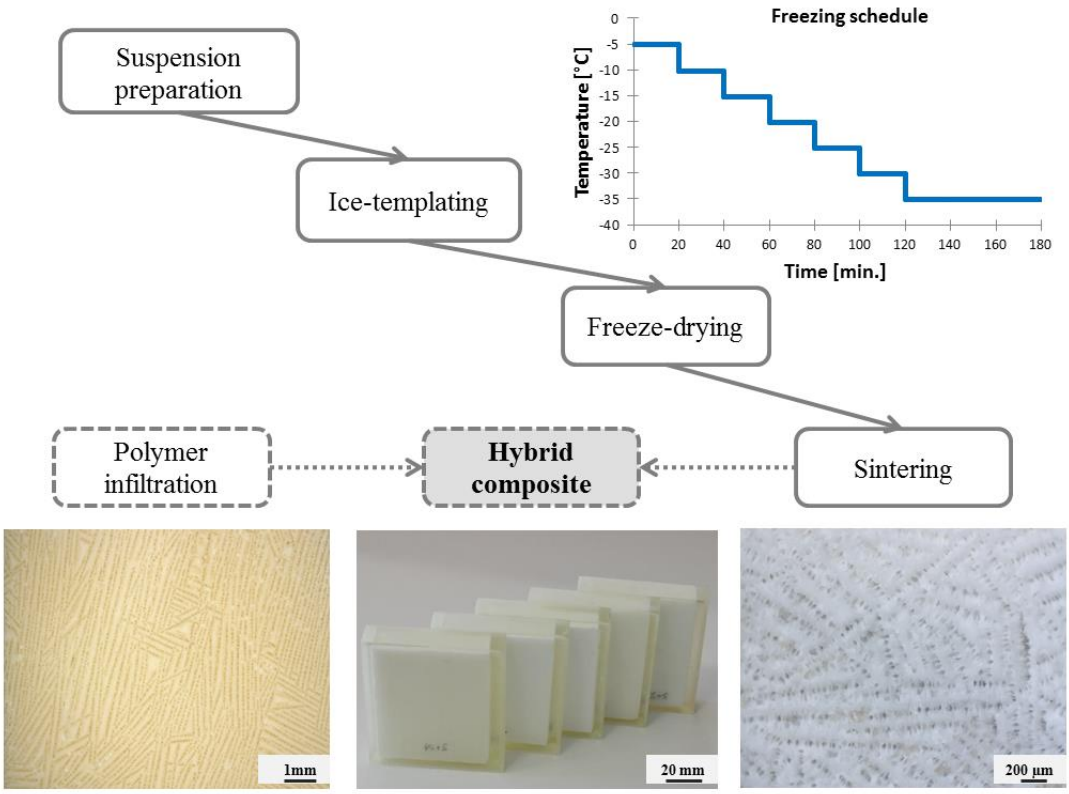

Figure 29. *Schematic illustration of processing steps during a preparation of the hybrid alumina/polymer composites.*

An epoxy resin was used for infiltration of alumina wafers for evaluation of flexural strength and fracture toughness behaviour of hybrid ceramics/polymer composites. Samples after epoxy infiltration were marked 25S, 30S, 35S, 40S and 45S according to the solid loading of alumina in starting suspensions (25S corresponds 25 vol.% of alumina in suspension, etc.).

4.5 Characterization

4.5.1 Scanning electron microscopy

The microstructure of sintered samples was analyzed using a scanning electron microscope FIB/SEM Tescan Lyra3 XMH (Tescan, Czech Republic) with digital image capturing system. Secondary electron images were used to reveal topographical information while backscatter electron images were used to show compositional contrast. Images were taken from both, surface of fractured samples at low voltage to reveal micro structural characteristics and grain sizes, and from polished surfaces of ice-templated samples cross sections in various axes to determine the lamellar thickness and spacing.

4.5.2 Image analysis

Image analyses using AxioVision software (Zeiss, Germany) were conducted on sintered ice-templated samples micrographs obtained by stereomicroscope Zeiss Stemi 508 (Zeiss, Germany) for evaluation of interlamellar distance.

4.5.3 X-ray diffraction

Phase compositions were investigated using a Rigaku X-ray diffractometer (XRD) (Rigaku, Japan). The XRD was operated at a voltage of 40 kV and current of 30 mA, source of X-rays was Cu anode (Cu Kα radiation). Results were compared with known data for identification of constituents and present phases. All XRD spectra were taken from crushed powder of the sintered scaffolds.

4.5.4 Porosity measurements

Total relative density of samples was evaluated from measurements of dimensions and weight of the sintered samples. The total relative porosity was then calculated based on the theoretical density of used materials. The size distribution of the open pores was measured by a mercury porosimeter PoreMaster (Quantachrome, USA) on sintered samples previously dried under a vacuum. The open pore distribution was used for inner structure comparison between various samples.

4.5.5 *Dilatometric analyses*

Cylindrically shaped samples with the diameter of d = 6 mm were prepared from both, calcined HAP powder and powder obtained by crushing of ice-templated scaffolds, by uniaxial pressing, using a semi-automatic hydraulic press BSML 21 (BRIO, Czech Republic). The applied pressure was set to 35 MPa with a 120 s dwell. To obtain a dilatometric data, the samples were then sintered in a high-temperature dilatometer (L70/1700, Linseis, Germany) at 1200 °C/2 h. The heating and cooling rate was set to 10 °C·min^{-1}. The relative shrinkage curves were converted to densification curves by methodology described in the literature [75]. After the sintering, relative densities of the samples were measured using the Archimedes method in accordance with the EN623-2.

4.5.6 Compressive strength

Rectangular testing samples with nominal dimensions of 10.5 × 10.5 × 10.5 mm were extracted from sintered ice-templated scaffolds using a precision saw Accutom-50 (Struers, USA). Robocast scaffolds were trimmed off and grinded so that the final dimensions before testing were 11.2 × 11.2 × 11.8 mm in the case of samples sintered at 950 °C/2h, and 8.8 × 8.8 × 8.2 mm in the case of samples sintered 1200 °C/2h.

Uniaxial compression tests of both sintered ice-templated and robocast samples, were performed using precision universal test frame AG-IS 10KN (Shimadzu, Japan) at a constant crosshead speed of 0.6 mm·min^{-1}. The compressive strength of each scaffold was evaluated as the maximum stress applied during the test. For both types of scaffolds at least 10 sintered samples were tested in order to get statistically reliable results.

4.5.7 Flexural strength and fracture toughness

The rectangular testing bars with nominal dimensions of 4.0 × 6.0 × 65.0 mm were extracted from each Al_2O_3/epoxy composite according to the scheme in Figure 30, using a precise saw Isomet 5000 (Buehler, USA). Sample surfaces were ground and polished using standard ceramographic approaches down to 1 μm diamond particle size. The flexural strength specimens were chamfered on the tensile side. The orientation of testing bars was chosen individually for given test type to always

keep the same loading direction (crack propagation) as would appear when the whole plate is loaded parallel to the Z-axis (i.e. out of plane orientation).

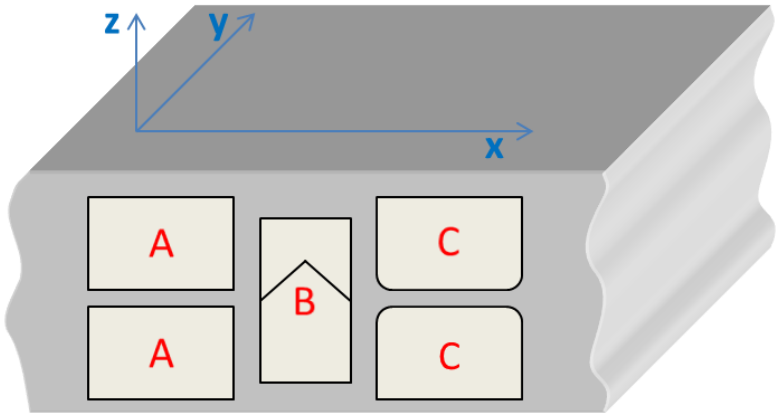

Figure 30. *A cutting scheme used for specimen preparation with indicated orientation. Specimens for elastic modulus are labelled by A, fracture toughness by B and flexural strength by C.*

The density of all composite hybrid composite materials was determined using an application of the Archimedes method on specimens type A. The double weighting technique was performed to determine volume, i.e. weighing in the air and HPLC water media using the density kit of precise balances (Denver, USA). The values obtained from individual bars were then statistically treated to receive relevant data for comparison.

Young's modulus was determined by using the same bars elastic properties and application of the impulse excitation technique using RFDA HT1600 system (IMCE, Belgium) equipment in accordance with the standard [76]. The bars were tested in the flexural mode in two orientations perpendicular to each other, i.e. out of plane (loading parallel to the z-axis) and in-plane (loading parallel to the x-axis) as is outlined in Figure 30. The Young's modulus values were calculated using RFDA software from measured natural frequencies, specimen dimensions, and densities. To obtain relevant data, at least 20 readings of natural frequencies per sample/orientation were conducted.

An Instron 8862 (Instron, UK) universal testing system with four and three point bend fixtures having a span of 40/20 and 24 mm was used for measurement of the flexural strength and fracture toughness, respectively. The cross-head speed of 0.5 $mm \cdot min^{-1}$ was applied in the case of flexural strength determination according to requirements given in the standard [77]. The samples for flexural strength measurement were oriented for out of plane loading as is indicated in Figure 30 (type C). The loading direction was chosen with respect to the planar shape of the prepared material and expected predominant loading during a service. The flexural strength values were calculated from the fracture (maximum) force and dimensions that were measured prior to the test. Minimally, 30 bending tests were conducted for each material. A Weibull statistical analysis was conducted and characteristic parameters, with confidence intervals on the confidence level of 95 %, were determined according to the standard [78].

The same experimental setup but with the three point bend configuration was used for the fracture toughness tests, and testing bars were oriented as is shown in Figure 30, specimen type B with keeping the same global crack propagation direction (i.e. out of plane orientation). A cross-head speed of 0.05 $mm \cdot min^{-1}$ was used to obtain valid loading curves exhibiting slow crack propagation with a smooth maximum. The chevron notch technique was used for fracture toughness determination. A chevron notch was introduced to each specimen with the top angle of 90° and a

nominal notch depth of 1.4 mm by two precious cuts of the thin diamond blade (thickness of 0.15 mm) using an Isomet 5000 saw (Buhler, USA). Fracture toughness was determined from the maximum force, geometrical parameters, and compliance function determined using Blum's slice model [79; 80; 81]. Each material was characterised by a minimum of 10 fracture toughness values, and the basic statistical parameters for a normal distribution were calculated.

4.5.8 Energy absorption evaluation

For energy absorption evaluation of the polymer resins, used in hybrid ceramics/polymer composites, the Newton cradle principle test (drop test) was used. Cylindrically shaped samples of diameter *d* = 50.0 mm and height *h* = 20.0 mm were cast from the resins (10 pieces of each type). The resin specimen was fixed to a steel rod of diameter *d* = 50 mm and length of 500 mm, and loaded with an impact rod raised to a specific height and then released. The impact velocity was set to 3.5 $m \cdot s^{-1}$, which is relatively low, but still this test enables to evaluate different behavior under dynamic loading, compared with the static compressive tests. Schematic illustration of the drop test is shown in Figure 31. More information about the drop test can be found elsewhere [82].

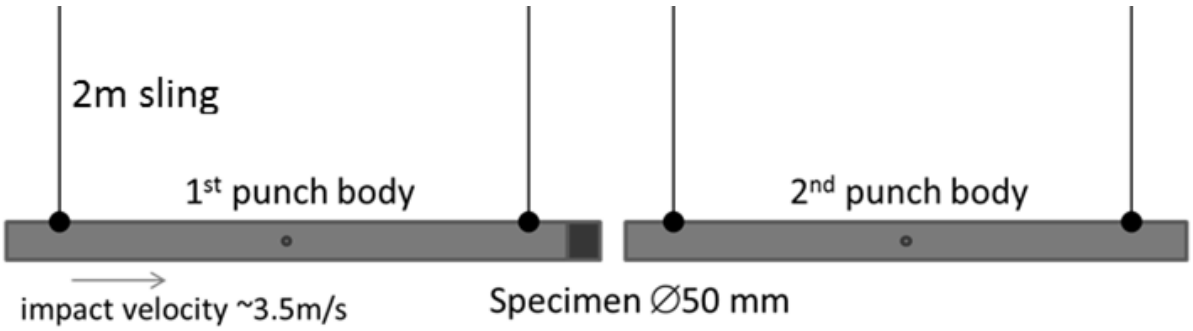

Figure 31. *Schematic illustration of the drop test.*

The maximum height at which the first rod raised after the impact and the speed that received immediately after the impact were recorded. The height was evaluated from the speed camera recorder and the speed was measured by the laser gauge. The energy absorbed by each specimen was evaluated by both residual potential and kinetic energy of the impact rod.

4.5.9 Ballistic performance

Hybrid alumina/resin composite plates were subjected to ballistic testing using the Depth of Penetration test (DOP). The DOP test was conducted as per the configuration depicted in Figure 32. More details about DOP test can be found in publications [83; 84; 85]. The armor piercing incendiary (API) projectile with quenched steel core (7.62 mm x 54R B32 API) was used in all ballistic testing experiments. The quenched steel core of the projectile has a diameter of 6.1 mm and a length of 28.2 mm with a mass of 10.4 g. The projectiles were fired through a rifled gun from a distance of 10 m. The projectile angle of impact was normal to the target. The velocity of projectiles was 854 ± 15 $m \cdot s^{-1}$.

The hybrid alumina/polymer tiles were glued on an aramid prepreg Twaron T 750/2-10 ContiTech (Teijin, Japan) using a Sikaflex 221 glue (Sika, Switzerland), and placed over an aluminium alloy (EN AW 2030) backing cylindrical block with diameter *d* = 90 mm and height h = 80 mm. This

assembly has been then fixed on a firing stand, for ballistic testing against 7.62 API projectiles. A schematic illustration of the DOP test setup is displayed in Figure 32.

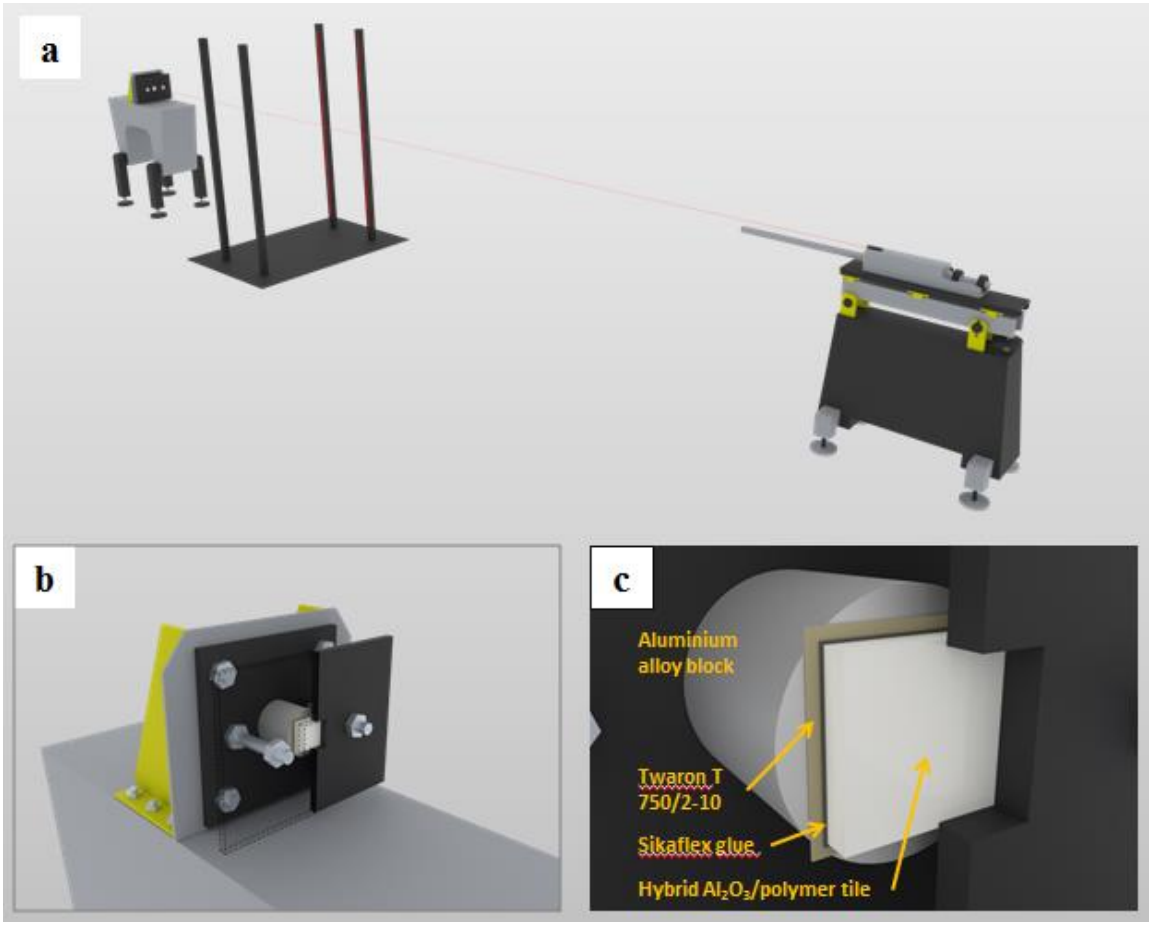

Figure 32. *The DOP ballistic test configuration; a) the overall shooting range setup, b) the firing stand for the sample mounting, c)close up of the sample set up for ballistic testing.*

Aluminium alloy backing blocks were examined by x-ray analysis after the ballistic testing to obtain precise value of the projectile penetration depth (DOP meas.). The DOP meas. values were then corrected according to a calibration curve, see Figure 33, to obtain a DOP values for 854 $m \cdot s^{-1}$ projectile impact velocity (DOP cor.).

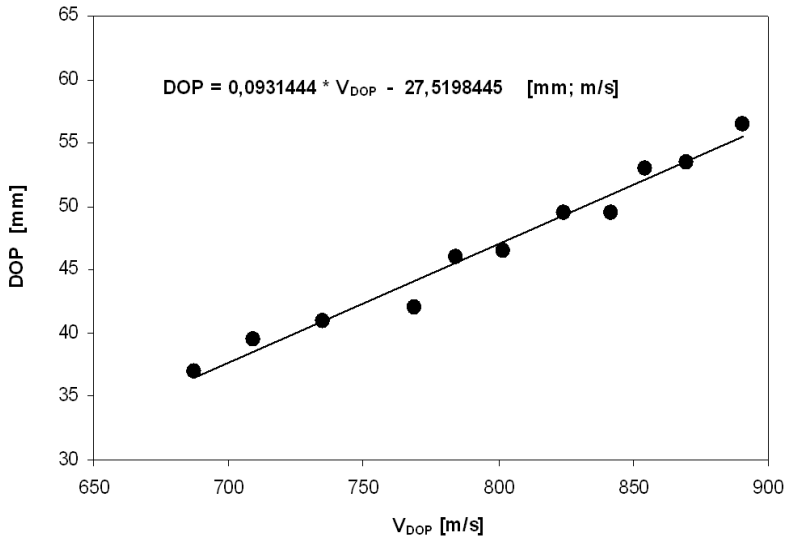

Figure 33. *DOP calibration curve for aluminium alloy EN AW 2030 and projectile 7.62 mm x 54R B32 API.*

5 Results

This chapter summarizes obtained experimental results and the description of the results follows the partial goals of the Ph.D. work.

5.1 Microstructure of ice-templated scaffolds

Microstructure of Al_2O_3 wafers

The appearance and shape of alumina wafers after ice-templating are shown in Figure 34. Dimensions of ice-templated alumina wafers before sintering were 70 × 80 × 15 mm.

Figure 34. *Al_2O_3 wafers after ice templating and freeze-drying.*

The microstructure of sintered alumina wafer (1550 °C/2 h in air atmosphere) on several levels of magnification is shown in Figure 35. The overall appearance of alumina lamellae, interlamellar spacing and interlamellar bridging caused by the sugar addition is depicted in the cross section perpendicular to lamellae growth (Figure 35a). The surface of lamellae and appearance of interconnecting bridges is shown in Figure 35b, note that this view is in direction parallel to the lamellae growth. The grain size and remaining intergranullar porosity is then shown in the Figure 35c.

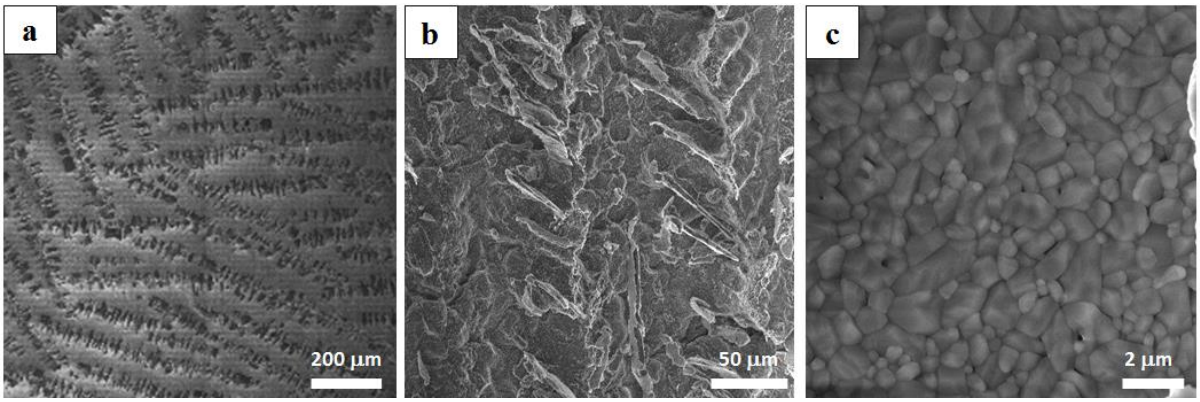

Figure 35. *Microstructure of sintered (1550 °C/2h) 45 vol.% alumina wafers; a) perpendicular to lamellae growth, b) interlamellar bridges, c) grains of sintered alumina.*

The influence of additives on lamellae surface micro roughness was also investigated by SEM. Comparison of surface topography of sintered alumina wafers made from suspension with 45 vol.% solid loading and addition of sugar, or addition of sugar and non-adding PVA is shown in Figure 36. Targeted microstructure should contain rough lamellae surface and high amount of interconnecting bridges.

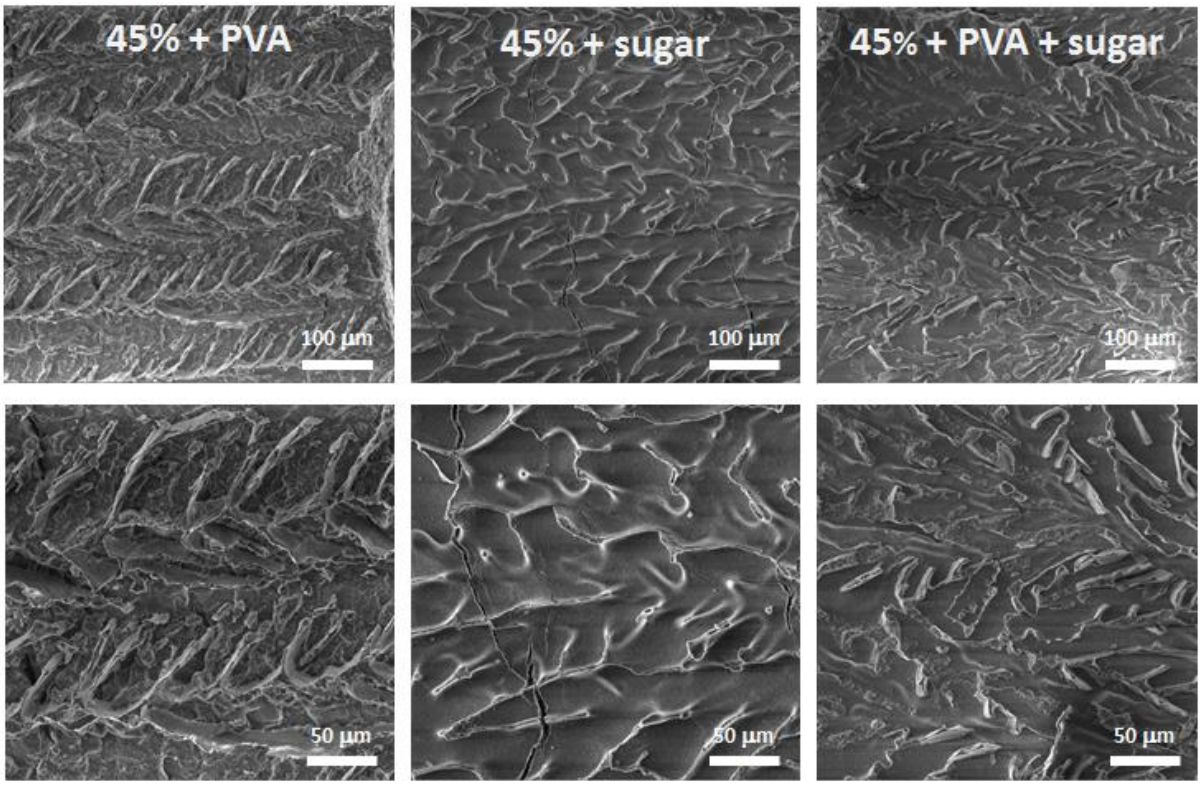

Figure 36. *Ice-templating additives Influence on micro roughness of alumina lamellae.*

Microstructure of HAP scaffolds

The appearance and shape of HAP cylindrical scaffolds after ice-templating is shown in Figure 37a. In Figure 37b is depicted composite scaffold with slip cast HAP layer after sintering at 1200 °C/2 h in air atmosphere. The slip cast layer is dense and the ice-templated structure remained porous.

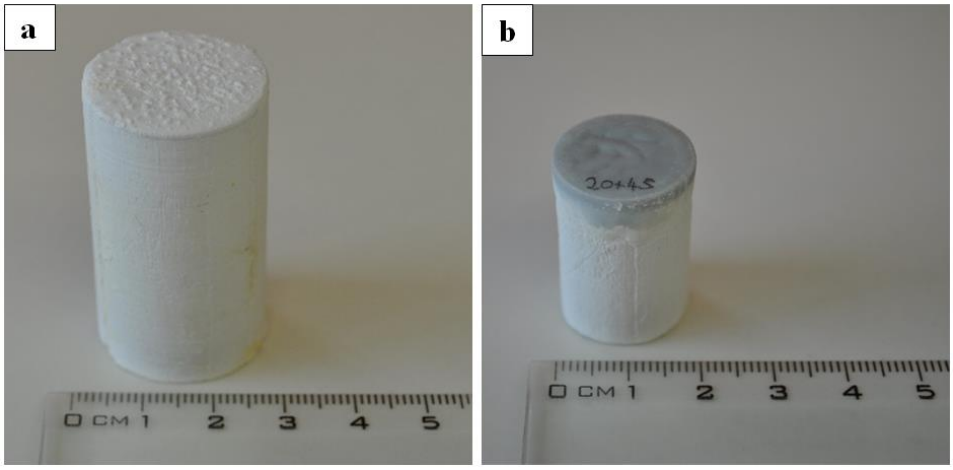

Figure 37. *HAP scaffolds after ice-templating (a), and after subsequent slip casting of HAP dense layer and sintering at 1200 °C/2h (b).*

The microstructure of sintered HAP scaffold (950 °C/2h in air atmosphere) on several levels of magnification is shown in Figure 38. The overall appearance of the HAP lamellae, interlamellar spacing and interlamellar bridging caused by the sugar addition is depicted in the cross section perpendicular to lamellae growth (Figure 38a). The surface of lamellae and appearance of interconnecting bridges is shown in Figure 38b, note that this view is in direction parallel to lamellae growth. The intergranullar porosity of lamellae wall is shown in Figure 38c.

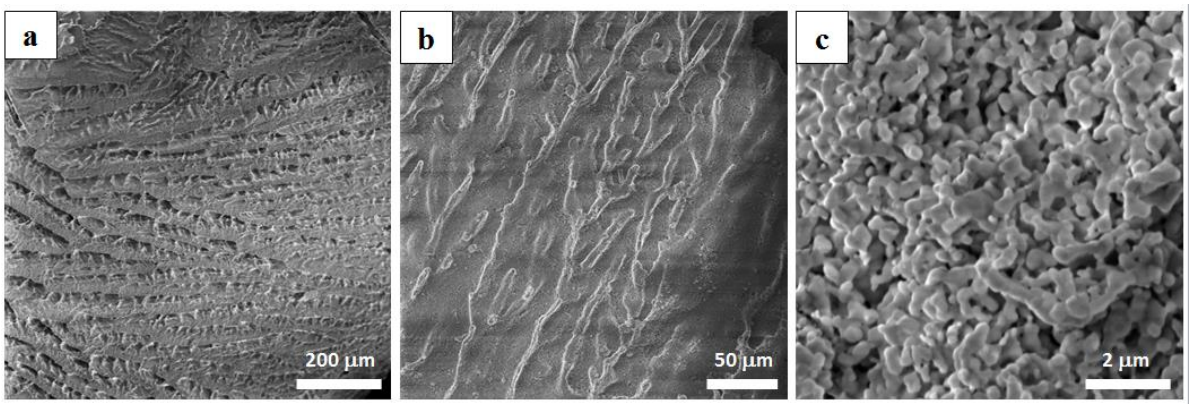

Figure 38. *Microstructure of sintered (950 °C/2h) 15 vol.% HAP scaffolds; a) perpendicular to lamellae growth, b) interlamellar bridges, c) partially sintered HAP particles.*

Microstructure of indirectly 3D printed + ice-templated and robocast HAP scaffolds

The appearance and shape of indirectly 3D printed + ice-templated HAP scaffold with subsequently slip cast dense HAP layer sintered at 1200 °C/2 h is shown in Figure 39a. A sample prepared for mechanical testing, which was cut out from indirectly 3D printed + ice-templated HAP scaffold sintered at 950 °C/2h is shown in Figure 39b. The influence of sintering temperature on densification and introduced macro porosity by robocasting is depicted in Figure 39c.

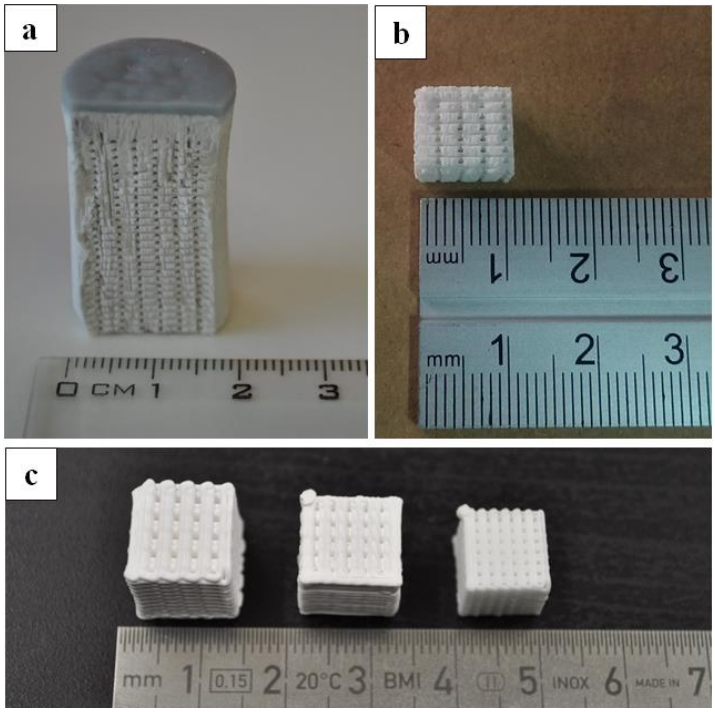

Figure 39. *Different appearance of HAP scaffolds; a) indirectly 3D printed + ice-templated scaffold with subsequently slip cast dense HAP layer, b) indirectly 3D printed + ice-templated sample for compression test, c) robocast scaffolds sintered at different temperatures, from the left: 950 °C/2h; 1000 °C/2h; 1200 °C/2h.*

SEM micrographs of the robocast scaffold sintered at 950 °C/2h and the indirectly 3D printed and ice-templated scaffold sintered at 1200 °C/2h are shown in Figure 40. These images show on one hand a comparable size of introduced macropores, and on other hand a difference in their shape. The higher magnification insets in Figure 40 show cross sectional images (perpendicular to the lamellae growth in case of the ice-templated sample, Figure 37b to reveal the difference in porosity between scaffolds in the tens of microns range.

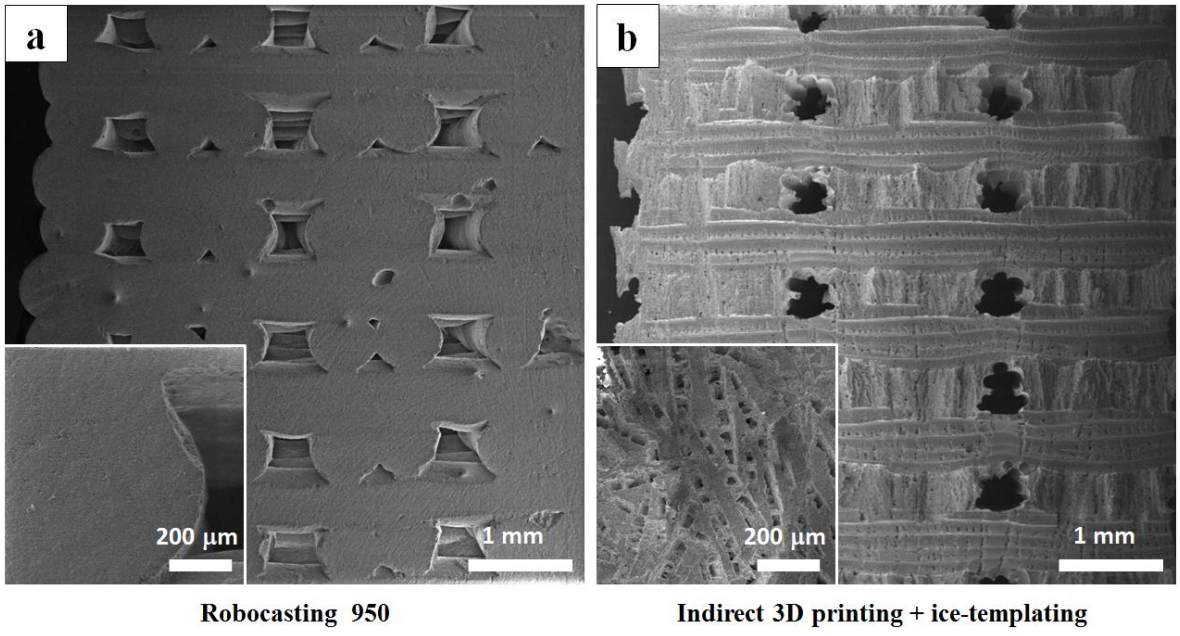

Figure 40. *SEM micrographs of (a) robocast scaffold sintered at 950 °C/2h and (b) indirectly 3D printed and ice-templated scaffold sintered at 1200 °C/2h.*

5.2 Porosity of ice-templated scaffolds after sintering

Porosity of Al_2O_3 wafers

Total relative porosity and interlamellar distance measurements were performed on ice-templated alumina wafers sintered at 1550 °C/2h, prepared from suspensions with Al_2O_3 solid loading from 25 to 45 vol.%. Results of measurements are shown in Table 8. The highest total porosity was achieved in the case of ice-templated wafers made from suspension with 25 vol.% Al_2O_3 solid loading (55.6 %) and the lowest porosity in the case of wafers made from suspension with 45 vol.% solid loading (35.1 %).

Table 8. *Porosity and interlamellar distance of ice-templated Al_2O_3 wafers sintered at 1550 °C/2h.*

Material	25S	30S	35S	40S	45S
Relative porosity [%]	55.6	49.3	44.9	40.6	35.1
Lamellae distance [μm]	130 ± 26	110 ± 19	95 ± 14	75 ± 10	60 ± 11

As expected, a good correlation can be found between total porosity results and interlamellar distance. The highest average interlamellar distance of 130 ± 26 μm was reached by ice-templated alumina wafers made from 25 vol.% of Al_2O_3 powder solid loading suspension and was gradually decreasing up to 60 ± 11 μm in the case of wafers made from suspension with 45 vol.% solid loading.

Porosity of HAP scaffolds

Total porosity and interlamellar distance measurements were performed on ice-templated HAP cylindrical scaffolds sintered at 950 °C/2h, prepared from suspensions with HAP powder solid loading from 7.5 to 20 vol.%. Results of those measurements are shown in Table 9. Very high amount of porosity was achieved at all scaffolds, but the highest total porosity was reached in the case of ice-templated scaffolds made from suspension with 7.5 vol.% of HAP powder solid loading (91.1 %). The lowest porosity was measured in the case of scaffolds made from suspension with 20 vol.% solid loading (79.8 %).

Table 9. *Porosity and interlamellar distance of ice-templated HAP scaffolds sintered at 950 °C/2h.*

Material	7.5S	10S	15S	20S
Relative porosity [%]	91.1	87.9	83.7	79.8
Lamellae distance [μm]	89 ± 18	87 ± 16	79 ± 15	74 ± 12

As in the case of alumina wafers, a good correlation can be found between total porosity results and interlamellar distance. The highest average interlamellar distance of 89 ± 18 μm was reached by ice-templated HAP scaffolds made from suspension with 7.5 vol.% of HAP powder solid loading. The interlamellar distance is gradually decreasing up to 74 ± 12 μm in the case of wafers made from suspension with 20 vol.% solid loading.

Porosity of indirectly 3D printed + ice-templated and robocast HAP scaffolds

Total relative porosity measurements were carried out on ice-templated scaffolds sintered at 1200 °C/2h and on robocast scaffolds sintered at 950 °C/2h and 1200 °C/2h. Highest total porosity was achieved by indirect 3D printing and ice-templating process (72.6 ± 1.21 %). Porosity was about 5 % lower (67.5 ± 0.76 %) in the case of robocast samples sintered at 950 °C and about 47 % lower (25.7 ± 2.40 %) in the case of robocast samples sintered at 1200 °C.

Mercury intrusion porosimetry measurements were carried out on indirectly 3D printed and ice-templated scaffolds sintered at 1200 °C/2h in air atmosphere and on robocast scaffolds sintered at 950 °C/2h and 1200 °C/2h in air atmosphere to compare the pore size distribution between all scaffolds. Figure 41 shows the porosimetry measurement results. It is apparent that the total volume of porosity can be divided into three main regions:

- porosity between grains (0.1–5 μm),
- interlamellar porosity (5–100 μm),
- introduced macroporosity (100–1000 μm).

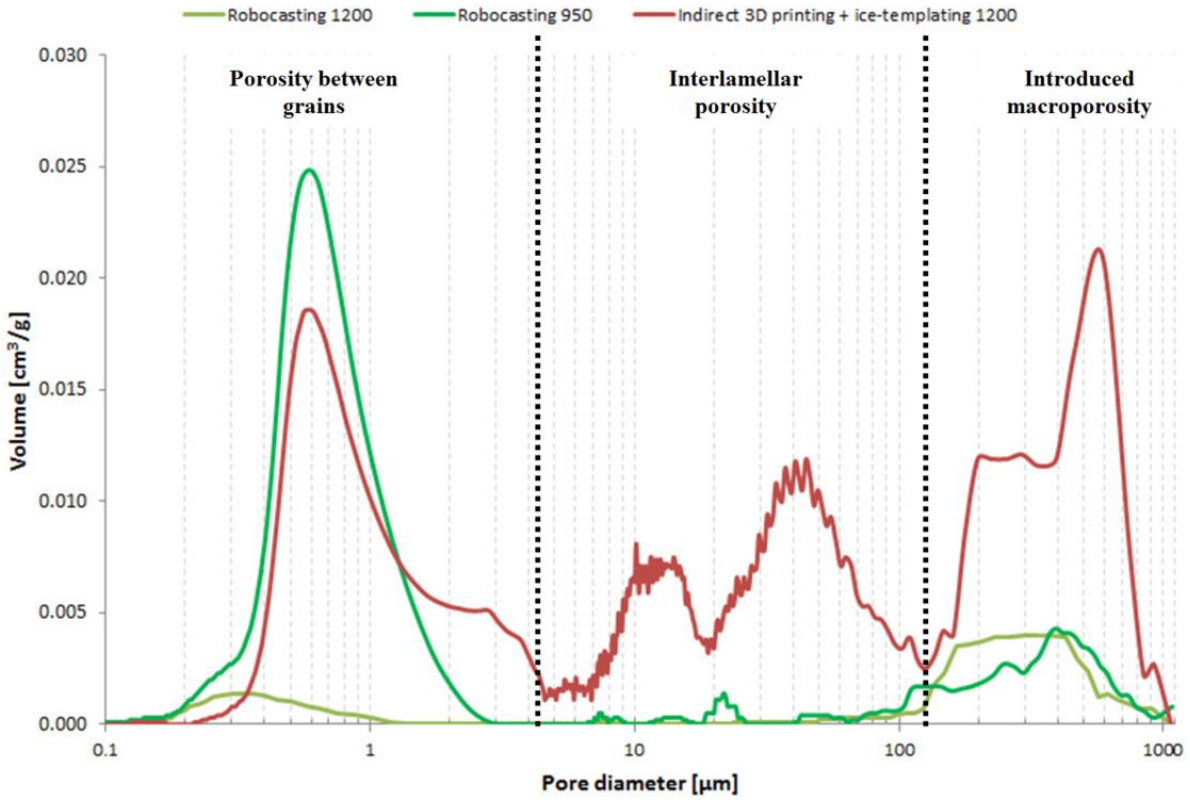

Figure 41. *A comparison of mercury intrusion porosimetry results for scaffolds prepared by robocasting and indirect 3D printing combined with ice-templating.*

The main difference between samples fabricated by both methods is the porosity in the 5–100 μm range, where the interlamellar porosity region was created by growing ice crystals during ice-templating process. This type of porosity is inexistent in the robocast samples, even in those sintered at 950 °C. Volume of introduced macropores appears to be lower also in the case of robocast

samples, but this discrepancy might be caused by inaccurate measurement of macropores with convex (Figure 40b), rather than typical concave, walls. Intergranular porosity is also much larger in ice-templated samples sintered at 1200 °C/2h, compared to robocast samples sintered at the same temperature, but close to that of robocast samples sintered at much lower temperature (950 °C/2h).

It is evident that the total relative porosity of robocast samples sintered at 1200 °C/2h is much lower, and that its main region lies in the region of pre-designed macroporosity. The less abundant and smaller intergranular pores proof a significantly greater densification in these samples.

5.3 Influence of ice-templating process on sintering behavior and phase composition of HAP scaffolds

To clarify the difference in the sintering behavior of robocast and indirectly 3D printed + ice-templated samples, dilatometric analyses were carried out on samples prepared from both, calcined HAP powder (800 °C/2h) and ice-templated scaffold. The obtained results are shown in Figure 42.

The dilatometric analyses revealed start of densification at temperature about 100 °C higher for ice-templated samples (~ 970 °C vs. 870 °C) and the absolute (apparent) density after sintering at the same temperature (1200 °C/2h) is about 34 % lower for ice-templated samples (~ 1.98 g·cm^{-3} vs. 2.99 g·cm^{-3}).

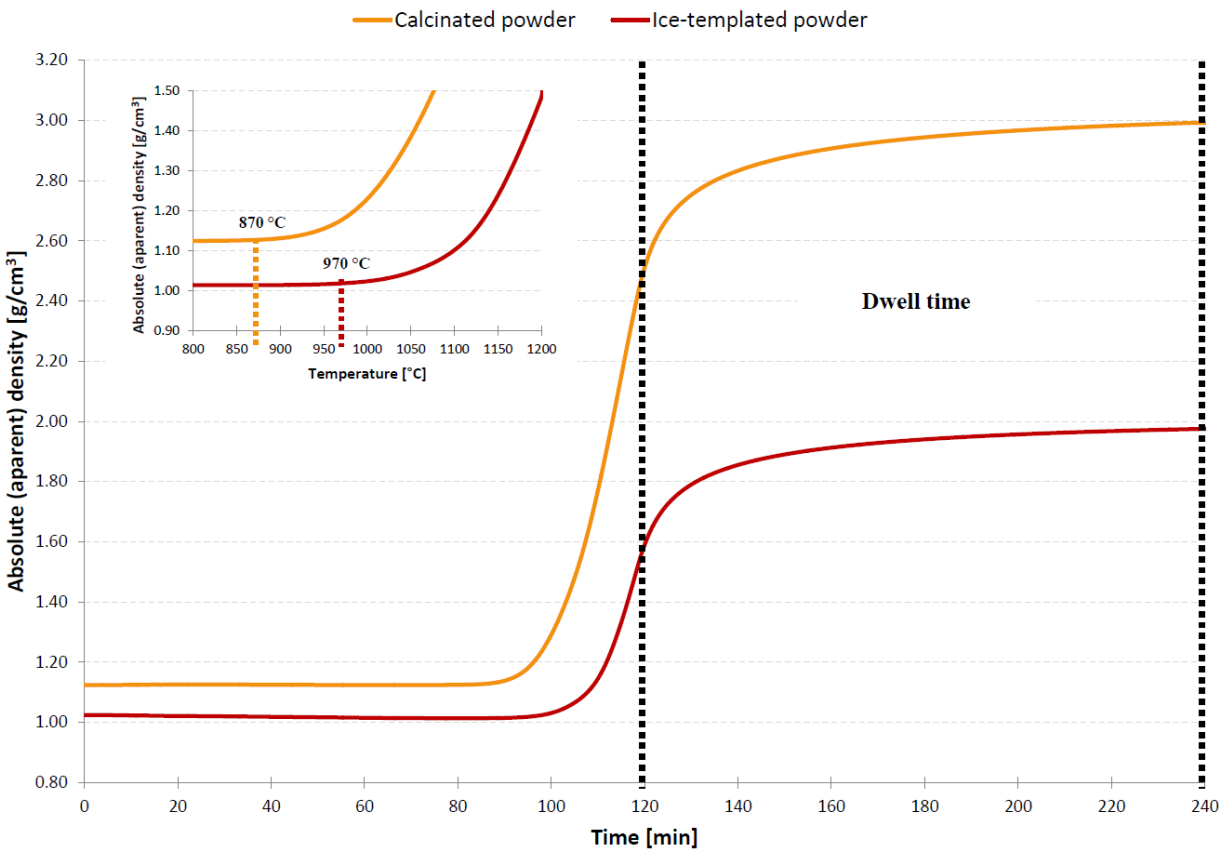

Figure 42. *Dilatometric analyses of samples prepared from the calcined HAP powder and the green body ice-templated scaffold. The initial density difference was caused by a particle packing during the ice-templating process, that wasn't overcome by a pressure involved in dilatometric samples preparation.*

XRD analyses were performed on calcined HAP powder (800 °C/2h), indirectly 3D printed and ice-templated scaffolds sintered at 1200 °C/2h, and robocast scaffolds sintered at 950 °C/2h to compare the phase composition of sintered samples with starting powder. The obtained XRD patterns are shown in Figure 43.

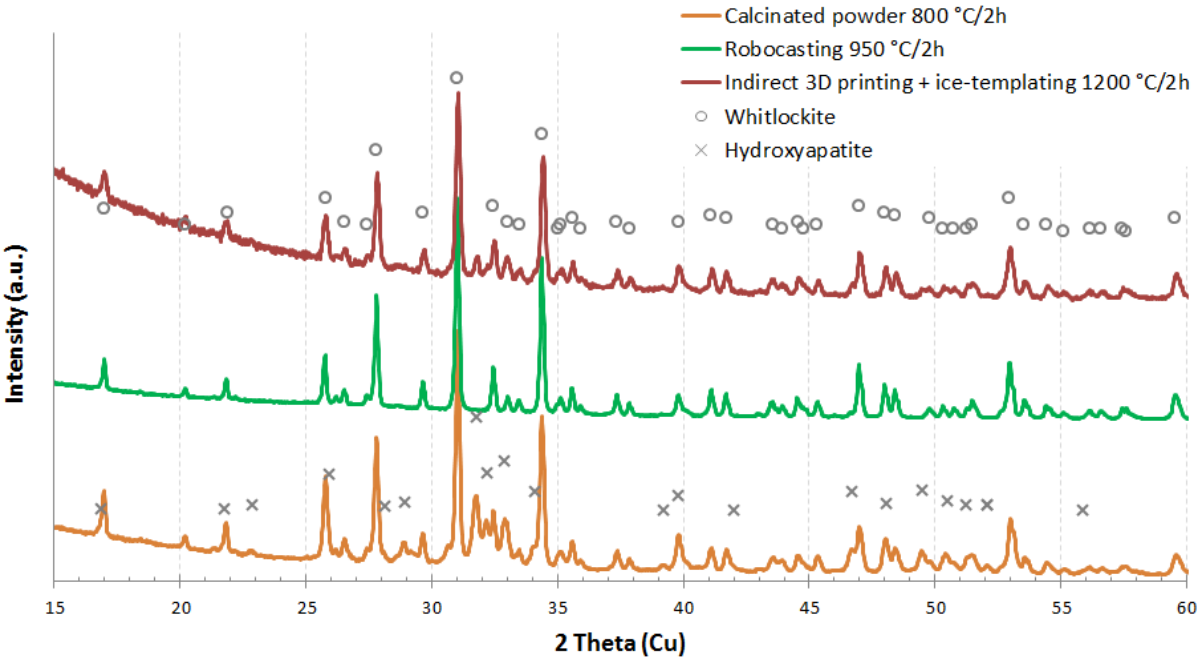

Figure 43. *The XRD patterns of calcined HAP powder, robocast scaffold and scaffold prepared by indirect 3D printing + ice-templating and robocasting. Main hydroxyapatite and Whitlockite peaks are identified with the symbols.*

The observed phase composition of calcined starting HAP powder is a mixture of hydroxyapatite and Whitlockite (β-TCP), as the primary phase after calcination. The phase composition of robocast samples sintered at 950 °C is almost pure β-TCP, while ice-templated samples sintered at 1200 °C still retains some of the original hydroxyapatite.

XRD analyses were also performed on ice-templated HAP scaffolds with slip cast HAP dense layer and subsequently sintered at 1200 °C/2h. The obtained XRD patterns, shown in Figure 44, revealed that the phase composition of ice-templated part is composing of β-TCP with some traces of original hydroxyapatite. However the phase composition of dense slip cast part contains γ-calcium pyrophosphate.

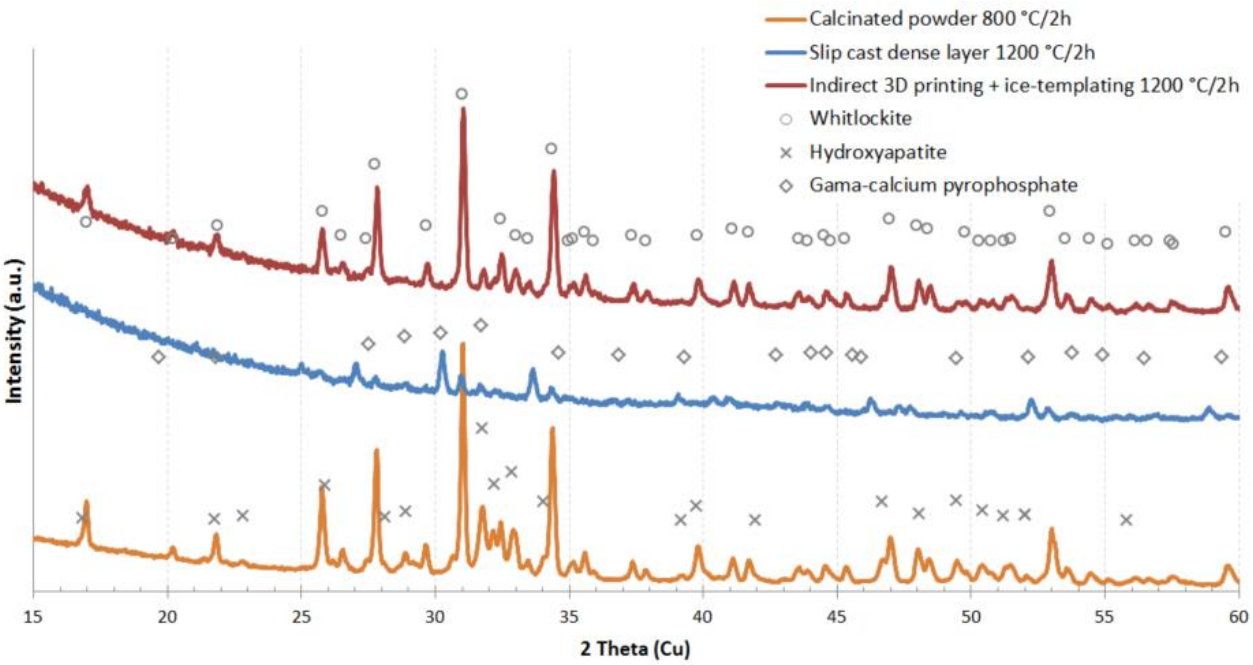

Figure 44. *The XRD patterns of ice-templated HAP scaffold with slip cast dense HAP layer sintered at 1200 °C/2h. Main hydroxyapatite, Whitlockite, and γ-calcium pyrophosphate peaks are identified with the symbols.*

5.4 Hybrid ceramic/polymer composites

Microstructure of alumina/polymer composites

Final appearance of hybrid ice-templated alumina/polymer composites after full curing of casting resins, taking out of silicon die and mechanical trimming is shown in Figure 45. These hybrid composites with final dimensions 72 x 72 x 16 mm are prepared for further operations and ballistic testing using DOP method.

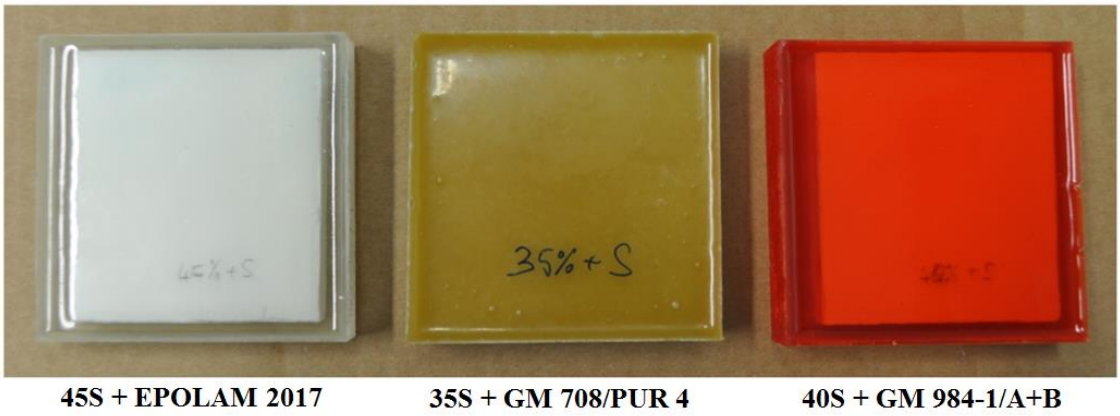

Figure 45.*Three different kinds of hybrid alumina/polymer composites.*

Figure 46 depicts microstructure comparison of alumina/polymer hybrid composites. Figures 46a and 46b are micrographs of hybrid composite Al_2O_3/GM 984-1/A+B obtained by stereomicroscope. The difference in alumina lamellae appearance, when viewed perpendicularly to lamella growth (Figure 46a) and in parallel to lamellae growth (Figure 46b), is shown in these micrographs. Notice well visible interlamellar bridges, caused by addition of sugar to initial ice-templating suspension, in Figure 46a.

SEM micrographs of hybrid composite Al_2O_3/EPOLAM 2017 shown in Figure 46c were obtained by back scattered electrons (BSE) hence the light areas are dedicated to alumina and the dark parts to epoxy resin. These micrographs are revealing difference in microstructure of hybrid composite with increasing alumina content in starting ice-templating suspensions (from 25 vol.% to 45 vol.%) and show recognizable lamellae formed by ice-templating and subsequently filled with epoxy resin. The shape and distances are changed with the increasing ceramic to polymer ratio. Distances of lamellae increase and shape of lamellae change from narrow long sharp closely packed chain of ribs to the wide short blunt partially separated ribs.

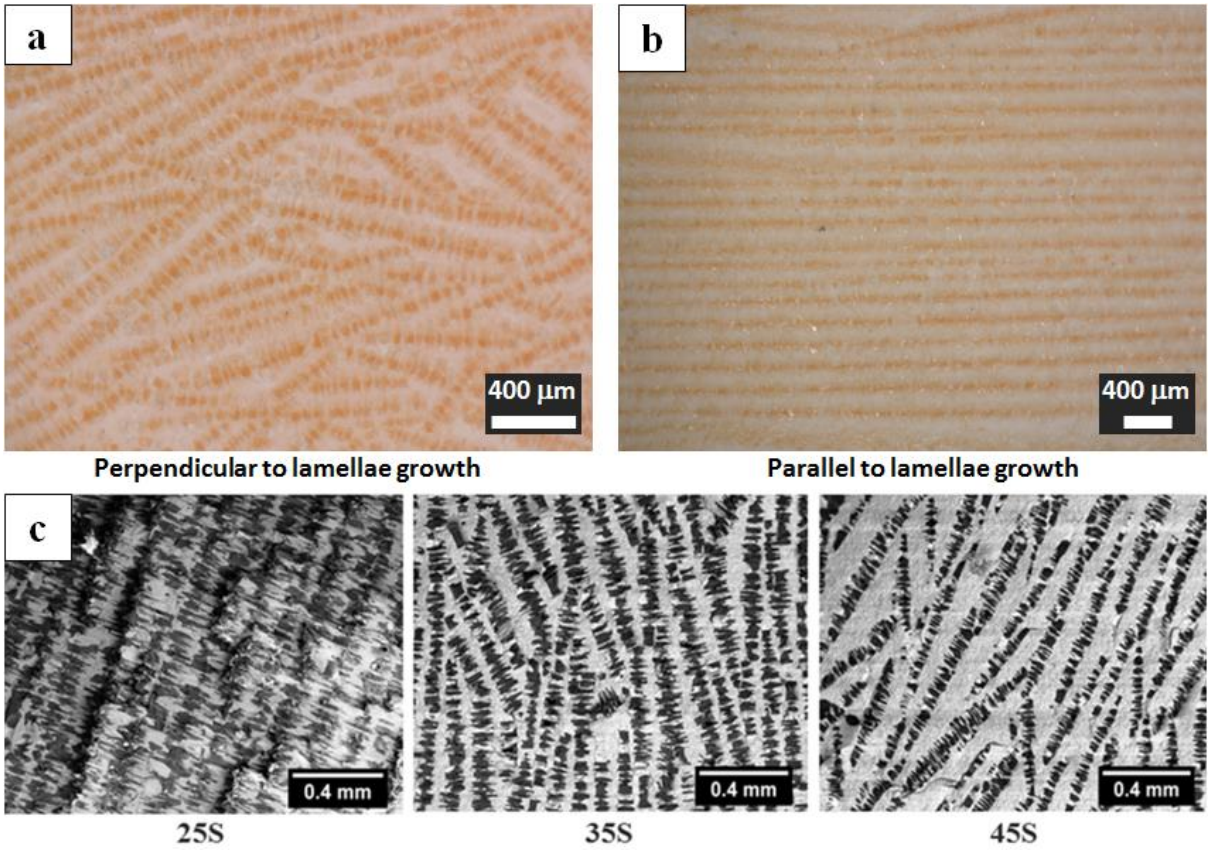

Figure 46. *The alumina/polymer hybrid composites microstructure; a) and b) Al_2O_3/GM 984-1 cross sections micrograph obtained by stereomicroscope, c) Al_2O_3/EPOLAM 2017 microstructure comparison with different alumina volume fraction, micrographs obtained by BSE.*

Ceramic/polymer composites for decorative purposes

The microstructure of hybrid ceramic/polymer composites, mainly in cross section perpendicular to lamellae growth (see Figure 46b), can imitate layered microstructure of Damascus steel. The contrast between layers is not created by use of low carbon and high carbon steel and their different behavior during etching as in the case of Damascus steel, but by the color contrast between alternating layers of sintered ceramics and infiltrated resin.

The final appearance of hybrid ceramic/polymer composite can be very similar to look of Damascus steel, especially when a zirconia powder is used in the starting suspension for preparation of ice-templated lamellar scaffold, and a black pigment is added into resin before infiltration. Microstructure of such hybrid composite with Damascus-steel-like pattern made of ice-templated zirconia infiltrated with black colored epoxy is shown in the Figure 47.

Figure 47. *The microstructure of ice-templated zirconia (15S)/black colored epoxy (EPOLAM 2017) composite.*

The lamellae of zirconia, created by ice-templating process, are after sintering at 1550 °C/2h in air atmosphere translucent, and therefore the black epoxy resin is optically a dominant component in the microstructure.

Main advantages of hybrid ice-templated ceramics/polymer composites against Damascus steel is their higher corrosion resistance, non-magnetic properties, high wear resistance (caused by presence of sintered ceramic lamellae within the structure), and low density (2.36 $g \cdot cm^{-3}$ in the case of alumina/epoxy composite prepared from ice-templating suspension with solid loading of 25 vol.%, see Table 10). These properties can make these hybrid composites attractive for manufacturing of design and jewelry products such as earrings, necklaces, pendants, rings, knives, cufflinks etc.

Simple earrings and cufflinks were made of ice-templated zirconia scaffold infiltrated with black colored epoxy resin (EPOLAM 2017) in order to verify the possibility of hybrid composites use for design products manufacturing. These two jewelry products are shown in the Figure 48.

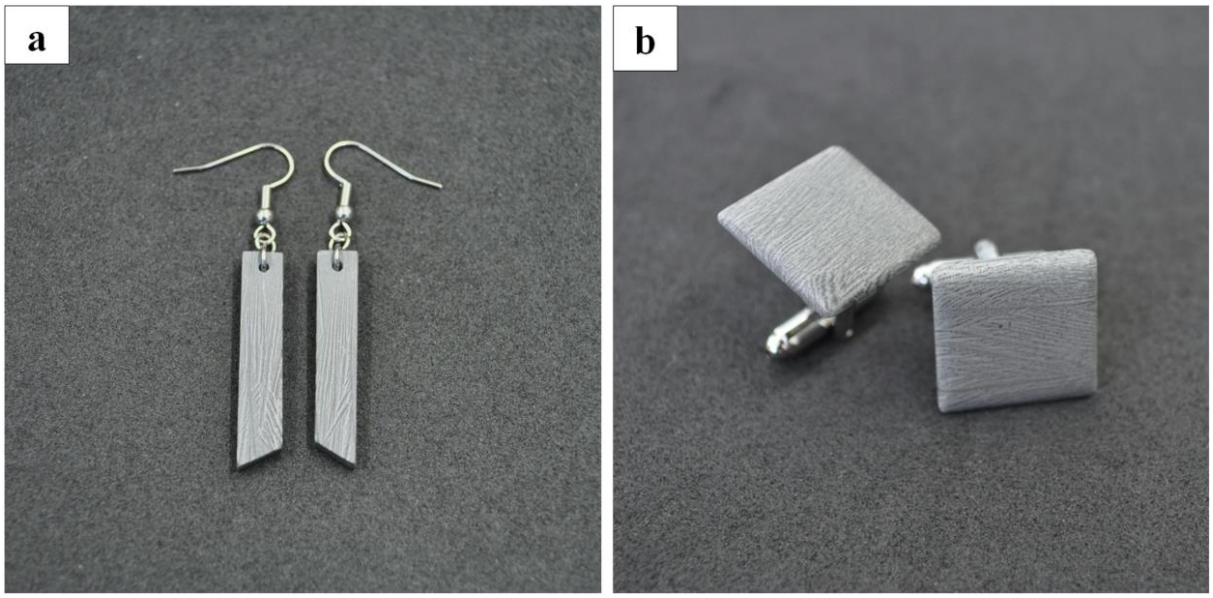

Figure 48. *Appearance of a) earrings, b) cufflinks made of ZrO_2/black epoxy resin hybrid composite.*

Microstructure of porous Al_2O_3/dense Al_2O_3/polymer composites

Figure 49 depicts the appearance of four ice-templated alumina/dense alumina composites prepared for polymer infiltration (Figure 49a), and final appearance of hybrid composites after vacuum infiltration by polyurethane casting resin (GM 984-1/A+B) prepared for ballistic testing (Figure 49b).

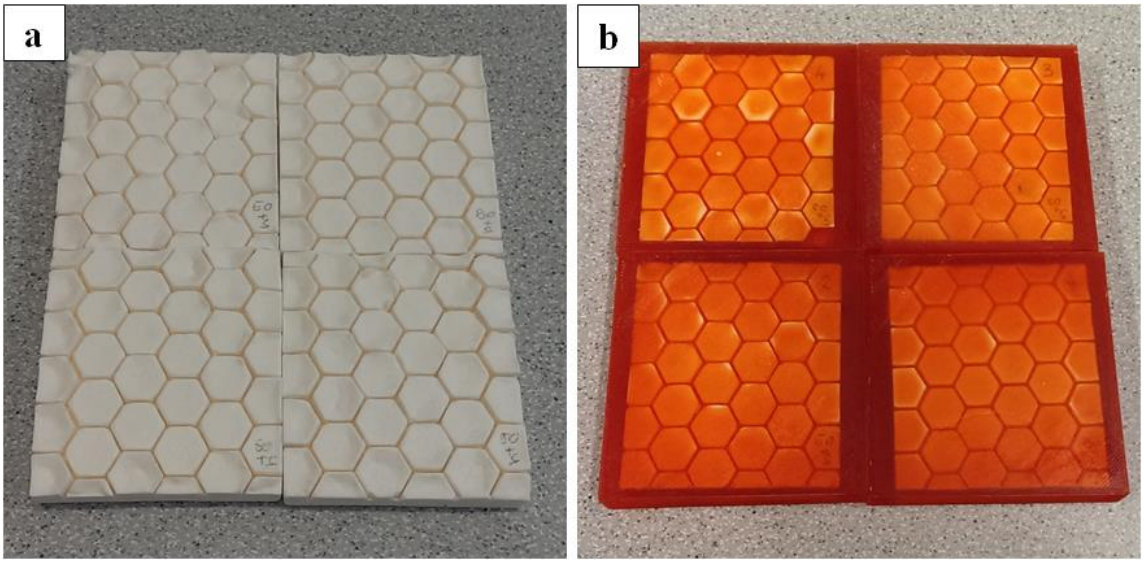

Figure 49. *Appearance of porous Al_2O_3/dense Al_2O_3/ polymer hybrid composites; a) after sintering at 1550 °C/2h, b) after infiltration.*

Closer view on microstructure of ice-templated alumina/dense alumina composites is shown in Figure 50. Higher magnification SEM images (Figure 50b and c) show that the ice-templated and slip cast part of composites is well connected without any major cracks and the boundary between these two parts is well pronounced and quite sharp, see Figure 50c.

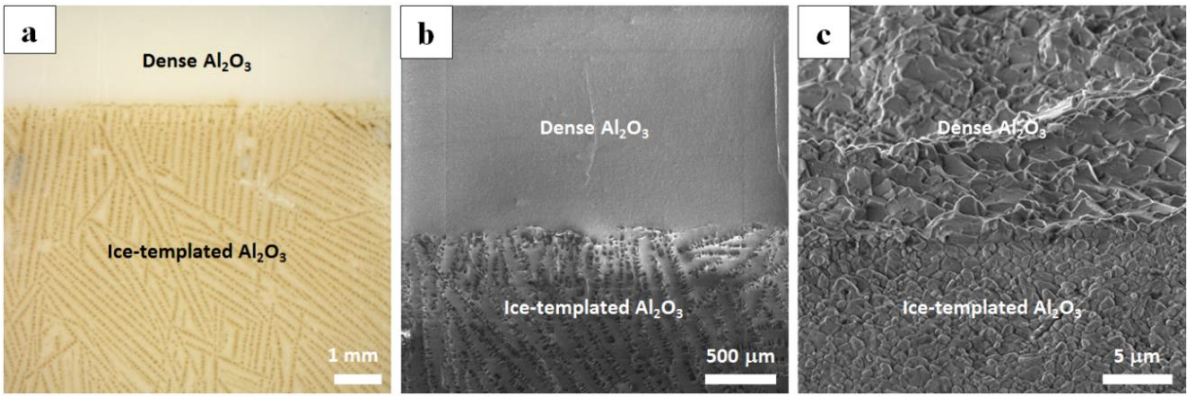

Figure 50. *Microstructure of porous Al_2O_3/dense Al_2O_3/ polymer hybrid composites; a)overall overview of microstructure in cross section perpendicular to lamellae growth, b) SEM micrograph of composite before polymer infiltration, c) detail view of ice-templated /dense alumina boundary.*

The explanation of such a good connection between ice-templated and slip cast part of composites can be found in the manufacturing process, where the ice-templated part acts as a suction die. Capillary forces, created by microstructure of ice-templated part, help to pack ceramic particles during slip casting of dense layer and to create a strong connection between both parts.

Energy absorption of polymer resins

For energy absorption evaluation of the polymer resins, applied in hybrid ceramics/polymer composites manufacturing, the Newton cradle principle test was used. Relative absorption of potential and kinetic energy for all polymer resins is shown in Figure 51.

The results of the Newton cradle test revealed that both energy absorption evaluation approaches (comparing of positional energies and kinetic energies) are nearly equivalent. The lowest energy absorption was achieved by epoxy casting resin (EPOLAM 2017), which was able to absorb only about 0.3 % of energy. On the other hand the polyurethane casting resin GM 959/959-1 was able to absorb about 22.5 % of input energy. Such energy absorption is superior to all other tested resins.

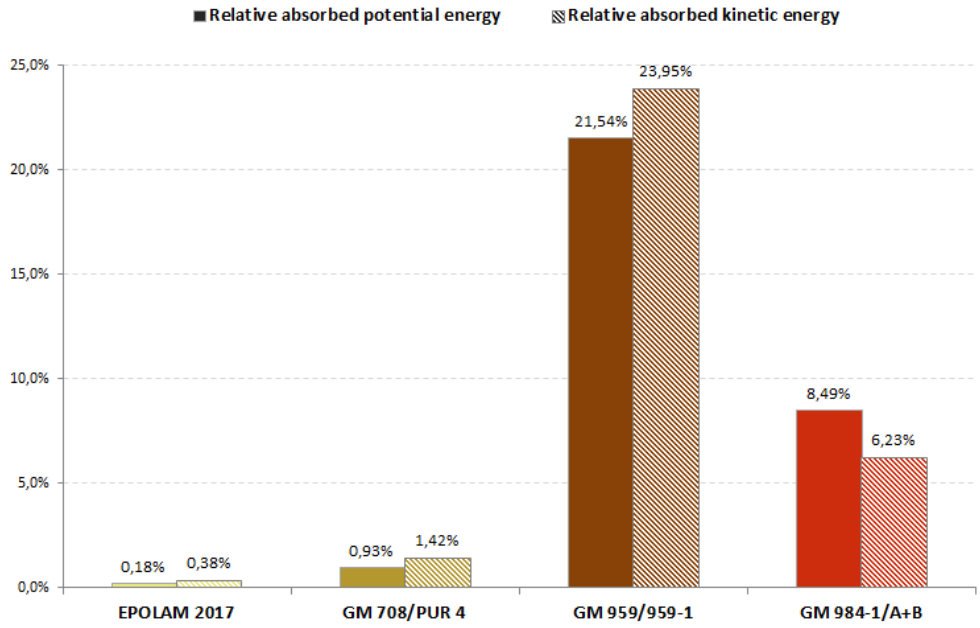

Figure 51. *Relative absorption of polymeric resins used for preparation of hybrid ceramic composites.*

5.5 Mechanical properties of indirectly 3D printed + ice-templated and robocast HAP scaffolds

Mechanical performance under uniaxial compressive stresses was evaluated for ice-templated scaffolds sintered at 1200 °C/2h, and for robocast scaffolds sintered at 950 °C/2h, and 1200 °C/2h. The results from the compressive strength measurements obtained are summarized in Figure 52, together with the total porosity results presented in previous sections.

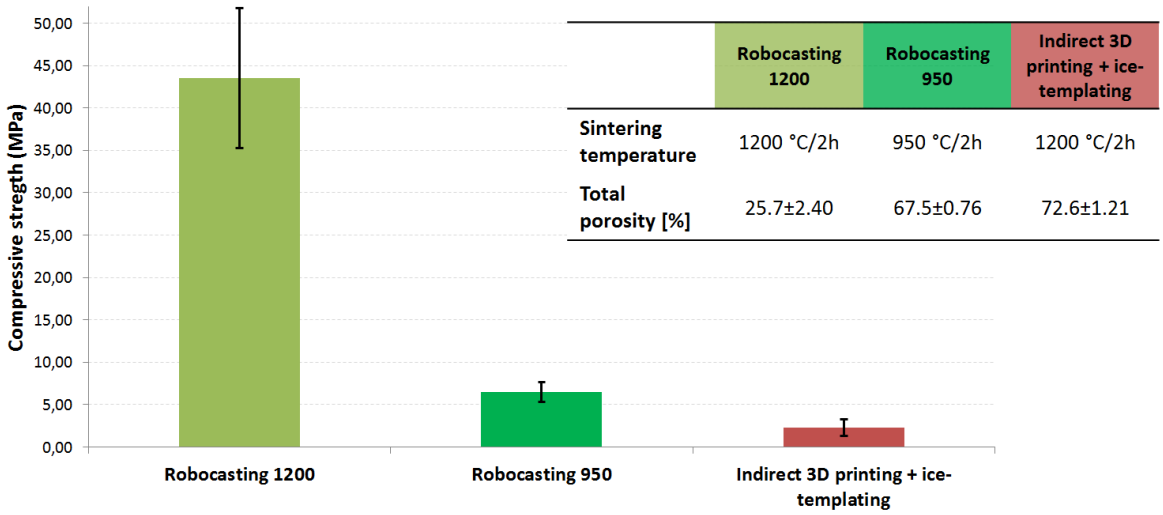

	Robocasting 1200	Robocasting 950	Indirect 3D printing + ice-templating
Sintering temperature	1200 °C/2h	950 °C/2h	1200 °C/2h
Total porosity [%]	25.7±2.40	67.5±0.76	72.6±1.21

Figure 52. *A comparison of compressive strengths and porosities of manufactured scaffolds.*

As expected, a good inverse correlation is found between total porosity results and compressive strength. The highest compressive strength was achieved in samples fabricated by robocasting and sintered at 1200 °C, whose average value reached 43.5 ± 8.24 MPa. Significantly lower compressive strength values were obtained by both, robocast samples sintered at 950 °C and ice-templated samples sintered at 1200 °C. The average strength values reached 6.5 ± 1.19 MPa and 2.3 ± 1.00 MPa, respectively in those cases.

5.6 Mechanical properties of hybrid alumina/epoxy composites

The results of density, alumina volume fraction, elastic modulus, fracture toughness and strength characteristics of all hybrid alumina/epoxy composites are summarized in Table 10.

Table 10. *Density, alumina volume fraction, elastic modulus, fracture toughness and strength characteristics of all hybrid composites.*

Material		25S	30S	35S	40S	45S
Density	[g·cm^{-3}]	2.36 ± 0.076	2.41 ± 0.001	2.68 ± 0.112	2.69 ± 0.026	3.06 ± 0.069
Al_2O_3 vol. fraction	[vol.%]	44.4	50.7	55.1	59.4	64.9
E-modulus out of plane	[GPa]	63.3 ± 13.00	76.3 ± 1.25	147.9 ± 22.39	124.6 ± 6.28	127.0 ± 13.00
E-modulus in plane	[GPa]	70.0 ± 4.45	77.1 ± 0.38	167.6 ± 29.59	127.0 ± 2.99	131.0 ± 30.67
Fracture toughness	[MPa·m$^{1/2}$]	2.11 ± 0.595	2.92 ± 0.404	2.23 ± 0.703	2.28 ± 0.605	2.57 ± 0.605
Weibull strength	[MPa]	81.4 (72.2 - 85.6)	88.9 (82.5 - 93.1)	117.0 (92.3 - 125.9)	115.6 (94.4 - 126)	89.7 (81.5 - 98.3)
Weibull modulus	[-]	4.3 (3.2 - 5.4)	7.1 (4.5 - 7.8)	3.6 (2 - 3.9)	3 (1.9 - 3.3)	4.3 (2.8 - 4.6)

The low density of hybrid composites is one of the main advantages and in this case varies from 2.4 g·cm^{-3} to 3.1 g·cm^{-3} linearly depending on the used amount of ceramics during processing according to the rule of mixture. The corresponding trend can be observed in alumina volume fraction in the composites. The different situation is with the elastic modulus measured by the impulse excitation method where two levels of values are detectable independently of the measured orientation. The lower level approximately of 70 GPa is dedicated to materials 25S and 30S. The second level is more than doubled comparing to the previous one with the average value laying at approximately 140 GPa is dedicated to the others hybrid composites. The scatter which is partially connected to the relatively low number of measured specimens, and also indicates the relatively low level of microstructure inhomogeneity in the tested materials.

The elastic modulus of composites depends on the components and porosity present, and as it is presented in this work microstructural orientation of formed lamellae plays a role. Therefore, two orientations of bar specimens were examined and averaged to obtain reasonable information about the elastic behavior of hybrid composite materials. Note that the elastic modulus is determined according to the standard for monolithic materials [76], therefore the absolute values are indicative but trends describe well the behavior of materials. Evolution of the elastic modulus and density detects a rapid increase in case of material 35S followed by a slight decrease for the material 45S. This is connected with a change in the lamellae distribution and cross-linking of the epoxy filler within the ceramic matrix.

The fracture behaviour was monitored by both the fracture toughness and the flexural strength measurements. The values of fracture toughness measured by the chevron notch technique are shown for all materials in the Figure 53 and demonstrated by individual data points together with average values accompanied by error bars indicating the scatter are plotted.

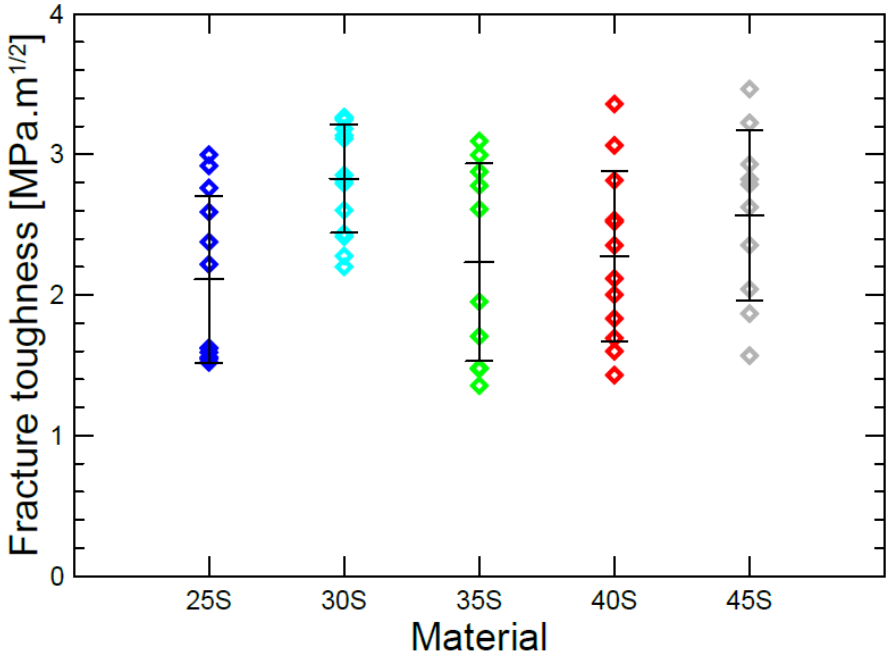

Figure 53. *Fracture toughness data for all materials with indicated average values and error bars.*

The fracture toughness data are in summary also numerically expressed in Table 10. All fracture toughness values are in the range between values for pure epoxy (ca 1.6 MPa·m$^{1/2}$) and fully dense

alumina (3.8 MPa·m$^{1/2}$). The composite material 30S exhibits slightly higher values which will be discussed further in detail.

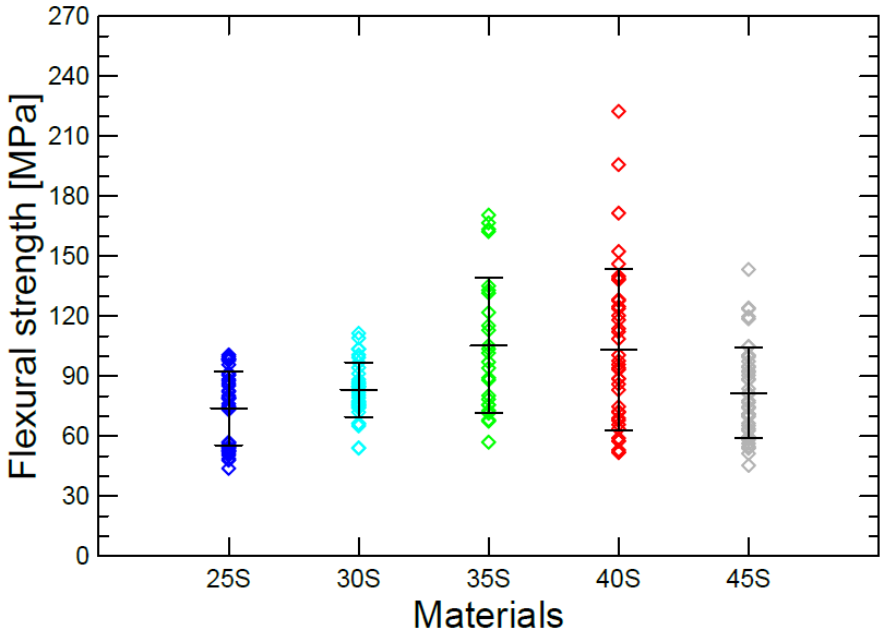

Figure 54. *Flexural strength data for all materials with indicated average values and error bars.*

The flexural strength data are summarised from the statistical point of view using Weibull analysis in Table 10, and also all data points, average values, and error bars are shown in Figure 54. The flexural strength data suffer from a significant level of the scatter (see for example material 40S) although the number of values in the data set is sufficient (more than 30). The minimal flexural strength values drop down to 40 MPa and the maximal flexural strength values reach more than 200 MPa.

5.7 Ballistic testing of hybrid alumina/polymer composites

Ballistic tests of hybrid Al_2O_3/epoxy composites

Hybrid alumina/epoxy composite plates, prepared as described above, with total thickness of 18.0 mm were subjected to ballistic testing using 7.62 mm x 54R B32 API projectiles. Set of five hybrid ceramic laminates Al_2O_3/epoxy resin prepared for ballistic testing, where the ice-templated wafers were made from 45 vol.% Al_2O_3 suspension (ICE Al_2O_3 45S), is shown in Figure 55.

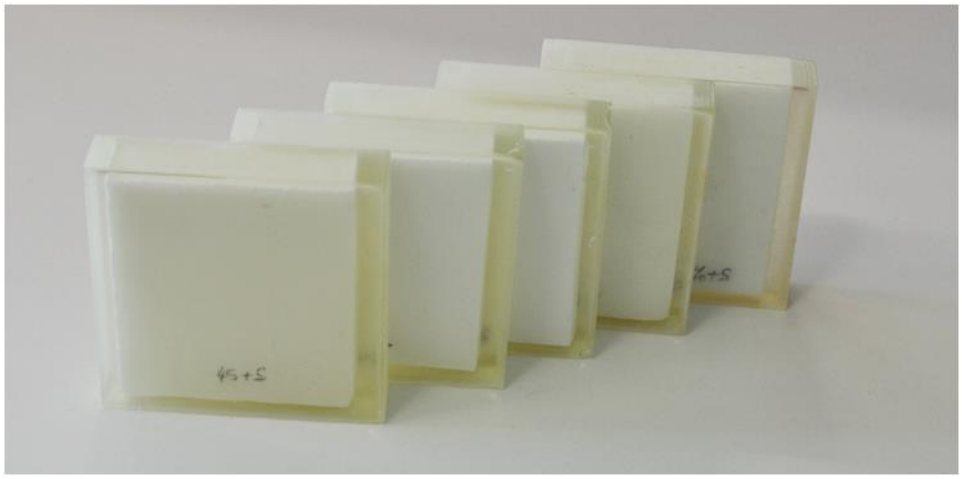

Figure 55. *Hybrid ceramic composites Al_2O_3/epoxy resin (EPOLAM 2017) prepared for ballistic testing.*

Selected ice-templated Al_2O_3 /epoxy resin hybrid composites characteristics as well as results of DOP ballistic tests are stated in Table 11.

Table 11. *DOP ballistic tests results of ICE Al_2O_3 45S / EPOLAM 2017 composites.*

Sample	Weight [g]	Areal density [kg·m^{-2}]	Projectile speed [m·s^{-1}]	DOP nom. [mm]	DOP meas. [mm]	DOP cor. [mm]
A/Epolam (1)	181.29	32.23	853.4	52.0	36.1	36.2
A/Epolam (2)	183.59	32.64	860.3	52.6	37.0	36.4
A/Epolam (3)	193.77	34.45	851.2	51.8	29.5	29.8
A/Epolam (4)	186.75	33.20	849.0	51.6	33.8	34.3
A/Epolam (5)	184.22	32.75	862.2	52.8	36.9	36.1

The average areal density of hybrid alumina/epoxy composites was 33.1 kg·m^{-2} and average corrected depth of penetration (DOP cor.) into aluminium block was 34.6 mm, with no significant difference between samples.

Ballistic tests of porous Al_2O_3/dense Al_2O_3 layer/polymer hybrid composites

Hybrid ice-templated porous alumina/dense alumina layer/epoxy composite plates, prepared as described above, with total thickness of 20.0 mm and 3.2 mm thickness of the slip cast plate were subjected to ballistic testing using 7.62 mm x 54R B32 API projectiles. Set of five hybrid ceramic composites porous Al_2O_3/dense Al_2O_3 /epoxy resin was prepared for ballistic testing. The ice-templated wafers were made from 30 vol.% Al_2O_3 suspension (ICE Al_2O_3 30S) and the slip cast plate was made from 50 vol.% Al_2O_3 suspension (Slip 50S). The appearance of hybrid composites after ballistic testing is shown in Figure 56.

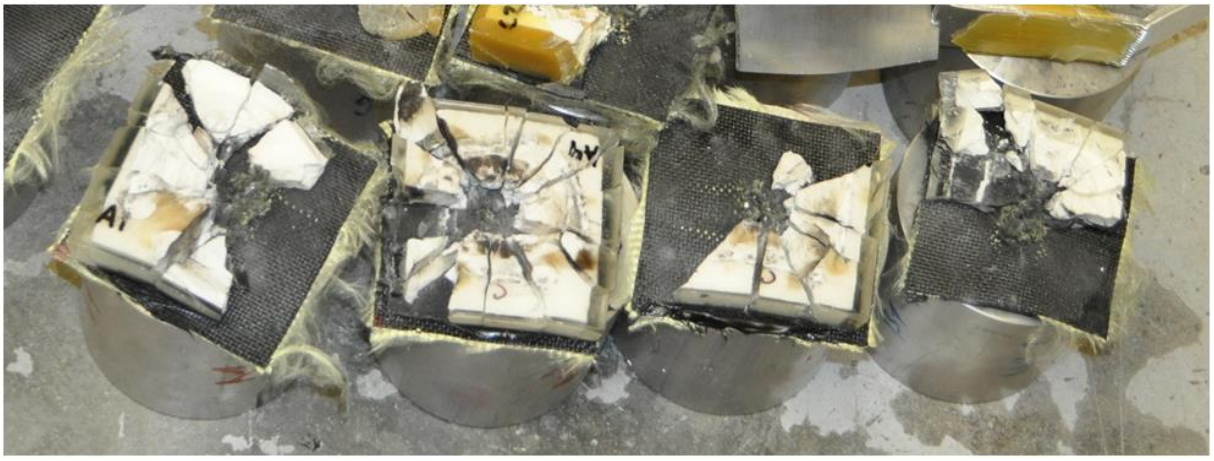

Figure 56. *Hybrid porous Al_2O_3/dense Al_2O_3/epoxy resin (EPOLAM 2017) composites after ballistic testing.*

Selected porous Al_2O_3/dense Al_2O_3/epoxy resin hybrid composites characteristics as well as results of ballistic tests are stated in Table 12.

Table 12. *DOP ballistic test results of ICE Al_2O_3 30S/Slip 50S_plate 3.2 mm/ EPOLAM 2017 composites.*

Sample	Weight [g]	Areal density [kg·m^{-2}]	Projectile speed [m·s^{-1}]	DOP nom. [mm]	DOP meas. [mm]	DOP cor. [mm]
A/Ap/Epolam (1)	143.97	25.59	853.8	52.0	22.1	22.1
A/Ap/Epolam (2)	146.28	26.01	850.5	51.7	14.5	14.8
A/Ap/Epolam (3)	144.35	25.66	857.3	52.3	29.5	29.2
A/Ap/Epolam (4)	147.94	26.30	850.6	51.7	17.7	18.0
A/Ap/Epolam (5)	137.15	24.38	852.6	51.9	18.5	18.6

The average areal density of hybrid alumina/epoxy composites with 3.2 mm slip cast dense layer was 25.6 kg·m^{-2} and average corrected depth of penetration (DOP cor.) into aluminium block was 20.5 mm. Ballistic performance of the sample number 3 was worse (DOP cor. 29.2 mm) in comparison with other composites. This deviation was probably caused by some microstructural defect, e.g. crack, in slip cast dense alumina layer.

Hybrid ice-templated porous alumina/dense alumina layer/polyurethane resin (GM 708/ PUR 4) composite plates were prepared as described above The total thickness of composites was 20 mm and the thickness of the slip cast layer was 3.2 mm. The hybrid composites were subjected to ballistic testing using 7.62 mm x 54R B32 API projectiles. Set of four hybrid ceramic composites porous Al_2O_3/dense Al_2O_3 layer/ polyurethane resin (GM 708/ PUR 4) was prepared for ballistic testing. The ice-templated wafers were made from 30 vol.% Al_2O_3 suspension (ICE Al_2O_3 30S) and the slip cast plate was made from 50 vol.% Al_2O_3 suspension (Slip 50S). The appearance of hybrid composites after ballistic testing is shown in Figure 57.

Figure 57. *Hybrid porous Al_2O_3/dense Al_2O_3/polyurethane resin (GM 708/PUR4) composites after ballistic testing.*

Selected ice-templated Al_2O_3/dense Al_2O_3/polyurethane resin (GM 708/ PUR 4) hybrid composites characteristics as well as the results of ballistic tests are stated in Table 13.

Table 13. *DOP ballistic test results of ICE Al_2O_3 30S / Slip 50S_plate 3.2 mm / GM 708/PUR4 composites.*

Sample	Weight [g]	Areal density [kg·m^{-2}]	Projectile speed [m·s^{-1}]	DOP nom. [mm]	DOP meas. [mm]	DOP cor. [mm]
A/Ap/GM 708/PUR4 (1)	189.75	35.61	848.0	51.5	11.5	12.1
A/Ap/GM 708/PUR4 (2)	201.33	37.78	854.5	52.1	13.5	13.5
A/Ap/GM 708/PUR4 (3)	184.65	34.65	840.7	50.8	28.4	29.6
A/Ap/GM 708/PUR4 (4)	198.08	37.17	848.8	51.5	35.0	35.5

The average areal density of hybrid alumina/polyurethane composites with 3.2 mm slip cast dense layer was 36.3 kg·m^{-2} and average corrected depth of penetration (DOP cor.) into aluminium block was 12.8 mm in the case of samples 1 and 2, and 32.6 mm in the case of samples 3 and 4. This discrepancy in ballistic performance can be explained by presence of microstructural defects, e.g. crack in the slip cast dense alumina layer. The most probable cause was not fully infiltrated ice-templated part of the composites.

Hybrid porous alumina/dense alumina layer/polyurethane resin (GM 959/959-1) composite plates were prepared as described above, with total thickness of 12.0 mm (4.0 mm thickness of the slip cast layer) were subjected to ballistic testing using 7.62 mm x 54R B32 API projectiles. Set of five hybrid ceramic composites porous Al_2O_3/dense Al_2O_3 layer/ polyurethane resin (GM 959/959-1) was prepared for the ballistic testing. The ice-templated wafers were made from 30 vol.% Al_2O_3 suspension (ICE Al_2O_3 30S) and the slip cast plate was made from 50 vol.% Al_2O_3 suspension (Slip 50S). The appearance of hybrid composites after ballistic testing is shown in Figure 58.

Figure 58. *Hybrid porous Al_2O_3/dense Al_2O_3/polyurethane resin (GM 959/959-1) composites after ballistic testing.*

Selected ice-templated Al_2O_3/dense Al_2O_3/polyurethane resin (GM 959/959-1) hybrid composites characteristics as well as the results of ballistic tests are stated in Table 14.

Table 14. *DOP ballistic test results of ICE Al_2O_3 30S / Slip 50S_plate 4.0mm / GM 959/959-1 composites.*

Sample	Weight [g]	Areal density [kg·m^{-2}]	Projectile speed [m·s^{-1}]	DOP nom. [mm]	DOP meas. [mm]	DOP cor. [mm]
A/Ap/GM 959 (1)	120.23	29.35	845.9	51.3	26.2	27.0
A/Ap/GM 959 (2)	120.87	29.51	850.8	51.7	23.5	23.8
A/Ap/GM 959 (3)	120.75	29.48	850.0	51.7	18.8	19.2
A/Ap/GM 959 (4)	121.32	29.62	856.0	52.2	17.9	17.7
A/Ap/GM 959 (5)	123.30	30.10	858.0	52.4	22.8	22.4

The average areal density of hybrid alumina/polyurethane composites with 4.0 mm slip cast dense layer was 29.6 kg·m^{-2} and average corrected depth of penetration (DOP cor.) into aluminium block was 22.0 mm. Ballistic performance of the sample number 1 was slightly worse (DOP cor. 27.0 mm) in comparison with other composites.

Hybrid porous alumina/dense alumina plate/ polyurethane resin (GM 984-1/A+B) composite plates, prepared as described above, with total thickness of 13.0 mm and 3.7 mm thickness of the slip cast plate were subjected to ballistic testing using 7.62 mm x 54R B32 API projectiles. Set of five hybrid ceramic composites porous Al_2O_3/dense Al_2O_3 plate/ polyurethane resin (GM 984-1/A+B) was prepared for ballistic testing. The ice-templated wafers were made from 30 vol.% Al_2O_3 suspension (ICE Al_2O_3 30S) and the slip cast plate was made from 50 vol.% Al_2O_3 suspension (Slip 50S). The appearance of hybrid composites after ballistic testing is shown in Figure 59.

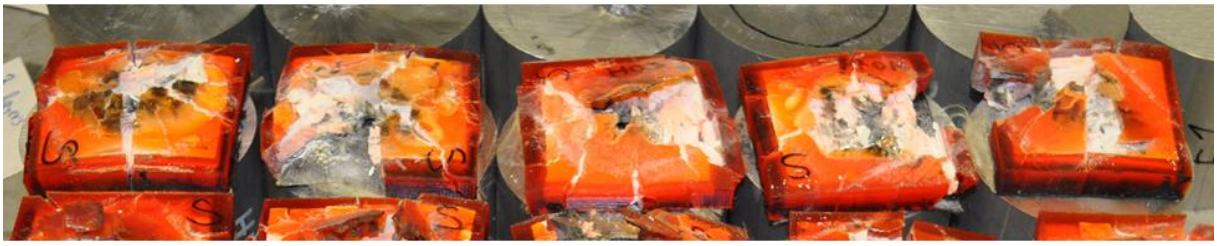

Figure 59. *Hybrid porous Al_2O_3/dense Al_2O_3/polyurethane resin (GM 984-1/A+B) composites after ballistic testing.*

Selected ice-templated Al_2O_3/dense Al_2O_3 plate/polyurethane resin (GM 984-1/A+B) hybrid composites characteristics as well as the results of ballistic tests are stated in Table 15.

Table 15. *DOP ballistic test results of ICE Al_2O_3 30S / Slip 50S_plate 3.7 mm / GM 984-1/A+B composites.*

Sample	Weight [g]	Areal density [kg·m^{-2}]	Projectile speed [m·s^{-1}]	DOP nom. [mm]	DOP meas. [mm]	DOP cor. [mm]
A/Ap/GM 984-1 (1)	175.20	32.88	855.0	52.1	26.2	26.1
A/Ap/GM 984-1 (2)	179.60	33.70	857.1	52.3	21.0	20.7
A/Ap/GM 984-1 (3)	180.47	33.87	859.8	52.6	21.4	20.9
A/Ap/GM 984-1 (4)	160.50	30.12	856.0	52.2	24.4	24.2
A/Ap/GM 984-1 (5)	167.85	31.50	855.8	52.2	19.3	19.1

The average areal density of hybrid alumina/polyurethane composites with 3.7 mm slip cast dense layer was 32.4 kg·m^{-2} and the average corrected depth of penetration (DOP cor.) into aluminium block was 22.2 mm, with no significant difference among samples.

Ballistic tests of porous Al_2O_3/segmented dense Al_2O_3 /polymer hybrid composites

Hybrid porous alumina/segmented dense alumina/polyurethane resin (GM 984-1/A+B) composite plates, prepared as described above, with total thickness of 17.0 mm and 6.0 mm thickness of the hexagonally divided plate (slip cast directly on ice-templated wafer) were subjected to ballistic testing using 7.62 mm x 54R B32 API projectiles. Set of five hybrid ceramic composites

porous Al_2O_3/segmented dense Al_2O_3 /polyurethane resin (GM 984-1/A+B) was prepared for ballistic testing. The ice-templated wafers were made from 30 vol.% Al_2O_3 suspension (ICE Al_2O_3 30S) and the slip cast plate was made from 50 vol.% Al_2O_3 suspension (Slip 50S). The appearance of hybrid composites after ballistic testing is shown in Figure 60.

Figure 60. *Hybrid porous Al_2O_3/segmented dense Al_2O_3/polyurethane resin (GM 984-1/A+B) composites after ballistic testing.*

Selected ice-templated Al_2O_3/segmented dense Al_2O_3/polyurethane resin (GM 984-1/A+B) hybrid composites characteristics as well as the results of ballistic tests are stated in Table 16.

Table 16. *DOP ballistic test results of ICE Al_2O_3 30S / Slip 50S_hexagons 6.0 mm / GM 984-1/A+B composites.*

Sample	Weight [g]	Areal density [kg·m^{-2}]	Projectile speed [m·s^{-1}]	DOP nom. [mm]	DOP meas. [mm]	DOP cor. [mm]
A/Ahex/GM 984-1 (1)	171.60	32.20	856.6	52.3	35.2	35.0
A/Ahex/GM 984-1 (2)	170.00	31.90	858.9	52.5	14.9	14.4
A/Ahex/GM 984-1 (3)	160.75	30.17	867.8	53.3	15.4	14.1
A/Ahex/GM 984-1 (4)	175.45	32.92	857.0	52.3	29.4	29.1
A/Ahex/GM 984-1 (5)	169.90	31.88	864.8	53.0	24.2	23.2

The average areal density of hybrid alumina/polyurethane composites with 6.0 mm slip cast hexagonally divided dense layer was 31.8 kg·m^{-2} and average corrected depth of penetration (DOP cor.) into aluminium block was 23.2 mm. There was a significant difference between ballistic performance of samples number 2 and 3 (DOP cor. 14.3 mm) and the rest of composites. This discrepancy and generally large scatter in depth of penetration results are showing that dividing of slip cast dense layer into hexagonal segments brought more negatives than positives. Borders of

hexagonal segments were acting as stress concentrators, so the slip cast layer was pre-cracked and wasn´t able to stop the projectile effectively.

Hybrid porous alumina/segmented dense alumina/polyurethane resin (GM 959/959-1) composite plates, prepared as described above, with total thickness of 17.0 mm and 10.0 mm thickness of dense hexagons (slip cast separately on gypsum mold) were subjected to ballistic testing using 7.62 mm x 54R B32 API projectiles. Set of five hybrid ceramic composites porous Al_2O_3/segmented dense Al_2O_3/polyurethane resin (GM 959/959-1) was prepared for ballistic testing. The ice-templated wafers were made from 30 vol.% Al_2O_3 suspension (ICE Al_2O_3 30S) and the slip cast hexagons were made from 55 vol.% Al_2O_3 suspension (Slip 55S). The appearance of hybrid composites after ballistic testing is shown in Figure 61.

Figure 61. *Hybrid porous Al_2O_3/segmented dense Al_2O_3/polyurethane resin (GM 959/959-1) composites after ballistic testing.*

Selected ice-templated Al_2O_3/segmented dense Al_2O_3/polyurethane resin (GM 959/959-1) hybrid composites characteristics as well as the results of ballistic tests are stated in Table 17.

Table 17. *DOP ballistic test results of ICE Al_2O_3 30S/Slip 55S_hexagons 10.0 mm / GM 959/959-1 composites.*

Sample	Weight [g]	Areal density [kg·m^{-2}]	Projectile speed [m·s^{-1}]	DOP nom. [mm]	DOP meas. [mm]	DOP cor. [mm]
A/Ahex/ GM 959 (1)	118.31	39.57	845.5	51.2	1.8	2.6
A/Ahex/ GM 959 (2)	117.10	39.16	845.5	51.2	8.4	9.2
A/Ahex/ GM 959 (3)	122.75	41.05	865.5	53.1	5.0	3.9
A/Ahex/ GM 959 (4)	115.71	38.70	856.2	52.2	6.1	5.9
A/Ahex/ GM 959 (5)	114.59	38.33	851.9	51.8	8.1	8.3

The average areal density of hybrid alumina/polyurethane composites with 6.0 mm slip cast hexagonally divided dense layer was 39.4 $kg \cdot m^{-2}$ and average corrected depth of penetration (DOP cor.) into aluminium block was 6.0 mm. Ballistic performance of samples number 2 and 5 was slightly worse in comparison with other composites. This was most probably caused due to the impact of projectile in the "weak point" (border between slip cast hexagons), so it was easier for the projectile to penetrate deeper in the aluminium block.

Summary of hybrid composites ballistic performance

Average thicknesses, areal densities and corrected DOPs of all hybrid composites as well as of the slip cast alumina plates are stated in Table 18. Set of five dense (relative density of 98.5 %) plates were slip cast from 55 vol.% Al_2O_3 suspension (Slip 55S) on gypsum mold, sintered at 1550 °C/2h, prepared for ballistic testing in the same way as hybrid composites, and subjected to ballistic testing using 7.62 mm x 54R B32 API projectiles.

Table 18. *Summary of DOP ballistic test results of all hybrid composites and dense alumina plates.*

Type of composite	Total thickness [mm]	Dense alumina thickness [mm]	Areal density [$kg \cdot m^{-2}$]	DOP cor. [mm]
A/Epolam	18.0	-	33.1	34.6
A/Ap/Epolam	20.0	3.2	25.6	20.5
A/Ap/GM 708/PUR4	20.0	3.2	36.3	22.7
A/Ap/GM 959	12.0	4.0	29.6	22.0
A/Ap/GM 984-1	13.0	3.7	32.4	22.2
A/Ahex/GM 984-1	17.0	6.0	31.8	23.2
A/Ahex/ GM 959	17.0	10.0	39.4	6.0
Dense alumina	7.0	7.0	26.9	4.3

The best ballistic performance together with lowest areal density among all hybrid ice-templated alumina/ slip cast alumina plate/polymer composites showed composite A/Ap/Epolam with average areal density of 25.6 $kg \cdot m^{-2}$ and average corrected depth of penetration of 22.2 mm.

The lowest average DOP among all hybrid composites was measured after ballistic testing of composites A/Ahex/ GM 959, where the DOP cor. reached value of 6.0 mm. Such low depth of penetration is superior to all other hybrid composites and it is comparable to ballistic performance of dense alumina plates (DOP cor. 4.3 mm). However, the areal density of dense Al_2O_3 plates is significantly lower than areal density of hybrid composites A/Ahex/ GM 959 (~26.9 $kg \cdot m^{-2}$ vs. 39.4 $kg \cdot m^{-2}$) and moreover the thickness of alumina plate is by 10 mm lower than in case of the hybrid composite.

6 Discussion

6.1 Ice-templating – design of microstructure

Ice-templating was successfully used for preparation of porous lamellar structures from alumina with relative porosity from 35.1 % to 55.6 %, and used for manufacturing of hybrid ceramic/polymer composites. Furthermore HAP scaffolds with relative porosity from 79.8 % to 91.1 % were prepared for bio-applications.

Main changing parameter was solid loading of starting water-based suspensions used for ice-templating. It ranged from 25 vol.% to 45 vol.% in the case of Al_2O_3 powder, and from 7.5 vol.% to 20 vol.% in the case of HAP powder.

Very important parameter of ice-templated structures is the interlamellar distance which highly influences ability of polymeric resins to fully infiltrate alumina wafers during hybrid composites preparation or successful bone growth into hydroxyapatite scaffolds. Interlamellar distance reached values from about 60 μm to 130 μm (see Table 8) in the case of Al_2O_3 wafers, and from 60 μm to 89 μm (see Table 9) in the case of HAP scaffolds. When ice-templating combined with indirect 3D printing was used for manufacturing of HAP scaffolds, the diameter of introduced macro channels was about 500 μm.

Another important microstructural feature which influences the mechanical stability is presence of interlamellar bridges between adjacent ceramic lamellae. Additives (PVA, sugar, dextrin, etc.) that are used in starting suspensions to control lamellar bridges are working on mechanism of splitting and healing ice crystal tips, which can result in the encapsulation of ceramic particles and the formation of bridges between lamellae. Each additive affects interfacial tension and forces between ceramic particles as it was shown by Munch et al. [25]. The best additive, in terms of interlamellar bridges formation and appearance, has proven to be 3 wt.% of sugar. The sugar addition introduces an interfacial instability at the solidification front which promotes side branching during directional solidification [86]. The main drawback of sugar addition is the need for careful lyofilization, due to the glassy phase presence which could easily destroy internal structure when overheated.

Ice-templated alumina scaffolds for hybrid composites

The first step in manufacturing of hybrid ceramic/polymer composites is preparation of ice-templated scaffolds/wafers from alumina suspensions. It was possible to prepare alumina wafers from all used suspensions (solid loading from 25 to 45 vol.%) with porosity ranging from about 56 % to 35 %, and inversely correlating interlamellar distances from about 130 μm to 60 μm, see Table 8. These results are corresponding with works of other authors dealing with ice-templating of water-based alumina suspensions [6; 31; 87].

After sintering at 1550 °C/2 h in air, the alumina lamellae are completely dense with almost no visible residual porosity (Figure 35c). The surface of the lamellae exhibits dendritic-like bridges between adjacent lamellae (Figure 36), due to the addition of 3 wt.% of sugar. As it was pointed out in other works [9; 25; 87], these interconnecting bridges play crucial role not only in final mechanical properties of sintered alumina wafers and prepared hybrid ceramic/polymer composites, but also in the green body strength of ice-templated wafers after sublimation of ice crystals. Sugar addition plays important role in the green body strength enhancement and it also behaves as an organic binder.

Indirectly 3D printed + ice-templated vs. robocast HAP scaffolds

Ice-templated scaffolds, especially combined with indirect 3D printing, seems to be a promising method for preparation of bioceramic scaffolds for bone replacement with the multiscale porosity, including a well-defined interconnected macro-channel network for. It has to be mentioned there that it is not the first time that ice-templating combined with fugitive polymeric template was used. For example Han et al. [88] used polyurethane foam impregnated with alumina suspension which was directionally frozen subsequently, and Reed et al. [89] used 3D printed ABS templates to introduce channels into directionally frozen chitosan-alginate scaffolds. Robocasting was used as a comparative technique to produce scaffolds with comparable porosity at the introduced macroporosity and the inter-grain microporosity levels.

Both methods, indirect 3D printing combined with ice-templating and robocasting can produce scaffolds with similar porosity in the submicron and hundreds of microns range. However, it is necessary to implement significantly different sintering conditions (950 °C/2h vs. 1200 °C/2h). Furthermore, ice-templating process introduces in the structure a new interlamellar porosity in the tens of microns range, see Figures 27 and 40. As a consequence, ice-templated scaffolds total porosity could be much higher than porosity achieved by robocasting using the same sintering conditions (thus, maintaining the same size of introduced macropores), and even higher than in the case of robocast scaffolds sintered at much lower temperature (950 °C), see Figure 41 and Figure 52.

Advantages of ice-templating combined with indirect 3D printing are the possibility to achieve multiscale pore sizes and an increased connection of internal porosity (micro and macro channels). These are crucial features of bioceramic scaffolds necessary for controlling and enhancing the biological activity. The relationship between bioceramic scaffolds porosity, pore size distribution and cell activity is still not well understood but previous studies have pointed out that a range of mean pore sizes convenient for cell attachment lies in range 96–150 μm [43; 90; 91], but for successful bone growth into scaffolds are necessary larger pores (300–800 μm) [43]. These results indicate that scaffolds with wide range of pore sizes could be beneficial to achieve optimal cell attachment and facilitating bone regeneration. The wide pore size distribution of indirectly 3D printed and ice-templated samples (Figure 41) could be thus optimal. Moreover, the porosity created by ice crystals fits nicely within the range of the optimal pore size for cell attachment, while macroporosity introduced by the PLA 3D mesh fits in the range allowing easy bone growth in whole volume of the scaffold.

Moreover it was shown by other authors [92; 93] that micro roughness of bioceramic scaffolds can considerably stimulate the adhesion, spreading and proliferation of osteoblastic cells. Such micro roughness is naturally formed during ice-templating on lamellae surface due to the sugar addition to starting suspension. Further tailoring of the surface roughness for particular biomedical applications is possible by various additives addition into starting suspensions.

Grain size and phase composition of ice-templated samples revealed to be unexpectedly different compared to the robocast samples or previous experiences with hydroxyapatite powders [94; 95]. Grain sizes of the robocast and ice-templated samples are demonstrated in Figure 62.

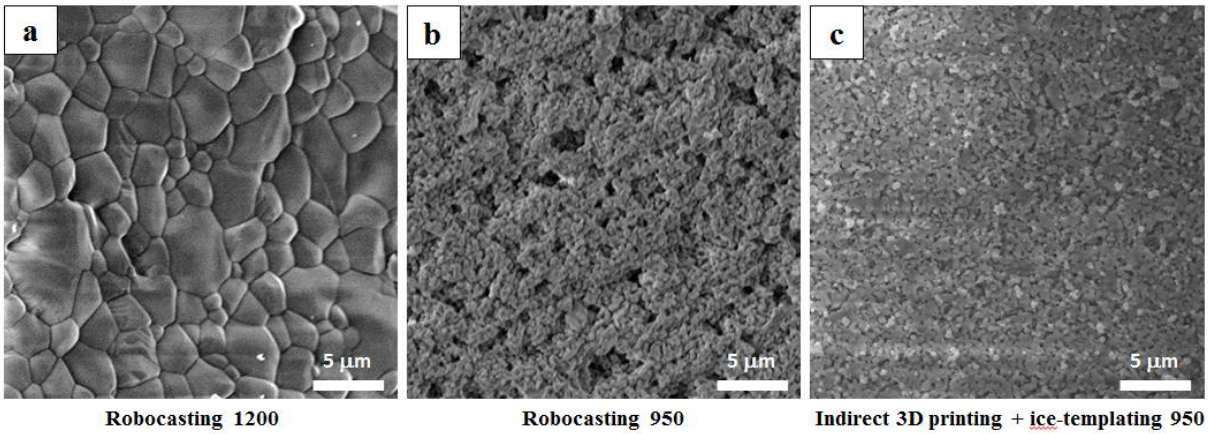

Figure 62. *Microstructural details of the prepared samples after sintering.*

Ice-templating process limited a grain growth, the grain size is around 500 nm at a sintering temperature of 1200 °C (Figure 62c), which is a size comparable to the grain size of robocast samples sintered at 950 °C (Figure 62b) but much smaller than those found in robocast samples sintered at the same 1200 °C (~2.5 µm, Figure 62a). Change of the sintering behavior after ice-templating had already been observed previously for alumina by Zheng et al. [8], but here the ice-templating seems to affects also the phase transformation of hydroxyapatite to Whitlockite at elevated temperature, according to the results summarized in Figure 42. The change of the shrinkage behavior is related to change of porosity distribution and length of the diffusion path. The dilatometric measurement, shown in Figure 42, demonstrates that densification of the HAP powder after freezing is shifted to high temperature. This suggests that similar levels of densification are connected with the similar phase transformation, however it is difficult to identify main reason due to complexity of the HAP phase transformation [95]. The porosity can influence diffusion process or gas release during the heat treatment, however very high mechanical pressure, in terms of hundreds of MPa [8] caused by expansion of water during freezing can also play a role. Furthermore, the difference in the final microstructure at 1200 °C (see Figure 62) is tremendous compared to relatively small difference in phase composition (see Figure 42).

Further research is necessary to fully reveal the impact of mechanical pressure during ice-templating and introduced porosity on grain growth or phase transformation. Anyhow, this study has clearly revealed that ice-templating is a suitable strategy for tailoring of porosity, grain size and even phase compositions in bioceramic scaffolds for bone tissue engineering applications.

6.2 Hybrid ceramic/polymer composites

Hybrid composites from ice-templated alumina/various resins were successfully prepared by ice-templating of alumina-water based suspensions followed by the resin infiltration. Despite some structural defects caused by ice-templating and infiltration process, it was possible to prepare lamellar materials with lamellae length up to 70 mm and thickness up to 10 mm for all presented hybrid composites compositions. However, infiltration by polymer was much more difficult in the case of polyurethane resins (due to higher viscosity, see Table 7) It was nearly impossible to achieve full infiltration of ice-templated alumina body in the case of resin GM 959/959-1, because the time necessary for complete infiltration of alumina scaffold was longer than pot life of this resin (the pot

life is defined as the amount of time it takes for an initial mixed viscosity of the resin to double). The resin with such high viscosity wasn't able to penetrate into small interlamellar spaces

No significant influence of alumina content on an ability to form lamellae was observed although freezing conditions were constant for all mixtures, but optimization of ice-templating process for each suspension compositions can further improve the strength of alumina after sintering [6].

The low density of hybrid composites is one of their main advantages and in the case of alumina/epoxy resin hybrid composites varies from 2.4 $g \cdot cm^{-3}$ (in the case of 25S) to 3.2 $g \cdot cm^{-3}$ (in the case of 45S) linearly depending on used amount of the ceramics during processing according to the rule of mixture. The final ceramic to epoxy ratio follows initial amount of ceramic powder in water suspension, see Table 10. Additionally, due to inhomogeneity in the microstructure within the plate volume, the values and their scatter are influenced by the place of sample extraction.

SEM micrographs show recognisable lamellae formed by ice-templating filled by epoxy, see Figure 46, the shape and distances change with the increasing ceramic to polymer ratio. Distances of lamellae increase and shape of lamellae change from narrow long sharp closely packed chain of ribs to the wide short blunt partially separated ribs. When the ceramic solid load was too high clearly visible unfilled cavities were more frequently found (Figure 63b). However, observed differences between lamellae and inter-lamellar spacing were not fully corresponding with measured mechanical properties of the alumina/epoxy resin hybrid composites, see Table 10.

6.3 Mechanical properties

Mechanical properties of ice-templated scaffolds after sintering

Mechanical properties of ice-templated scaffolds after sintering (without any infiltration by polymer) were tested on indirectly 3D printed + ice-templated HAP scaffolds. Robocast scaffolds were used for comparison.

Regarding the compressive strength, the performance of robocast scaffolds, even those sintered at 950 °C, is superior to those fabricated by indirect rapid prototyping combined with ice-templating and sintered at 1200 °C (see Figure 52) due to the absence of interlamellar pores, and possibly slightly lower pre-designed macroporosity. Indeed, the flaws responsible for the crack propagation and precursors of fracture are bigger and more abundant in the ice-templated scaffolds, reducing the stress required for the initiation of failure in the sample. Although the intergranular porosity is greater in the robocast scaffolds sintered at 950 °C, this circumstance is not critical in terms of strength as smaller pores are not likely to be the precursors of fracture. Despite these apparently unfavorable results, mechanical stability of the ice-templated samples can be further tailored, and highly porous scaffolds fabricated by ice-templating can be mechanically more stable compared to competing techniques [6]. However, it would be necessary to evaluate the potentially negative impact of the expansion of the polymeric template in the ice-templated structure during the heat treatment, due to the difference of HAP (β-TCP) and PLA thermal expansion coefficients [94; 96; 97]. Another potential drawback of combining indirect rapid prototyping and ice-templating would be an influence of the polymeric template on the direction of freezing due to blocking of the freezing front. There is a limit in the volume of polymeric template introduced in the structure, due to the change of thermal capacity and conductivity of the mixture (polymeric template/ceramic suspension). Excessive amount of polymeric template can lead to a difficult control of ice lamellae growth direction (loss of the temperature gradient) during the freezing step. These problems could become significant if total volume of introduced polymeric template is significantly higher than in the presented example.

Mechanical properties of ice-templated ceramic/polymer hybrid composites

Mechanical properties of ice-templated ceramic/polymer hybrid composites were tested on alumina/epoxy resin composites with different solid loading of Al_2O_3 in starting suspensions.

The elastic modulus of composites depends on the components and porosity present, and as it is presented in this work microstructural orientation of formed lamellae plays a role. Therefore, two orientations of bar specimens were examined and averaged to obtain reasonable information about the elastic behaviour of hybrid composite materials. Note that the elastic modulus is determined according to the standard for monolithic materials, therefore the absolute values are indicative but trends describe well the behaviour of materials. Evolution of the elastic modulus and density detects a rapid increase in case of material 35S followed by a slight decrease for the material 45S. This is connected with a change in the lamellae distribution and cross-linking of the epoxy filler within the ceramic matrix as can be seen in Figure 46c. Even thou microstructures difference showed in Figure 46c for materials 25S, 35S and 45S are significant the fracture toughness values are comparable. This observation is closely linked to the determination method, fracture toughness using chevron notch technique measure usually some point at the beginning of R-curve. This method was successfully used previously and it was found more reliable for composite systems than other methods [98; 99; 100]. Moreover, the values obtained here are in good correlation with the literature data [61; 101].

Fracture toughness values determined using chevron notch technique showed in Figure 53 are in average values consistent and apparently independent of the ceramic solid loading, only the material 30S is different. Detail data analysis of the fracture toughness values shows that the most of the data sets consist two data subsets, i.e., the values controlled by epoxy (the fracture toughness of pure epoxy is about 1.6 $MPa \cdot m^{1/2}$) or by alumina (the fracture toughness of dense pure alumina is about 3.8 $MPa \cdot m^{1/2}$). In the case of material 30S, the group of epoxy controlled fracture is suppressed. This can be ascribed to the locally changed homogeneity of the composite comparing to others or as an effect of the relatively small data set. Additional information can be provided by the comparison of loading traces as is shown in Figure 63.

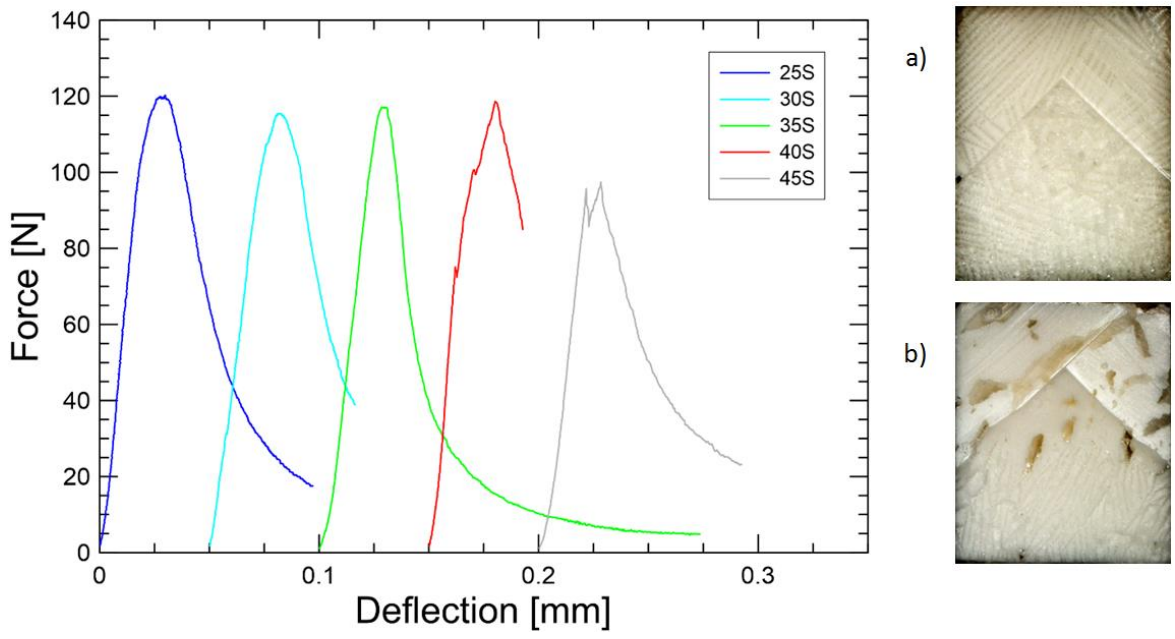

Figure 63. *Comparison of loading traces obtained during fracture toughness tests for all materials together with optical micrographs of corresponding fracture surfaces for a) 25S, and b) 45S material showing differences in the fracture behavior.*

All materials exhibited a stable crack propagation during loading only the material 45S (the highest of alumina content) showed significant pop-in behaviour. The shape of the loading curve well corresponds with shown fracture surface in Figure 64b, where are present zones containing epoxy, alumina or lamellar structure. Pop-ins are formed when the crack is stopped in one zone and reinitiated in another zone. Contrary, the regularly distributed lamellae in material 25S (see Figure 64a) led to the smooth loading curve confirming stable crack propagation.

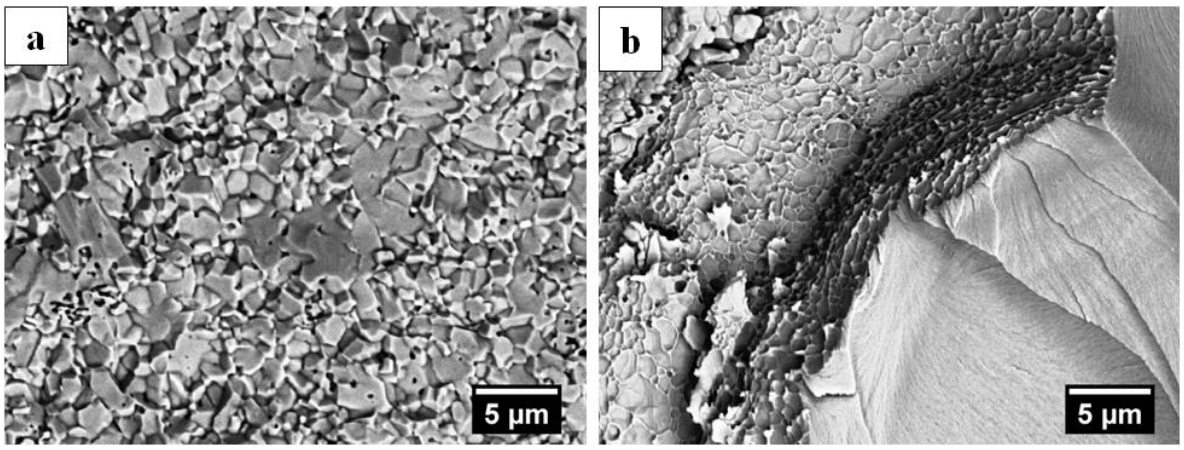

Figure 64. *The typical fracture surface of alumina (a) and epoxy (b) regions (BSE).*

Fracture behaviour of the hybrid composites is mostly dependent on the synergic effect of individual components. In this particular case both materials the alumina ceramic and used polymeric filler exhibits rather brittle behaviour as can be seen in Figure 46c, and in the detailed view in Figure 64. The alumina (left) exhibits mixed fracture mode, i.e., small grains shows mainly intergranular fracture and larger grains are fractured predominately trans-granularly. The presence of micro-porosity is a consequence of the processing route with minimal impact on the properties, because larger defects are present in the form of empty cavities or delaminated ceramic – epoxy interfaces due to shrinkage of the epoxy during its hardening (see Figure 65).

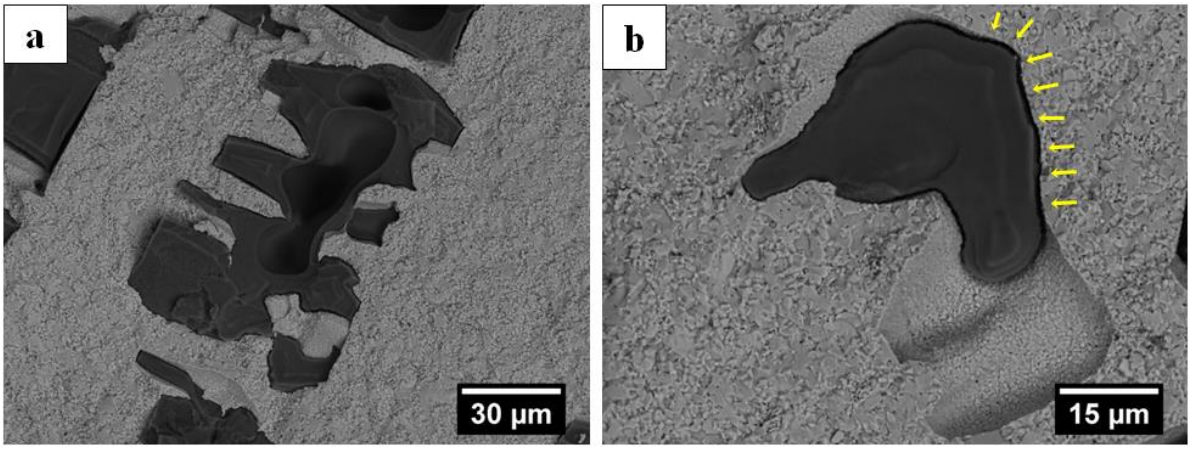

Figure 65. *Examples of the defects found in the microstructure for 45S material; a) bubbles inside the epoxy filling, b) unfilled spaces with ceramic epoxy delamination due to epoxy shrinkage, indicated by arrows (BSE).*

The epoxy fracture (Figure 64b) is characteristic by detectable fracture origin(s) and featured by the river like fracture marks showing the crack propagation direction typical for brittle materials

without grain structure like amorphous glasses. There are also locally present fracture steps when two cracks propagating in different plains are meeting as well as tongues or bridges as a result of localised plastic deformation when high stresses are present.

The optimal combination of ceramic microstructure and epoxy resin content was found for materials 35S and 40S which possess the increased strength, i.e., the lamellae distance was convenient and large pores (above 0.1 mm) were not present. The measure mechanical properties of these materials are comparable with the data presented in the literature. Additionally, huge advantages of the presented processing method are easy up scaling and significant reduction of processing steps compare to the literature, and the mechanical properties sustain on the comparable level [61].

6.4 Ballistic performance

The ballistic performance of ice-templated ceramic/polymer hybrid composites was tested on ice-templated alumina/epoxy resin composites and ice-templated alumina/slip cast alumina/resins composites. Slip cat dense alumina plates were used for comparison.

Ballistic performance of alumina/epoxy resin composites (Al_2O_3 45S/EPOLAM 2017) wasn't satisfying, because average corrected DOP of these composites was 34.6 mm. The average nominal DOP (depth of penetration into aluminium block without any added material) was 52.2 mm, which means that 18 mm of hybrid composite was able to lower the DOP by 17.6 mm. The main reason for such low ballistic performance can be found in the microstructure of composites. Alumina lamellae created by ice-templating are too thin to be able to effectively abrade the tip of projectile. The hybrid alumina/epoxy resin composite itself exhibits rather brittle fracture behaviour even during low-speed loading, which was proved by fracture toughness measurements, see Figure 63 and 64. The brittleness of these composites is even more emphasized during high-velocity loading after the projectile impact. Hence after-impact analysis revealed that cores of AP projectiles were unharmed after passing through hybrid alumina/epoxy composites (see Figure 66), it was necessary to place dense ceramic layer on the front side of hybrid composites, in order to improve ability of hybrid composites to abrade the tip of AP projectile.

Figure 66. *7.62 mm x 54R B32 API projectiles; left: with copper jacket before shooting, right: quenched steel core of the projectile after passing through Al_2O_3 45S/EPOLAM 2017 composite.*

Results of ballistic testing of alumina/slip cast alumina/resins composites revealed that alumina plate slip cast directly on the ice-templated scaffold was able to lower the corrected DOP approximately by 12 mm. Dense alumina layer was able to partially abrade the tip of projectile and distribute the impact energy in higher volume of hybrid composite under the dense plate. Noteworthy fact is that the DOP cor. is comparable for all alumina/slip cast alumina/resin composites (~22 mm) despite the fact that results of energy absorption test (Newton cradle test, see Figure 51) shown that polyurethane resin GM 959/959-1 was able to absorb about 20 % more of input energy in comparison with epoxy resin. This discrepancy can be caused by several reasons, or by combination of all of them.

- Deformation caused by impacting projectile is so fast that all used polymeric resins exhibit rather brittle behavior.
- The weakest points of all hybrid ice-templated alumina/polymer composites are thin alumina lamellae that have similar thickness for all prepared composites.
- The weakest point is adhesion between applied resins and alumina lamellae.
- The amount of infiltrated resin is too high, respectively interlamellar distances are too high to enable synergic behavior of alumina/polymer composite.

As it was shown by Munch et al. [61], it is possible to improve fracture toughness of alumina/ PMMA composites by subsequent pressing of lamellar structure infiltrated with PMMA and creating ”brick and mortar” structure (see Figure 20). This approach possibly could improve ballistic performance of our hybrid alumina/resin composites, but the manufacturing procedure that was presented by Munch et al. was too complex and its use would make our hybrid composites too expensive and price- noncompetitive with other types of ballistic protection materials.

Best ballistic performance among all hybrid composites was performed by A/Ahex/ GM 959 with the corrected DOP of 6.0 mm which is comparable to ballistic performance of dense alumina plate. However, the thickness of slip cast hexagons was 10 mm compared to 7 mm thickness of slip cast dense Al_2O_3 plates. Overall thickness of A/Ahex/ GM 959 composites was 10 mm higher compared to alumina plate. The areal density was as well significantly lower in case of dense Al_2O_3 plates (~26.9 $kg \cdot m^{-2}$ vs. 39.4 $kg \cdot m^{-2}$).

The addition of dense alumina plate/segments on the front side of composites partially helped to abrade tips of AP projectiles, but the hybrid ice-templated alumina/resins plates failed to support these dense layers sufficiently to be able to absorb more kinetic energy of impacting projectile by cracking and crushing of dense ceramics. It would be possible to add thicker layer of dense Al_2O_3 on the front side of hybrid composites to prevent AP projectiles to penetrate through, but this step doesn´t make sense in terms of areal density of the final ballistic protection. Even the A/Ahex/ GM 959 hybrid composite in presented configuration has higher areal density than 7 mm dense alumina plate used for comparison and other materials commonly used for ballistic protection against AP projectiles [102; 103; 104] .

Taking in account all previously mentioned parameters, it can be concluded that ice-templated alumina/polymer hybrid composites in presented configurations are not able to sufficiently replace commonly used materials (dense ceramics, or combination of dense ceramics with polymers and aramid composites) in ballistic protection against 7.62 mm x 54R B32 API projectiles.

7 Conclusions

- Ice-templating apparatus with dimensions suitable for preparation of large samples and ice-templating vessels with designed inner structure and various dimensions were successfully designed, constructed, and put into practice.

- Ceramic suspensions for ice-templating were successfully prepared from different powders (mainly hydroxyapatite and alumina) with different solid loadings of ceramic powder from 7.5 vol.% up to 45 vol.%. Sugar approved to be be the best additive in terms of resulting microstructure of the ice-templated scaffolds (creation of interlamellar bridges) and green body mechanical properties, sufficient for manipulation with samples.

- Combination of ice-templating and indirect rapid prototyping has been shown to enable manufacturing of bioceramic scaffolds for bone replacement from hydroxyapatite with multiscale porosity, including a well-defined interconnected network of macro channels. The compressive strength of resulting scaffolds seems to be somewhat lower than in the case of robocast samples with a similar total porosity even though in order to achieve a similar (slightly lower) porosity a significantly lower (950 °C vs. 1200 °C) sintering temperature had to be used. However, the increased level of interconnected multiscale porosity coupled to a very fine microstructure in the ice-templated samples sintered at 1200 °C (average grain size about 500 nm) could prove to be beneficial for the development of highly porous bioactive scaffolds with enhanced biological performance. Ice-templating also significantly modified the phase composition change during the sintering step, which could be beneficial in biological scaffolds properties tailoring, but further investigation is necessary to clarify this phenomenon.

- Hybrid alumina/polymer composites were successfully designed and prepared from ice-templated alumina plates (solid loading in starting suspensions from 25 vol.% to 45 vol.%; final alumina volume fraction from 44 % to 65 %) and all used polymeric resins. The main limiting factor for infiltration appeared to be combination of higher viscosity and limited pot time of polyurethane resins.

- Mechanical performance of hybrid alumina/epoxy resin composites was tested and the results showed that the optimal strength/density ratio was found for initial content of alumina from 35 to 40 vol.% (density from 2.6 to 2.8 $g \cdot cm^{-3}$). These composites exhibit Weibull strength of 117 MPa and 116 MPa, respectively. Presented mechanical properties are comparable with data reported in the literature when more complicated procedures after ice-templating were applied. Ice-templating reveals to be the robust method for production of hybrid ceramic-polymer composites with good strength/density ratio.

- Ballistic tests of ice-templated alumina/polymer hybrid composites revealed that majority of composites in presented in this work are not able to efficiently stop armor piercing projectiles. The only hybrid composite that was able to stop 7.62 mm x 54R B32 API projectile was A/Ahex/ GM 959 with cor. DOP of 6.0 mm, but even this composite was worse, in terms of thickness and areal density, compared to dense alumina plate. Further thorough tailoring of hybrid composites manufacturing procedures would be necessary to achieve their sufficient ballistic performance against armor piercing projectiles.

8 References

[1] RIEDEL, Ralf. a I-Wei. CHEN. Ceramics science and technology. Weinheim: Wiley-VCH, 2013. ISBN isbn978-3-527-31155-2.

[2] DAVID J. GREEN., . An Introduction to the Mechanical Properties of Ceramics. Cambridge: Cambridge University Press, 1998. ISBN 9780511623103.

[3] DEVILLE, Sylvain, Hasse FREDRIKSSON, Ulla ÅKERLIND, Tassilo MORITZ a Hans RICHTER. Ice-templating, freeze casting: Beyond materials processing. Journal of Materials Research. 2013, 28(17), 391-396. DOI: http://dx.doi.org/10.4028/3-908158-01-x.391.

[4] MAHLER, Walter a Max BECHTOLD. Freeze-formed silica fibres. Nature. 1980, 285(5759), 27-28. DOI: http://dx.doi.org/10.1038/285027a0.

[5] FUKASAWA, Takayuki, Motohide ANDO, Tatsuki OHJI a Shuzo KANZAKI. Synthesis of Porous Ceramics with Complex Pore Structure by Freeze-Dry Processing. Journal of the American Ceramic Society. 2001, 84(1), 230-232. DOI: http://dx.doi.org/10.1111/j.1151-2916.2001.tb00638.x.

[6] DEVILLE, Sylvain, Sylvain MEILLE a Jordi SEUBA. A meta-analysis of the mechanical properties of ice-templated ceramics and metals. Science and Technology of Advanced Materials. 2016, 16(4), 043501. DOI: 10.1088/1468-6996/16/4/043501. ISSN 1468-6996.

[7] KURAPOVA, O.Yu. Cryochemical methods for manufacturing nanosized ceramics and ceramic precursor powders with low agglomeration degree: A review. Reviews on advanced materials science. 2012, 32(2), 112-132.

[8] ZHENG, Jumeng, Louis WINNUBST, VELIANTI et al. Manipulation of Sintering Behavior by Initial Freeze Pressing an Aqueous Alumina Suspension. Advanced Engineering Materials. 2011, 13(1-2), 129-134. DOI: http://dx.doi.org/10.1007/978-1-4899-5301-8_10.

[9] ZHANG, Yumin, Luyang HU, Jiecai HAN a Zehui JIANG. Freeze casting of aqueous alumina slurries with glycerol for porous ceramics. Ceramics International. 2010, 36(2), 617-621. DOI: 10.1016/j.ceramint.2009.09.036. ISSN 02728842.

[10] CHEN, Ruifeng, Chang-An WANG, Yong HUANG, Liguo MA a Weiyuan LIN. Ceramics with Special Porous Structures Fabricated by Freeze-Gelcasting: Using tert-Butyl Alcohol as a Template. Journal of the American Ceramic Society. 2007, 90(11), 3478-3484. DOI: 10.1111/j.1551-2916.2007.01957.x. ISSN 0002-7820.

[11] LI, W, K LU a J WALZ. Freeze casting of porous materials: review of critical factors in microstructure evolution. International Materials Reviews. 2013, 57(1), 37-60. DOI: 10.1179/1743280411Y.0000000011. ISSN 0950-6608.

[12] ARAKI, Kiyoshi a John HALLORAN. New Freeze-Casting Technique for Ceramics with Sublimable Vehicles. Journal of the American Ceramic Society. 2004, 87(10), 1859-1863. DOI: 10.1111/j.1151-2916.2004.tb06331.x. ISSN 00027820.

[13] HONG, C, X ZHANG, J HAN, J DU a W HAN. Ultra-high-porosity zirconia ceramics fabricated by novel room-temperature freeze-casting. Scripta Materialia. 2009, 60(7), 563-566. DOI: 10.1016/j.scriptamat.2008.12.011. ISSN 13596462.

[14] KIM, J.H., J.H. LEE, T.Y. YANG, S.Y. YOON, B.K. KIM a H.C. PARK. TBA-based freeze/gel casting of porous hydroxyapatite scaffolds. Ceramics International. 2011, 37(7), 2317-2322. DOI: 10.1016/j.ceramint.2011.03.023. ISSN 02728842.

[15] SOFIE, Stephen. Fabrication of Functionally Graded and Aligned Porosity in Thin Ceramic Substrates With the Novel Freeze?Tape-Casting Process. Journal of the American Ceramic Society . 2007, 90(7), 2024-2031. DOI: 10.1111/j.1551-2916.2007.01720.x. ISSN 0002-7820.

[16] DEVILLE, S. Freeze-Casting of Porous Ceramics: A Review of Current Achievements and Issues. Advanced Engineering Materials. 2008, 10(3), 155-169. DOI: 10.1002/adem.200700270. ISSN 14381656.

[17] WEGST, U., M. SCHECTER, A. DONIUS a P. HUNGER. Biomaterials by freeze casting. Philosophical Transactions of the Royal Society A: Mathematical, Physical and Engineering Sciences. 2010, 368(1917), 2099-2121. DOI: 10.1098/rsta.2010.0014. ISSN 1364-503X.

[18] PORTER, Michael, Joanna MCKITTRICK a Marc MEYERS. Biomimetic Materials by Freeze Casting. JOM. 2013, 65(6), 720-727. DOI: http://dx.doi.org/10.1007/s11837-013-0606-3.

[19] ZHANG, Haifei, Irshad HUSSAIN, Mathias BRUST, Michael BUTLER, Steven RANNARD a Andrew COOPER. Aligned two- and three-dimensional structures by directional freezing of polymers and nanoparticles. Nature Materials. 2005, 4(10), 787-793. DOI: 10.1038/nmat1487. ISSN 1476-1122.

[20] DEVILLE, S. Freezing as a Path to Build Complex Composites. Science. 2006, 311(5760), 515-518. DOI: 10.1126/science.1120937. ISSN 0036-8075.

[21] DEVILLE, Sylvain, Eric MAIRE, Audrey LASALLE, Agnès BOGNER, Catherine GAUTHIER, Jérôme LELOUP a Christian GUIZARD. In Situ X-Ray Radiography and Tomography Observations of the Solidification of Aqueous Alumina Particle Suspensions-Part I: Initial Instants. Journal of the American Ceramic Society. 2009, 92(11), 2489-2496 . DOI: 10.1111/j.1551-2916.2009.03163.x. ISSN 00027820.

[22] DEVILLE, Sylvain, Eric MAIRE, Audrey LASALLE, Agnès BOGNER, Catherine GAUTHIER, Jérôme LELOUP a Christian GUIZARD. In Situ X-Ray Radiography and Tomography Observations of the Solidification of Aqueous Alumina Particles Suspensions. Part II: Steady State. Journal of the American Ceramic Society. 2009, 92(11), 2497-2503. DOI: 10.1111/j.1551-2916.2009.03264.x. ISSN 00027820.

[23] PEPPIN, Stephen, M. WORSTER a J.S. WETTLAUFER. Morphological instability in freezing colloidal suspensions. Proceedings of the Royal Society A: Mathematical, Physical and Engineering Sciences. 2007, 463(2079), 723-733. DOI: 10.1098/rspa.2006.1790. ISSN 1364-5021.

[24] BAREGGI, Andrea, Eric MAIRE, Audrey LASALLE a Sylvain DEVILLE. Dynamics of the Freezing Front During the Solidification of a Colloidal Alumina Aqueous Suspension: In Situ X-Ray Radiography, Tomography, and Modeling. Journal of the American Ceramic Society. 2011, 94(10), 3570-3578. DOI: 10.1111/j.1551-2916.2011.04572.x. ISSN 00027820.

[25] MUNCH, Etienne, Eduardo SAIZ, Antoni TOMSIA a Sylvain DEVILLE. Architectural Control of Freeze-Cast Ceramics Through Additives and Templating. Journal of the American Ceramic Society. 2009, 92(7), 1534-1539. DOI: 10.1111/j.1551-2916.2009.03087.x. ISSN 00027820.

[26] PEKOR, Christopher a Ian NETTLESHIP. The effect of the molecular weight of polyethylene glycol on the microstructure of freeze-cast alumina. Ceramics International. 2014, 40(7), 9171-9177. DOI: 10.1016/j.ceramint.2014.01.134. ISSN 02728842.

[27] DEVILLE, Sylvain, Céline VIAZZI a Christian GUIZARD. Ice-Structuring Mechanism for Zirconium Acetate. Langmuir. 2012, 28(42), 14892-14898. DOI: 10.1021/la302275d. ISSN 0743-7463.

[28] LASALLE, Audrey, Christian GUIZARD, Eric MAIRE, Jérôme ADRIEN a Sylvain DEVILLE. Particle redistribution and structural defect development during ice templating. Acta Materialia. 2012, 60(11), 4594-4603. DOI: 10.1016/j.actamat.2012.02.023. ISSN 13596454.

[29] STYLE, Robert, Stephen PEPPIN, Alan COCKS a J. WETTLAUFER. Ice-lens formation and geometrical supercooling in soils and other colloidal materials. Physical Review E. 2011, 84(4). DOI: 10.1103/PhysRevE.84.041402. ISSN 1539-3755.

[30] WEGST, Ulrike, Hao BAI, Eduardo SAIZ, Antoni TOMSIA a Robert RITCHIE. Bioinspired structural materials. Nature Materials. 2014, 14(1), 23-36. DOI: 10.1038/nmat4089. ISSN 1476-1122.

[31] DEVILLE, Sylvain, Eduardo SAIZ a Antoni TOMSIA. Ice-templated porous alumina structures. Acta Materialia. 2007, 55(6), 1965-1974. DOI: 10.1016/j.actamat.2006.11.003. ISSN 13596454.

[32] PORTER, Michael, Michael YEH, James STRAWSON, Thomas GOEHRING, Samuel LUJAN, Philip SIRIPASOPSOTORN, Marc MEYERS a Joanna MCKITTRICK. Magnetic freeze casting inspired by nature. Materials Science and Engineering: A. 2012, 556, 741-750. DOI: 10.1016/j.msea.2012.07.058. ISSN 09215093.

[33] WASCHKIES, T., R. OBERACKER a M.J. HOFFMANN. Investigation of structure formation during freeze-casting from very slow to very fast solidification velocities. Acta Materialia. 2011, 59(13), 5135-5145. DOI: 10.1016/j.actamat.2011.04.046. ISSN 13596454.

[34] NAGLIERI, Valentina, Hrishikesh BALE, Bernd GLUDOVATZ, Antoni TOMSIA a Robert RITCHIE. On the development of ice-templated silicon carbide scaffolds for nature-inspired structural materials. Acta Materialia. 2013, 61(18), 6948-6957. DOI: 10.1016/j.actamat.2013.08.006. ISSN 13596454.

[35] ABDELWAHED, W, G DEGOBERT, S STAINMESSE a H FESSI. Freeze-drying of nanoparticles: Formulation, process and storage considerations☆. Advanced Drug Delivery Reviews. 2006, 58(15), 1688-1713. DOI: 10.1016/j.addr.2006.09.017. ISSN 0169409x.

[36] FRANKS, Felix. Freeze-drying of bioproducts: putting principles into practice. European Journal of Pharmaceutics and Biopharmaceutics [online]. 1998, 45(3), 221-229 [cit. 2016-04-17]. DOI: 10.1016/S0939-6411(98)00004-6. ISSN 09396411.

[37] PIKAL, M, S SHAH, M ROY a R PUTMAN. The secondary drying stage of freeze drying: drying kinetics as a function of temperature and chamber pressure☆. International Journal of Pharmaceutics . 1990, 60(3), 203-207. DOI: 10.1016/0378-5173(90)90074-E. ISSN 03785173.

[38] SHAOZHI, Zhang, Peng YU, Liu DONGPO, Zheng YOUMING, Chen GUANGMING a Lu HENG. A thermophysical study on the freeze drying of wooden archaeological artifacts. Journal of Cultural Heritage. 2016, 17, 95-101. DOI: 10.1016/j.culher.2015.07.003. ISSN 12962074.

[39] MARTÍNEZ-VÁZQUEZ, Francisco, Antonia PAJARES a Pedro MIRANDA. Effect of the drying process on the compressive strength and cell proliferation of hydroxyapatite-derived scaffolds. International Journal of Applied Ceramic Technology. 2017, 14(6), 1101-1106. DOI: 10.1111/ijac.12755. ISSN 1546542X.

[40] LOH, Qiu a Cleo CHOONG. Three-Dimensional Scaffolds for Tissue Engineering Applications: Role of Porosity and Pore Size. Tissue Engineering Part B: Reviews. 2013, 19(6), 485-502. DOI: 10.1089/ten.teb.2012.0437. ISSN 1937-3368.

[41] LIU, C.Z., E. SACHLOS, D.A. WAHL, Z.W. HAN a J.T. CZERNUSZKA. On the manufacturability of scaffold mould using a 3D printing technology. Rapid Prototyping Journal. 2007, 13(3), 163-174. DOI: 10.1108/13552540710750915. ISSN 1355-2546.

[42] LIU, C., Z. XIA, Z. HAN, P. HULLEY, J. TRIFFITT a J. CZERNUSZKA. Novel 3D collagen scaffolds fabricated by indirect printing technique for tissue engineering. Journal of Biomedical Materials Research Part B: Applied Biomaterials. 2008, 85(2), 519-528. DOI: 10.1002/jbm.b.30975. ISSN 15524973.

[43] MURPHY, Ciara a Fergal O'BRIEN. Understanding the effect of mean pore size on cell activity in collagen-glycosaminoglycan scaffolds. Cell Adhesion & Migration. 2014, 4(3), 377-381. DOI: 10.4161/cam.4.3.11747. ISSN 1933-6918.

[44] MIRANDA, Pedro, Antonia PAJARES, Eduardo SAIZ, Antoni TOMSIA a Fernando GUIBERTEAU. Mechanical properties of calcium phosphate scaffolds fabricated by robocasting. Journal of Biomedical Materials Research Part A. 2008, 85(1), 218-227 . DOI: 10.1002/jbm.a.31587. ISSN 15493296.

[45] HOUBEN, Annemie, Jasper VAN HOORICK, Jürgen VAN ERPS, Hugo THIENPONT, Sandra VAN VLIERBERGHE a Peter DUBRUEL. Indirect Rapid Prototyping: Opening Up Unprecedented Opportunities in Scaffold Design and Applications. Annals of Biomedical Engineering. 2017, 45(1), 58-83. DOI: 10.1007/s10439-016-1610-x. ISSN 0090-6964.

[46] BILLIET, Thomas, Mieke VANDENHAUTE, Jorg SCHELFHOUT, Sandra VAN VLIERBERGHE a Peter DUBRUEL. A review of trends and limitations in hydrogel-rapid prototyping for tissue engineering. Biomaterials . 2012, 33(26), 6020-6041. DOI: 10.1016/j.biomaterials.2012.04.050. ISSN 01429612.

[47] CHIA, Helena a Benjamin WU. Recent advances in 3D printing of biomaterials. Journal of Biological Engineering. 2015, 9(1). DOI: 10.1186/s13036-015-0001-4. ISSN 1754-1611.

[48] CHU, T.M., J.W. HALLORAN, S.J. HOLLISTER a S.E. FEINBERG. Hydroxyapatite implants with designed internal architecture. Journal of materials science. Materials in medicine. 2001, 12(6), 471-8.

[49] LEE, Ju-Yeon, Bogyu CHOI, Benjamin WU a Min LEE. Customized biomimetic scaffolds created by indirect three-dimensional printing for tissue engineering. Biofabrication. 2013, 5(4). DOI: 10.1088/1758-5082/5/4/045003. ISSN 1758-5082.

[50] DEISINGER, Ulrike, Sabine HAMISCH, Matthias SCHUMACHER, Franzika UHL, Rainer DETSCH a Günter ZIEGLER. Fabrication of Tailored Hydroxyapatite Scaffolds: Comparison between a Direct and an Indirect Rapid Prototyping Technique. Key Engineering Materials. 2007, 361-363, 915-918. DOI: 10.4028/www.scientific.net/KEM.361-363.915. ISSN 1662-9795.

[51] KANG, Hyun-Wook a Dong-Woo CHO. Development of an Indirect Stereolithography Technology for Scaffold Fabrication with a Wide Range of Biomaterial Selectivity. Tissue Engineering Part C: Methods. 2012, 18(9), 719-729. DOI: 10.1089/ten.tec.2011.0621. ISSN 1937-3384.

[52] CHEN, Zhongzhong, Dichen LI, Bingheng LU, Yiping TANG, Minglin SUN a Zhen WANG. Fabrication of artificial bioactive bone using rapid prototyping. Rapid Prototyping Journal. 2004, 10(5), 327-333. DOI: 10.1108/13552540410562368. ISSN 1355-2546.

[53] CHU, T.-M.Gabriel, David ORTON, Scott HOLLISTER, Stephen FEINBERG a John HALLORAN. Mechanical and in vivo performance of hydroxyapatite implants with controlled architectures. Biomaterials. 2002, 23(5), 1283-1293. DOI: 10.1016/S0142-9612(01)00243-5. ISSN 01429612.

[54] TABOAS, J.M, R.D MADDOX, P.H KREBSBACH a S.J HOLLISTER. Indirect solid free form fabrication of local and global porous, biomimetic and composite 3D polymer-ceramic scaffolds. Biomaterials. 2003, 24(1), 181-194. DOI: 10.1016/S0142-9612(02)00276-4. ISSN 01429612.

[55] BANSAL, Narottam a Jacques LAMON. Ceramic matrix composites: materials, modeling and technology. Hoboken, New Jersey: Wiley, 2015. ISBN 978-1-118-23116-6.

[56] KERANS, Ronald, Randall HAY, Triplicane PARTHASARATHY a Michael CINIBULK. Interface Design for Oxidation-Resistant Ceramic Composites. Journal of the American Ceramic Society. 2002, 85(11), 2599-2632 . DOI: 10.1111/j.1151-2916.2002.tb00505.x. ISSN 00027820.

[57] BEN RAMDANE, C., A. JULIAN-JANKOWIAK, R. VALLE, Y. RENOLLET, M. PARLIER, E. MARTIN a P. DISS. Microstructure and mechanical behaviour of a Nextel™610/alumina weak matrix composite subjected to tensile and compressive loadings. Journal of the European Ceramic Society. 2017, 37(8), 2919-2932. DOI: 10.1016/j.jeurceramsoc.2017.02.042. ISSN 09552219.

[58] KELLER, Kristin, Tai-Il MAH, Triplicane PARTHASARATHY, Emmanuel BOAKYE, Pavel MOGILEVSKY a Michael CINIBULK. Effectiveness of Monazite Coatings in Oxide/Oxide Composites after Long-Term Exposure at High Temperature. Journal of the American Ceramic Society. 2003, 86(2), 325-332. DOI: 10.1111/j.1151-2916.2003.tb00018.x. ISSN 00027820.

[59] MAH, Tai-Il, Kristin KELLER, Ronald KERANS a Michael CINIBULK. Reduced Cracking in Oxide Fiber-Reinforced Oxide Composites via Freeze-Dry Processing. Journal of the American Ceramic Society. 2015, 98(5), 1437-1443. DOI: 10.1111/jace.13500. ISSN 00027820.

[60] WAMSER, Thomas, Sven SCHELER, Bernd MARTIN a Walter KRENKEL. Novel oxide fiber composites by freeze casting. Journal of the European Ceramic Society. 2014, 34(15), 3827-3833. DOI: 10.1016/j.jeurceramsoc.2014.06.015. ISSN 09552219.

[61] MUNCH, E., M. LAUNEY, D. ALSEM, E. SAIZ, A. TOMSIA a R. RITCHIE. Tough, Bio-Inspired Hybrid Materials. Science. 2008, 322(5907), 371-386. DOI: http://dx.doi.org/10.1002/9781118843499.index.

[62] LAUNEY, M., E. MUNCH, D. ALSEM, E. SAIZ, A. TOMSIA a R. RITCHIE. A novel biomimetic approach to the design of high-performance ceramic-metal composites. Journal of The Royal Society Interface. 2010, 7(46), 741-753. DOI: 10.1098/rsif.2009.0331. ISSN 1742-5689.

[63] LIU, Qiang, Feng YE, Ye GAO, Shichao LIU, Haixia YANG a Zhiqiang ZHOU. Fabrication of a new SiC/2024Al co-continuous composite with lamellar microstructure and high mechanical properties. Journal of Alloys and Compounds. 2014, 585, 146-153. DOI: 10.1016/j.jallcom.2013.09.140. ISSN 09258388.

[64] GHANEM, Amyl a Yujie LANG. Introduction to polymer adhesion. In: . Department of process engineering and applied science, Dalhousie University, 1360 Barrington Street, Halifax, Nova Scotia, Canada, 2017, s. 1-17.

[65] Material Surface Preparation Techniques. Adhesives Technology Handbook. Elsevier, 2009, s. 37-46. DOI: 10.1016/B978-0-8155-1533-3.50006-2. ISBN 9780815515333.

[66] LAUSUND, K.B., B.B. JOHNSEN, D.B. RAHBEK a F.K. HANSEN. Surface treatment of alumina ceramic for improved adhesion to a glass fibre-reinforced polyester composite. International Journal of Adhesion and Adhesives. 2015, 63, 34-45. DOI: 10.1016/j.ijadhadh.2015.07.015. ISSN 01437496.

[67] EBNESAJJAD, Sina a Cyrus EBNESAJJAD. Surface treatment of materials for adhesive bonding. Second edition. Amsterdam: William Andrew, an imprint of Elsevier, 2014. ISBN 978-0-323-26435-8.

[68] THURMOND, John, Wayne BARKMEIER a Terry WILWERDING. Effect of porcelain surface treatments on bond strengths of composite resin bonded to porcelain. The Journal of Prosthetic Dentistry. 1994, 72(4), 355-359. DOI: 10.1016/0022-3913(94)90553-3. ISSN 00223913.

[69] KATO, H., H. MATSUMURA a M. ATSUTA. Effect of etching and sandblasting on bond strength to sintered porcelain of unfilled resin. Journal of Oral Rehabilitation. 2000, 27(2), 103-110. DOI: 10.1046/j.1365-2842.2000.00489.x. ISSN 0305-182X.

[70] KAMEYAMA, Atsushi, Akiko HARUYAMA, Akihiro TANAKA, Akio NORO, Toshiyuki TAKAHASHI, Masao YOSHINARI, Masahiro FURUSAWA a Shuichiro YAMASHITA. Repair Bond Strength of a Resin Composite to Plasma-Treated or UV-Irradiated CAD/CAM Ceramic Surface. Coatings. 2018, 8(7). DOI: 10.3390/coatings8070230. ISSN 2079-6412.

[71] VALVERDE, Guilherme, Paulo COELHO, Malvin JANAL, Fábio LORENZONI, Ricardo CARVALHO, Van THOMPSON, Klaus-Dieter WELTEMANN a Nelson SILVA. Surface characterisation and bonding of Y-TZP following non-thermal plasma treatment. Journal of Dentistry. 2013, 41(1), 51-59. DOI: 10.1016/j.jdent.2012.10.002. ISSN 03005712.

[72] VILAS BOAS FERNANDES JÚNIOR, Virgílio, Débora BARBOSA DANTAS, Eduardo BRESCIANI a Maria ROCHA LIMA HUHTALA. Evaluation of the bond strength and characteristics of zirconia after different surface treatments. The Journal of Prosthetic Dentistry. 2018, 120(6), 955-959. DOI: 10.1016/j.prosdent.2018.01.029. ISSN 00223913.

[73] MATINLINNA, Jukka, Christie LUNG a James TSOI. Silane adhesion mechanism in dental applications and surface treatments: A review. Dental Materials. 2018, 34(1), 13-28. DOI: 10.1016/j.dental.2017.09.002. ISSN 01095641.

[74] LUNG, Christie a Jukka MATINLINNA. Aspects of silane coupling agents and surface conditioning in dentistry: An overview. Dental Materials. 2012, 28(5), 467-477. DOI: 10.1016/j.dental.2012.02.009. ISSN 01095641.

[75] MACA, K., V. POUCHLY a A.R. BOCCACCINI. Sintering densification curve: A practical approach for its construction from dilatometric shrinkage data. Science of Sintering. 2008, 40(2), 117-122. DOI: 10.2298/SOS0802117M. ISSN 0350-820X.

[76] EN 843-2. Advanced technical ceramics - Mechanical properties of monolithic ceramics at room temperature - Part 2: Determination of Young's modulus, shear modulus and Poisson's ratio. 2006.

[77] EN 843-1. Advanced technical ceramics. Mechanical properties of monolithic ceramics at room temperature. Determination of flexural strength. 2007.

[78] EN 843-5. Advanced technical ceramics. Mechanical properties of monolithic ceramics at room temperature. Statistical analysis. 2007.

[79] BLUHM, J.I. Slice synthesis of a three dimensional “work of fracture” specimen. Engineering Fracture Mechanics. 1975, 7(3), 593-604. DOI: 10.1016/0013-7944(75)90059-4. ISSN 00137944.

[80] DLOUHY, I., M. HOLZMAN, J. MAN a L. VALKA. The use of chevron-notched specimens for fracture-toughness determination of bearing steels. Kovové materiály - Metallic Materials.

1994, 32(1), 3-13.

[81] EN 14425-3. Advanced technical ceramics - Test methods for determination of fracture toughness of monolithic ceramics - Part 3: Chevron notched beam (CNB) method. 2010.

[82] DRDLOVÁ, M, M POPOVIČ a M ŠEBÍK. The behavior of cement-bonded wood-chip material under static and impact load. IOP Conference Series: Materials Science and Engineering . 2018, 379, 012025. DOI: 10.1088/1757-899X/379/1/012025. ISSN 1757-8981.

[83] SAVIO, S a V MADHU. Ballistic performance evaluation of ceramic tiles with respect to projectile velocity against hard steel projectile using DOP test. International Journal of Impact Engineering. 2018, 113, 161-167. DOI: 10.1016/j.ijimpeng.2017.11.020. ISSN 0734743X.

[84] SAVIO, S.G., K. RAMANJANEYULU, V. MADHU a T. BHAT. An experimental study on ballistic performance of boron carbide tiles. International Journal of Impact Engineering. 2011, 38(7), 535-541. DOI: 10.1016/j.ijimpeng.2011.01.006. ISSN 0734743X.

[85] CARTON, Erik a Geert ROEBROEKS. Testing Method for Ceramic Armor and Bare Ceramic Tiles. LASALVIA, Jerry C, ed., Jerry LASALVIA. Advances in Ceramic Armor X. Hoboken, NJ, USA: John Wiley & Sons, 2014, s. 1-12. Ceramic Engineering and Science Proceedings. DOI: 10.1002/9781119040590.ch1. ISBN 9781119040590.

[86] GONDA, T., S. NAKAHARA a T. SEI. The formation of side branches of dendritic ice crystals growing from vapor and solution. Journal of Crystal Growth. 1990, 99(1-4), 183-187. DOI: 10.1016/0022-0248(90)90509-J. ISSN 00220248.

[87] SCOTTI, Kristen a David DUNAND. Freeze casting – A review of processing, microstructure and properties via the open data repository, FreezeCasting.net. Progress in Materials Science. 2018, 94, 243-305. DOI: 10.1016/j.pmatsci.2018.01.001. ISSN 00796425.

[88] HAN, Jiecai, Luyang HU, Yumin ZHANG a Yufeng ZHOU. Fabrication of Ceramics with Complex Porous Structures by the Impregnate-Freeze-Casting Process. Journal of the American Ceramic Society. 2009, 92(9), 2165-2167. DOI: 10.1111/j.1551-2916.2009.03168.x. ISSN 00027820.

[89] REED, Stephanie, Grace LAU, Benjamin DELATTRE, David LOPEZ, Antoni TOMSIA a Benjamin WU. Macro- and micro-designed chitosan-alginate scaffold architecture by three-dimensional printing and directional freezing. Biofabrication. 2016, 8(1). DOI: 10.1088/1758-5090/8/1/015003. ISSN 1758-5090.

[90] O'BRIEN, Fergal, Brendan HARLEY, Mary A. WALLER, Ioannis YANNAS, Lorna J. GIBSON a Patrick J. PRENDERGAST. The effect of pore size on permeability and cell attachment in collagen scaffolds for tissue engineering. Technology and health care : official journal of the European Society for Engineering and Medicine. 2007, (15), 3-17.

[91] MURPHY, Ciara, Matthew HAUGH a Fergal O'BRIEN. The effect of mean pore size on cell attachment, proliferation and migration in collagen–glycosaminoglycan scaffolds for bone tissue engineering. Biomaterials. 2010, 31(3), 461-466. DOI: 10.1016/j.biomaterials.2009.09.063. ISSN 01429612.

[92] ZHAO, Cancan, Lunguo XIA, Dong ZHAI, Na ZHANG, Jiaqiang LIU, Bing FANG, Jiang CHANG a Kaili LIN. Designing ordered micropatterned hydroxyapatite bioceramics to promote the growth and osteogenic differentiation of bone marrow stromal cells. Journal of Materials Chemistry B. 2015, 3(6), 968-976. DOI: 10.1039/C4TB01838A. ISSN 2050-750X.

[93] LI, Jingan, Kun ZHANG, Ping YANG, Wei QIN, Guicai LI, Ansha ZHAO a Nan HUANG. Human vascular endothelial cell morphology and functional cytokine secretion influenced by different size of HA micro-pattern on titanium substrate. Colloids and Surfaces B: Biointerfaces. 2013, 110, 199-207. DOI: 10.1016/j.colsurfb.2013.04.048. ISSN 09277765.

[94] MIYAZAKI, Hidetoshi, Isao USHIRODA, Daisuke ITOMURA, Tsunehisa HIRASHITA, Nobuyasu ADACHI a Toshitaka OTA. Thermal expansion of hydroxyapatite between −100 °C and 50 °C. Materials Science and Engineering: C. 2009, 29(4), 1463-1466. DOI: 10.1016/j.msec.2008.12.001. ISSN 09284931.

[95] TõNSUAADU, Kaia, Kārlis GROSS, Liene PLūDUMA a Mihkel VEIDERMA. A review on the thermal stability of calcium apatites. Journal of Thermal Analysis and Calorimetry. 2012, 110(2), 647-659. DOI: 10.1007/s10973-011-1877-y. ISSN 1388-6150.

[96] NAKAMURA, Satoshi, Ryohei OTSUKA, Hideki AOKI, Masaru AKAO, Naoki MIURA a Takeyuki YAMAMOTO. Thermal expansion of hydroxyapatite-β-tricalcium phosphate ceramics. Thermochimica Acta. 1990, 165(1), 57-72 . DOI: 10.1016/0040-6031(90)80206-E. ISSN 00406031.

[97] BOTEAN, Adrian, C. BALAN a M.C. BALAN. Thermal expansion coefficient determination of polylactic acid using digital image correlation. E3S Web of Conferences. 2018, 32. DOI: 10.1051/e3sconf/20183201007. ISSN 2267-1242.

[98] DLOUHY, Ivo, Michal KOTOUL, Tomas VYSLOUZIL, Zdenek CHLUP a Aldo BOCCACCINI. Crack resistance curve in glass matrix composite reinforced by long Nicalon® fibres. Journal of Materials Science. 2008, 43(12), 4022-4030. DOI: 10.1007/s10853-007-2317-z. ISSN 0022-2461.

[99] ČERNÝ, Martin, Zdeněk CHLUP, Zbyněk SUCHARDA a Petr GLOGAR. Fracture Properties of Basalt Fibre Composites with Cured or Pyrolysed Matrix. Key Engineering Materials. 2009, 409, 326-329. DOI: 10.4028/www.scientific.net/KEM.409.326. ISSN 1662-9795.

[100] DLOUHY, I., Z. CHLUP, D.N. BOCCACCINI, S. ATIQ a A.R. BOCCACCINI. Fracture behaviour of hybrid glass matrix composites: thermal ageing effects. Composites Part A: Applied Science and Manufacturing. 2003, 34(12), 1177-1185. DOI: 10.1016/j.compositesa.2003.08.004. ISSN 1359835X.

[101] BOUVILLE, Florian, Eric MAIRE, Sylvain MEILLE, Bertrand VAN DE MOORTèLE, Adam STEVENSON a Sylvain DEVILLE. Strong, tough and stiff bioinspired ceramics from brittle constituents. Nature Materials. 2014, 13(5), 508-514. DOI: 10.1038/nmat3915. ISSN 1476-1122.

[102] CLAYTON, J.D. Penetration resistance of armor ceramics: Dimensional analysis and property correlations. International Journal of Impact Engineering. 2015, 85, 124-131. DOI: 10.1016/j.ijimpeng.2015.06.025. ISSN 0734743X.

[103] BAYER, Petr, Josef KRÁTKÝ, Daniel DRDLÍK a Miloslav POPOVIČ. Ballistic Performance of Al2O3 and SSiC Ceramic with Areal Density of 26 kg/m2 against 7.62 mm Calibre Projectiles. Advanced Materials Research. 2015, 1124, 103-110. DOI: 10.4028/www.scientific.net/AMR.1124.103. ISSN 1662-8985.

[104] JIUSTI, J., E.H. KAMMER, L. NECKEL, N.J. LÓH, W. TRINDADE, A.O. SILVA, O.R.K. MONTEDO a A. DE NONI. Ballistic performance of Al2O3 mosaic armors with gap-filling materials. Ceramics International. 2017, 43(2), 2697-2704. DOI: 10.1016/j.ceramint.2016.11.087. ISSN 02728842.

9 Author´s publications and other outputs

Publications

- FORAL, Š., K. KATOVSKÝ, J. VARMUŽA, D. SALAMON and J. ROLEČEK. Influence of silicone carbide on the reactivity of nuclear fuels using cerium dioxide as a surrogate material. In *Proceedings on 2014 22nd International Conference on Nuclear Engineering (ICONE22).* 2014. s. 1-10. ISBN: 978-0-7918-4594- 3

- ROLEČEK, J., Š. FORAL, K. KATOVSKÝ and D. SALAMON. A feasibility study of using CeO_2 as a surrogate material during the investigation of UO_2, *Advances in Applied Ceramics, 2017*, *116(3), 123-131. DOI: 10.1080/17436753.2016.1264122.*

- ROLEČEK, J., D. SALAMON and Z. CHLUP. Mechanical properties of hybrid composites prepared by ice-templating of alumina, *Journal of the European Ceramic Society*. 2017, 37(14), 4279-4286. DOI: 10.1016/j.jeurceramsoc.2017.04.007.

- DRDLÍK, D., J. ROLEČEK, K.DRDLÍKOVÁ and D. SALAMON. Restraining of calcium contamination in near-net shape alumina ceramics during slip casting. *International Journal of Applied Ceramic Technology*. DOI: 10.1111/ijac.13042.

- DRDLÍK, D., V. MAŘÁK, J. ROLEČEK, K. DRDLÍKOVÁ, J. KRATOCHVÍL and D. SALAMON. Study of Alumina and Alumina-Silicon Carbide Layered Composites Sintered by SPS. *Key Engineering Materials (print)*, 2018, vol. 784, no. 1, p. 67-72. ISSN: 1013-9826.

- ROLEČEK, J., L. PEJCHALOVÁ, F.J. MARTÍNEZ-VÁZQUEZ, P. MIRANDA GONZÁLEZ a D. SALAMON. Bioceramic scaffolds fabrication: Indirect 3D printing combined with ice-templating vs. robocasting. *Journal of the European Ceramic Society*. 2019, 39(4), 1595-1602. DOI: 10.1016/j.jeurceramsoc.2018.12.006.

Patents and functional samples

- SALAMON, D.; GOCKERT, R.; ROLEČEK, J.; Vysoké učení technické v Brně: Metoda výroby samostatně stojících ultratenkých dutých keramických vláken využívající obětovaných šablon. 307596, Patent. (2018)

- DRDLÍK, D.; ROLEČEK, J.; SALAMON, D.: Balistická keramika typ HV2017-1; Efektivně tvarovaná keramika pro balistické účely. Vysoké učení technické v Brně, Středoevropský technologický institut, Purkyňova 123, 612 00, Brno. (Functional sample)

- SALAMON, D.; ROLEČEK, J.; DRDLÍK, D.; KACHLÍK, M.; SPUSTA, T.: HR; Hybridní kompozit keramika-polymer pro balistickou ochranu. Vysoké učení technické v Brně, Středoevropský technologický institut, Purkyňova 123, 612 00, Brno. (Functional sample)

- DRDLÍK, D.; ROLEČEK, J.; SALAMON, D.: Balistická keramika typ HV2017-4; Efektivně tvarovaná keramika pro balistické účely. Vysoké učení technické v Brně, Středoevropský technologický institut, Purkyňova 123, 612 00, Brno. (Functional sample)

Projects

Technology Agency of the Czech Republic – "Centre of advanced materials and technologies for protection and safety enhancement"

- Design, manufacturing and upgrading of the Ice-templating apparatus and using of the freeze casting technology for preparation of hybrid armor.
- Design and manufacturing of dies for slip casting; development and tailoring of slip casting technique for preparation of dense ceramic armor.
- Development of the ceramic-metal composites for ballistic protection.
- Preparation of samples from ceramics and various polymers for data gathering from static a dynamic mechanical testing for finite element simulations.
- Responsible for preparation of samples for ballistic testing.
- Responsible for deliverables 2016, 2017, 2018 and 2019.

Other outputs

ANM 2015, odborný seminář doktorandů
11.2. – 12.2.2015; Praha

- National student speech contest – active participation with oral presentation on theme: *"Ice-templating of ceramics in industrial scale"*.

Conference Frontiers in Material and Life Sciences: Creating life in 3D
2.9 – 4.9.2015; Brno

- Active participation with poster on theme: *"Shaping of bioceramics on micro level via dip-coating process"*.

11th Conference for Young Scientists in Ceramics
21.9. – 24.9.2015; Novi Sad, Serbia

- Active participation with oral presentation on theme: *"Ice-templating of ceramics in industrial scale"*.

Conference Fractography of Advanced Ceramics V
9.10. – 12.10.2016; Smolenice, Slovakia

- Active participation with oral presentation on theme: *"Mechanical properties of hybrid ceramic composites prepared by ice-templating"*.

ANM 2017, odborný seminář doktorandů
8.2. – 9.2.2017; Praha

- National Student Speech Contest – active participation with oral presentation on theme: *"Mechanical properties of hybrid ceramic composites prepared by ice-templating"*.
- ***1st place in the National student speech contest.***

15th Conference and Exhibition of the European Ceramic Society
9.7. – 13.7.2017; Budapest, Hungary

- Active participation in the ECerS Student Speech Contest as a representative of the Czech Republic with oral presentation on theme: *"Mechanical properties of hybrid ceramic composites prepared by ice-templating"*.

Additive manufacturing as a tool to create life in 3D
26.7. – 27.7.2017; Brno

- Active participation in poster session of the workshop with poster on theme: *"Shaping of bioceramics scaffolds on micro/macro level by 3D printing and freeze-casting"*.

Research internship

- **13.10.2017 – 08.12.2017**
  Escuela de Ingenierías Industriales, Universidad de Extremadura, Avda. de Elvas 06006 Badajoz, Spain
  Project: ***„Porous ceramic and composite scaffolds prepared by direct and indirect rapid prototyping"***

- **05.04.2018 – 24.04.2018**
  Escuela de Ingenierías Industriales, Universidad de Extremadura, Avda. de Elvas 06006 Badajoz, Spain
  Project: ***„Comparative study of mechanical properties of designed macro channels in bioceramic scaffolds by robocasting and indirect 3D printing combined with ice-templating"***